Multiscale numerical modelling of mechanical behavior in pile-soil system

Jianhong Wan

▶ To cite this version:

Jianhong Wan. Multiscale numerical modelling of mechanical behavior in pile-soil system. Civil Engineering. Université de Lille; Sun Yat-sen University, 2023. English. NNT : 2023ULILN033 . tel-04794667

HAL Id: tel-04794667
https://theses.hal.science/tel-04794667v1

Submitted on 21 Nov 2024

N° d'ordre :

THÈSE DE DOCTORAT EN COTUTELLE DE L'UNIVERSITÉ DE LILLE ET DE L'UNIVERSITÉ SUN YAT-SEN

réalisée au sein de

École doctorale n°632 : Sciences de l'Ingénierie et des Systèmes – ENGYS

Laboratoire de Génie Civil et Géo-Environnement – LGCgE ULR4515

Modélisation numérique multi-échelle du comportement mécanique d'un système pieux-sol

Multiscale numerical modelling of mechanical behavior in pile-soil system

---

Thèse soutenue publiquement le 07/11/2023, par

Jianhong WAN

pour obtenir le grade de

DOCTEUR en Mécanique, génie mécanique, génie civil de l'Université de Lille

Devant le jury composé de :

Siham KAMALI-BERNARD	Institut National des Sciences Appliquées de Rennes	Professeur	Président
Andrey G. KALINICHEV	Institut Mines-Télécom Atlantique	Directeur de Recherche	Rapporteur
Wei YANG	University of Hunan (China)	Professeur	Rapporteur
Yuanyuan ZHENG	Sun Yat-Sen University (China)	Professeur	Examinateur
Ali ZAOUI	Université de Lille	Professeur	Direction de thèse
Xueyou LI	Sun Yat-Sen University (China)	Professeur	Direction de thèse

Abstract

The study of pile-soil systems is of paramount importance in the field of geotechnical engineering, as it is directly related to the stability and reliability of structures and infrastructure. This work investigates the mechanical behavior in pile-soil systems, with a focus on fiber-reinforced polymer (FRP) piles and rubber-soil mixes (RSM).

Three main aspects are investigated using molecular dynamics (MD) simulations. First, the evolution of interfacial friction between the FRP pile and clay plays a critical role in determining the pile shaft resistance. Friction properties at the FRP pile-clay interface are studied using a kaolinite-epoxy model, which yields a calculated work of adhesion value of 159 mJ/m^2. The peak interfacial shear coefficients decrease nonlinearly with increasing normal stress. The interfacial friction process is characterized by its velocity-dependent with distinct velocity ranges, and these characteristics are captured by the extended Bell theory. It is observed that stick-slip motion manifests itself exclusively in scenarios with lower sliding velocities. This observed trend of increasing energy barriers with increasing normal stresses highlights the increased pulling forces required to induce FRP sliding along the clay interface under higher normal stress conditions.

Second, it is necessary to determine friction behavior of FRP pile in the marine environment due to the characteristics of the pile-soil interaction. MD simulations are used to investigate the interfacial friction at the FRP pile-sand interface under various dry, pure water, and salt water conditions. A cross-linked epoxy resin is synthesized to study its interactions with crystalline silica. Friction force-displacement relationships show distinct nonlinear and steady-state phases. Tangential stiffness profiles, especially at lower normal stress levels, show faster reductions to reach the steady-state. Water molecules act as lubricants, with NaCl ions affecting their effectiveness. Dry systems have the highest coefficient of friction, followed by salt water and pure water systems.

Third, the influence of clay minerals on soil frictional strength and system stability in the context of earthquake mechanics is essential for the RSM system. The interaction at the rubber/soil interface is studied within RSM using MD simulations. Friction force increases with sliding distance and normal stress, which is consistent with the friction behavior between natural soils. Compaction of rubber and clay increases friction forces and improves engineering properties. Rubber particles reduce stick-slip motion at the montmorillonite-rubber interface, providing a damping effect that reduces stick-slip vibration during sliding. Interfacial parameters and friction coefficients are determined and agree with experimental data, improving the understanding of RSM behavior and applications in soil foundations.

Another important aspect is investigated based on the finite element (FE) method. Predicting pile behavior under extreme loads is an essential design consideration. In this study, an efficient integrated pile-soil element is introduced to simulate the pile behavior while taking into account the nonlinearity of the soil and pile material. The plastic hinges and soil springs are integrated into the proposed element formulations, so that one element type is sufficient to conveniently simulate the nonlinear pile-soil interactions. A Python program has been developed based on the FE method, and the detailed analysis procedure is given. Validation with field tests demonstrates its accuracy for analyzing the pile behavior under lateral and axial loads.

Keywords: FRP pile; sand; clay; interface friction; rubber-soil mixtures; molecular dynamics; finite element method.

Résumé

L'étude des systèmes pieux-sol est d'une importance capitale dans le domaine de l'ingénierie géotechnique, car elle est directement liée à la stabilité et à la fiabilité des structures et des infrastructures. Ce travail étudie le comportement mécanique des systèmes pieux-sol, en se concentrant sur les pieux en polymère renforcé de fibres (FRP) et les mélanges caoutchouc-sol (RSM).

Trois aspects principaux sont étudiés à l'aide de simulations de dynamique moléculaire (MD). Tout d'abord, l'évolution du frottement interfacial entre le pieu FRP et l'argile joue un rôle essentiel dans la détermination de la résistance de l'arbre du pieu. Les propriétés de frottement à l'interface entre le pieu FRP et l'argile sont étudiées à l'aide d'un modèle kaolinite-époxy, qui donne une valeur calculée du travail d'adhésion de 159 mJ/m2. Les coefficients de cisaillement interfaciaux maximaux diminuent de manière non linéaire avec l'augmentation de la contrainte normale. Le processus de frottement interfacial est caractérisé par le fait qu'il dépend de la vitesse avec des plages de vitesse distinctes, et ces caractéristiques sont prises en compte par la théorie de Bell étendue. On observe que le mouvement de stick-slip se manifeste exclusivement dans les scénarios où les vitesses de glissement sont faibles. Cette tendance à l'augmentation des barrières énergétiques avec l'augmentation des contraintes normales met en évidence l'augmentation des forces de traction nécessaires pour induire le glissement du FRP le long de l'interface avec l'argile dans des conditions de contraintes normales plus élevées.

Deuxièmement, il est nécessaire de déterminer le comportement du frottement des pieux en FRP dans l'environnement marin en raison des caractéristiques de l'interaction entre les pieux et le sol. Des simulations MD sont utilisées pour étudier le frottement interfacial à l'interface pile FRP-sable dans diverses conditions de sécheresse, d'eau pure et d'eau salée. Une résine époxy réticulée est synthétisée pour étudier ses interactions avec la silice cristalline. Les relations force-déplacement de frottement présentent des phases non linéaires et stables distinctes. Les profils de rigidité tangentielle, en particulier à des niveaux de contrainte normale plus faibles, montrent des réductions plus rapides pour atteindre l'état d'équilibre. Les molécules d'eau agissent comme des lubrifiants, les ions NaCl affectant leur efficacité. Les systèmes secs ont le coefficient de frottement le plus élevé, suivis par les systèmes à l'eau salée et à l'eau pure.

Troisièmement, l'influence des minéraux argileux sur la résistance au frottement du sol et la stabilité du système dans le contexte de la mécanique des tremblements de terre est essentielle pour le système RSM. L'interaction à l'interface caoutchouc/sol est étudiée dans le cadre de RSM à l'aide de simulations MD. La force de frottement augmente avec la distance de glissement et la contrainte normale, ce qui est cohérent avec le comportement de frottement entre les sols naturels. Le compactage du caoutchouc et de l'argile augmente les forces de frottement et améliore les propriétés techniques. Les particules de caoutchouc réduisent le mouvement de stick-slip à l'interface montmorillonite-caoutchouc, fournissant un effet d'amortissement qui réduit la vibration de stick-slip pendant le glissement. Les paramètres interfaciaux et les coefficients de frottement sont déterminés et concordent avec les données expérimentales, ce qui améliore la compréhension du comportement du RSM et les applications dans les fondations des sols.

Un autre aspect important est étudié sur la base de la méthode des éléments finis (FE). La prévision du comportement des pieux sous des charges extrêmes est une considération essentielle de la conception. Dans cette étude, un élément pieu-sol intégré efficace est introduit pour simuler le comportement du pieu tout en tenant compte de la non-linéarité du sol et du matériau du pieu. Les charnières plastiques et les ressorts du sol sont intégrés dans les formulations de l'élément proposé, de sorte qu'un seul type d'élément suffit pour simuler commodément les interactions non linéaires entre le pieu et le sol. Un programme Python a été développé sur la base de la méthode FE, et la procédure d'analyse détaillée est donnée. La validation par des essais sur le terrain démontre sa précision pour l'analyse du comportement des pieux sous des charges latérales et axiales.

Mots clés: Pile FRP; sable; argile; frottement d'interface; mélanges caoutchouc-sol; dynamique moléculaire; méthode des éléments finis.

Acknowledgements

First of all, I would like to express my deep appreciation to my supervisor, Prof. Ali ZAOUI. His supervision has not only helped me grow as a researcher, but has also taught me the importance of hard work and perseverance. I have learned so much from Prof. ZAOUI, and I feel so fortunate to have the opportunity to work with someone who has such an impressive expertise and knowledge. He has always created an open and friendly environment where I felt comfortable sharing my thoughts, asking for advice, and working with other colleagues. With his guidance and help, I was able to complete this thesis.

I would also like to express my sincere gratitude to my co-supervisor Prof. Xueyou LI for his great help in academics. From the very beginning, Prof. LI has been an inspiring role model. His expertise and guidance have pushed me to explore new areas and challenge myself. His insightful feedback and constructive advice have been essential in improving my research ideas and methods, leading to more rigorous research results.

I am very grateful to Dr. Wassila SEKKAL for the guidance and advice she gave me in every group meeting. She has helped me a lot in learning about molecular dynamics.

I would like to express my sincere gratitude to the members of my PhD committee, Prof. Siham KAMALI-BERNARD, Prof. Andrey G. KALINICHEV, Prof. Wei YANG, and Prof. Yuanyuan ZHENG.

I am very grateful to my group members, colleagues, and friends. Their support, discussions, and sharing have made this journey not only academically rewarding, but also personally fulfilling.

I would like to express my love and gratitude to my families: my wife Lilan ZHANG and my parents. Their encouragement and endless love have been my driving force throughout this academic pursuit.

Finally, I wish to express my sincere gratitude to the people who have played an important role in my journey to complete this thesis. Their support, encouragement, and guidance have been invaluable.

Contents

General introduction

Pile foundations, which serve as a widely used form of foundation, find extensive application in various engineering structures including buildings, bridges, wind turbines, and more [1]. The fundamental role of pile foundations is to provide structural stability by transferring loads from the superstructure through the piles into the underlying soil. The study of the performance of pile-soil systems is of paramount importance in the field of geotechnical and foundation engineering, as it is directly related to the stability and reliability of structures and infrastructure.

The design of pile foundations requires consideration of both geotechnical and structural strength requirements [2]. Geotechnical strength refers to the ability of the soil to support the loads transferred by the pile foundation without damage to the soil, while structural strength guarantees the stability of the pile under the intended loads. In addition, serviceability of pile foundations requires that total deformation and uneven settlement remain below acceptable limits.

However, engineering geological conditions have become increasingly complex, particularly those characterized by deep earth and deep-sea conditions. Pile foundation performance is significantly influenced by soil properties [3]. Different geological conditions can lead to complicated consequences within pile-soil systems. Corrosion of pile foundations in seawater or highly corrosive environments is a major challenge. In soft soils, pile foundations are susceptible to problems such as settlement and deformation. Seismic loading has the potential to induce failure in the foundation soil, causing instability within the pile foundation structure.

These challenges increase the demands on the design of the pile-soil system. With respect to piles, this demand has led to the emergence of fiber-reinforced polymer (FRP) piles, which can offer corrosion resistance, durability, and mechanical strength. In order to promote the wider use of FRP piles in marine infrastructure, the study of the interfacial behavior between pile material and soil is essential in determining the loading bearing capacity of pile foundations. With respect to the soil, the use of rubber soil mixtures (RSM) as seismic isolation systems has gained increasing attention. These mixtures are used to replace natural foundation soils, thereby reducing structural response during earthquakes and increasing foundation stability.

Consequently, to ensure the stability of the pile-soil system with FRP pile or RSM, a comprehensive understanding of the load-bearing mechanism of pile foundations and the mechanical properties of the soils surrounding the pile is essential. Such an understanding facilitates the rational analysis and design of pile foundations to meet the complexities of engineering environments.

In this thesis, the initial focus is to investigate the interface friction behavior between FRP piles and soil (including both clay and sand) using molecular dynamic (MD) simulations. This analysis aims to improve the predictive capabilities for understanding FRP pile-soil interactions. Then, MD simulations will be also used to investigate the complex interactions at the rubber-clay interface within the RSM system. The goal is to gain insight into the potential mitigating the foundation response under dynamic loading. Finally, an integrated pile-soil element is developed to efficiently simulate the nonlinearity of the soil and pile materials using the finite element (FE) method in engineering-scale problems. The formulations of this proposed method and the numerical solution procedure for calculating pile responses are provided.

The thesis is divided into two parts: Part I is devoted to theory, while Part II presents the results of the analysis and the ensuing discussion.

The first chapter provides an introduction to the pile-soil system and explains load-bearing mechanism of the pile under vertical and lateral load. It also introduces to corrosion-resistant FRP piles and discusses the complex mechanical behavior that occurs at the soil/pile interface. The chapter continues with an examination of soil types and their chemical structures, including sandy and clay soils, and an innovative ground improvement approach: the use of RSM for pile foundations.

The second chapter introduces the FE method, a numerical technique for solving complex engineering and scientific problems. The basic steps of the method are highlighted, including problem solving procedures. In addition, the discussion extends to the efficiency of using specific element types to simulate the pile-soil system. The chapter also introduces the basic process of the MD method, along with related concepts such as boundary conditions, ensembles, energy minimization, relaxation, and steered molecular dynamic. The potential function and related parameters within the ClayFF and CVFF force fields are described.

The third chapter focuses on the critical role of interface friction between FRP piles and clay in determining pile shaft resistance at the nanoscale. The geotechnical importance of the soil/pile interface shear strength for the design of FRP piles embedded in clay is emphasized. The axial load transfer behavior and shear performance between FRP and clay are investigated using MD simulation. The study focuses on the interaction between kaolinite (representative of soft clay) and epoxy in the MD simulation, investigating the effects of normal stress and sliding velocity on the friction characteristics.

The fourth chapter focuses on investigating the interfacial friction behavior between FRP piles and sand at the nanoscale using MD simulations. The aim of the study is to understand how different factors influence the friction behavior in the seawater environment. Cross-linked epoxy resin and crystalline silica substrate models are used to simulate the friction characteristics under different conditions, including the dry, pure water, and salt water systems.

The fifth chapter deals with the phenomenon of interaction between rubber and clay in RSM. The research aims to understand the mechanical properties of the RSM and support its application in improving seismic resistance and mitigating the structure response through the MD simulations study. These simulations investigate the friction behavior between rubber and clay at the rubber-clay interface within the RSM. The available experimental results are used to evaluate with the accuracy of the calculated results.

The sixth chapter focuses on the accurate prediction of pile behavior under extreme loading conditions in engineering design. It highlights the challenges of modeling pile-soil interaction and material inelasticity in conventional numerical models using a large number of elements. To address this, the chapter presents a novel approach using an integrated pile-soil element that efficiently captures structural inelasticity and nonlinearity. This element incorporates zero-length plastic hinges to account for inelastic pile behavior and soil springs to represent nonlinear pile-soil interactions. By integrating these features into the element formulation, it provides a convenient and accurate way to simulate the behavior of the pile-soil system. The chapter will provide the formulation of the proposed method and the numerical solution procedure for geometrically nonlinear analysis. The proposed method is compared with existing solutions and validated through field tests of axially and laterally loaded piles.

In the end, a summary of the thesis will be given.

Part I: Theory

Chapter 1. Overview on the pile-soil system

1.1 General Introduction about the pile foundation

1.1.1 Development of pile foundation

To address the challenges posed by inadequate foundation bearing capacity, the predominant approach is to use piles to provide essential structural support for the superstructure. This employment of piles can mitigate and minimize the settlement of the superstructure, thus ensuring the stability of the entire structure [4]. The applications of pile foundations are closely related to the development of various structures such as high-rise buildings, wide span bridges, high-speed railways, offshore platforms and others. According to the characteristics of different pile materials, piles can be classified into several categories such as timber piles, concrete piles, steel piles, and composite piles.

For centuries, timber piles (Figure 1-1(a)) have been the most commonly used pile type for a variety of large civil engineering structures [5]. The construction of timber piles is facilitated by their convenient accessibility and ease of processing and transportation. However, due to their limited load-bearing capacity and susceptibility to corrosion, timber piles have gradually been replaced by concrete and steel piles.

Concrete piles (Figure 1-1(b)), widely used in the field of pile foundations, offer the advantages of high strength, corrosion resistance, convenient construction, and economical cost. The evolution of concrete piles has been characterized by a gradual development from the initial cast-in-place concrete piles to the subsequent emergence of precast and prestressed concrete pile technologies. Concrete piles could be precast in various structural forms to meet the requirements of the applied loads and the engineering geological conditions.

Steel piles (Figure 1-1(c)) include steel H-piles, steel pipe piles, etc. Compared with concrete piles, steel piles offer superior tensile strength and reduced susceptibility to damage during handling and installation [6]. Steel pipe piles, which are constructed from seamless steel pipes, which provide excellent strength and facilitate seamless penetration during pile driving, thereby minimizing the impact on adjacent structures. However, the cost implications associated with steel piles and their inherent susceptibility to corrosion limit their use in marine environments [7, 8].

(a) Timber piles [9]

(b) Concrete piles [10]

Source: www.creativecompositesgroup.com

(c) Steel piles [11]

(d) FRP piles

Figure 1-1 Different pile types and materials

Composite piles are made of mixed materials, including concrete-steel tubular piles and fiber-reinforced plastic (FRP) piles (Figure 1-1(d)). These different types of piles offer unique advantages designed for specific engineering contexts. In recent decades, FRP has been increasingly used in a number of fields, such as geotechnical engineering [12]. The advantages of FRP piles over conventional piles are their corrosion resistance, excellent strength-to-weight ratio, and low maintenance requirements. Recently, extensive research has been conducted on various aspects of FRP piles, including their different types, structural and geotechnical properties, installation methods, and load-bearing characteristics [6, 13, 14].

Due to the increasingly complex engineering geological conditions, there is a need to develop innovative types of pile foundations, such as FRP piles, to meet construction requirements. To meet these challenges, extensive research into structural compositions, advanced materials and contact mechanisms in pile-soil systems is being carried out using numerical simulation methods.

1.1.2 Load-bearing mechanism of pile

In practice, a single pile is subjected to a variety of external forces, including axial loads from the superstructure, as well as lateral loads from various sources such as waves, wind, soil pressure, ship and vehicle impacts [15]. Based on the different load transfer mechanisms, pile foundations are divided into two basic categories: laterally loaded piles and vertically loaded piles.

In response to the application of external loads, the behavior of laterally loaded piles results in the generation of a lateral soil resistance. As shown in Figure 1-2, this resistance involves a complex interaction of active soil pressure, passive soil resistance, and horizontal friction forces between the pile and its surrounding soil. The application and design of pile foundations in projects such as harbors, pits, and bridges, where lateral loads have a significant influence on pile behavior, require careful consideration of the lateral load-bearing mechanism of pile foundations. In the field of laterally loaded pile analysis, the *p-y* curve has become a widely used and well documented tool that is prominently featured in major design codes such as the American Petroleum Institute (API) code [16]. The *p-y* curve is used to describe the relationship between the lateral deflection experienced by the pile and the corresponding lateral soil resistance. In particular, the use of *p-y* curves fitted to different soils (sand and clay) facilitates the determination of critical parameters such as lateral restraint stiffness and soil resistances. This approach plays a fundamental role in capturing the complex interaction between soil and pile and the structural response to lateral loading. The p-y curve has demonstrated its reliability in the design evaluation of laterally loaded piles.

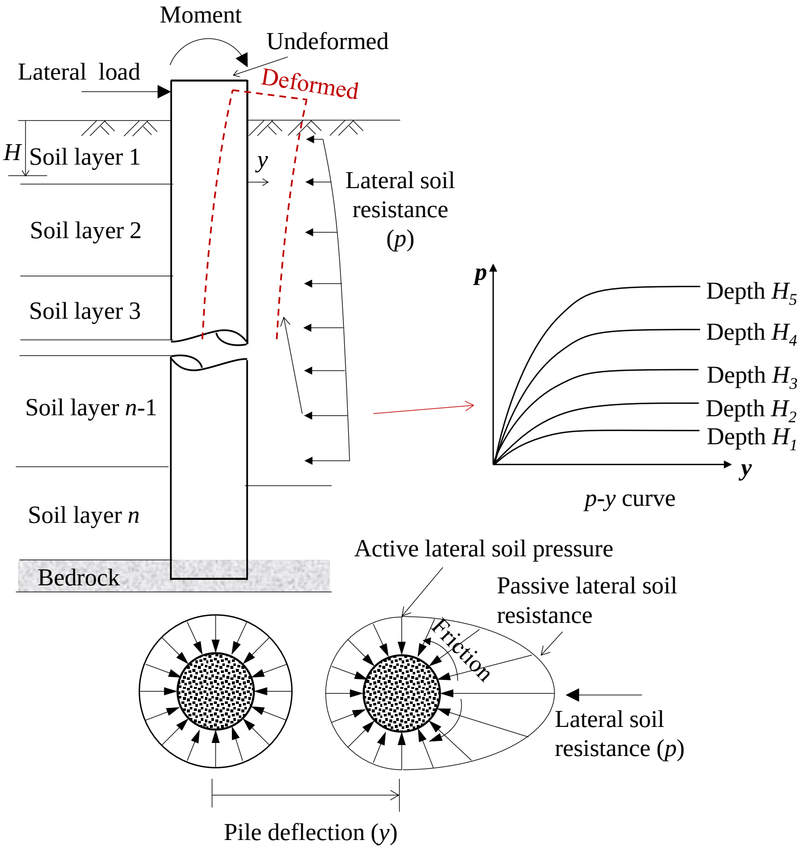

Figure 1-2 Schematic behaviors of the laterally loaded pile and its *p*-*y* curves

Vertically loaded piles experience axial displacement under axial loading, which creates axial resistance from the surrounding soil. This is manifested as vertical friction resistance along the pile length and soil resistance at the pile tip. The mechanical response of pile foundations to axial loading is primarily characterized by parameters such as settlement, axial force distribution, and axial bearing capacity. Friction piles tend to reach their ultimate limit state primarily due to soil failure surrounding the pile. Conversely, end bearing piles are more susceptible to structural limit state failures such as pile buckling, especially when the pile tip is located in hard soil or bedrock. Analogous to the well-established *p*-*y* curve for lateral load analysis, the *t*-*z* curve describes the correlation between the mobilized unit skin friction and the axial displacement along the pile length, providing critical insight into the axial load transfer mechanism within the pile-soil interface [17]. At the same time, the *Q*-*z* curve serves as a tool to capture the interaction between the mobilized ultimate bearing capacity and the axial displacement at the pile tip [18]. The failure mode of the vertically loaded piles is determined by factors such as the shear strength of the soil surrounding the pile, the bearing capacity of the soil layers, and the geometry and properties of the pile. The axial capacity of a pile is influenced by two main factors: (1) pile strength, where inadequate strength can result in compromised structural stability under load; and (2) pile-soil interaction, which causes relative displacement between the pile and the surrounding soil, ultimately resulting in soil failure around the pile. Consequently, the frictional characteristics of the pile-soil interface play a key role in pile foundation design.

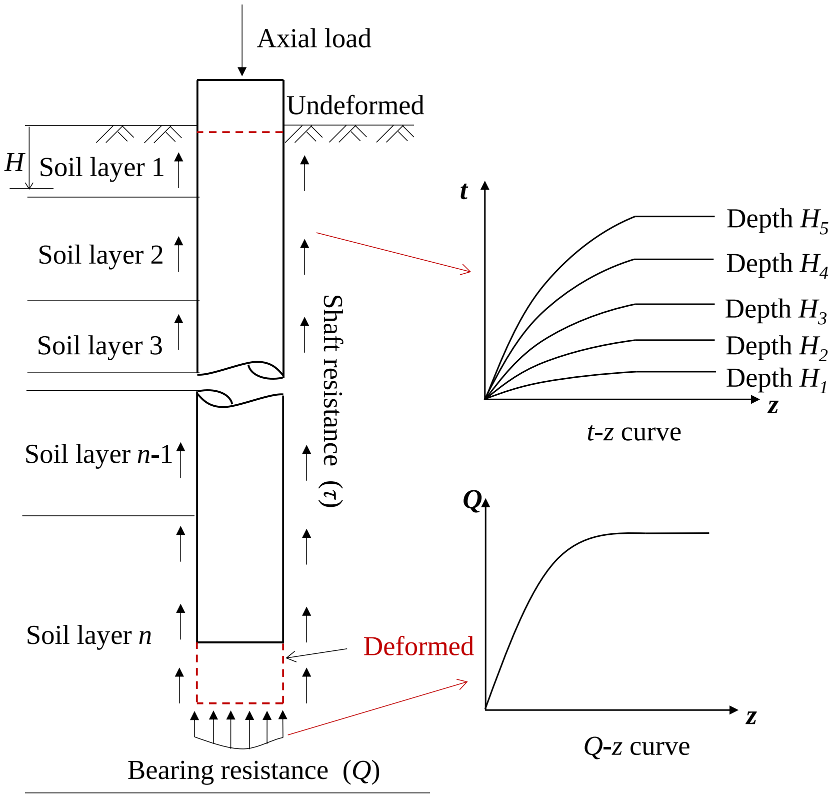

Figure 1-3 Schematic behaviors of the axially loaded pile and its *t*-*z* and *Q*-*z* curves

The pile design shall mitigate the occurrence of pile instability problems similar to those experienced in the referenced project shown in Figure 1-4. The pile-soil system must have sufficient bearing capacity and stiffness to resist external loads without excessive deformation, thereby satisfying the serviceability limit state design requirements for pile foundations. Therefore, a thorough study of the force-displacement behavior of piles under various loads is of great theoretical and practical importance. Although on-site load testing is one of the most reliable methods for determining pile capacity, pile deformation, internal forces, and soil reaction coefficients, its application is often limited by time and cost considerations. Therefore, there is a need to develop numerical simulation methods that model the laterally and vertically loaded piles to effectively address the requirements of practical engineering scenarios.

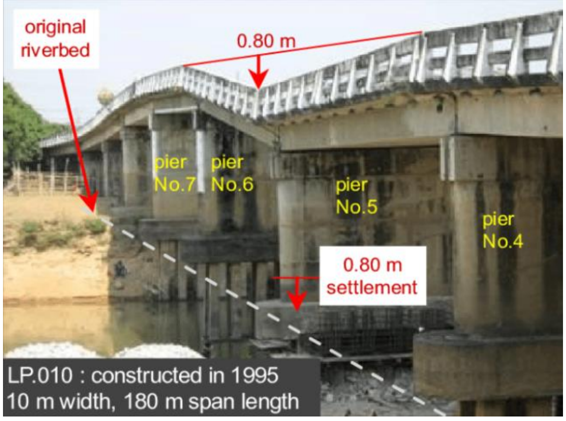

Figure 1-4 The subsidence of pile foundation leads to uneven settlement of bridge [19]

1.1.3 Characterization of the FRP pile

Different pile types such as timber, concrete, and steel piles have been used in engineering to support marine structures, but the corrosion poses a great risk to the service life of relevant infrastructures (Figure 1-5). It will lead to high maintenance costs when used in the harsh marine environment. A new type of corrosion-resistant material, FRP, provides sustainability benefits to marine infrastructures and thus experiences particular interest. FRP is a composite type of material fabricated in the form of a polymer matrix reinforced with fibers. Usually, the polymer is an epoxy, vinyl ester, or polyester, and fibers are made of glass, carbon, and aramid. The FRP pile has the potential to replace conventional pile types due to its non-corrosive nature, light weight, and superior mechanical properties [20]. However, the use of FRP composite material in geotechnical engineering was started a few years ago, and it is still somewhat limited compared to traditional materials. This is mainly because of their relatively higher initial cost, lack of database, and insufficient knowledge for these used in harsh marine environments.

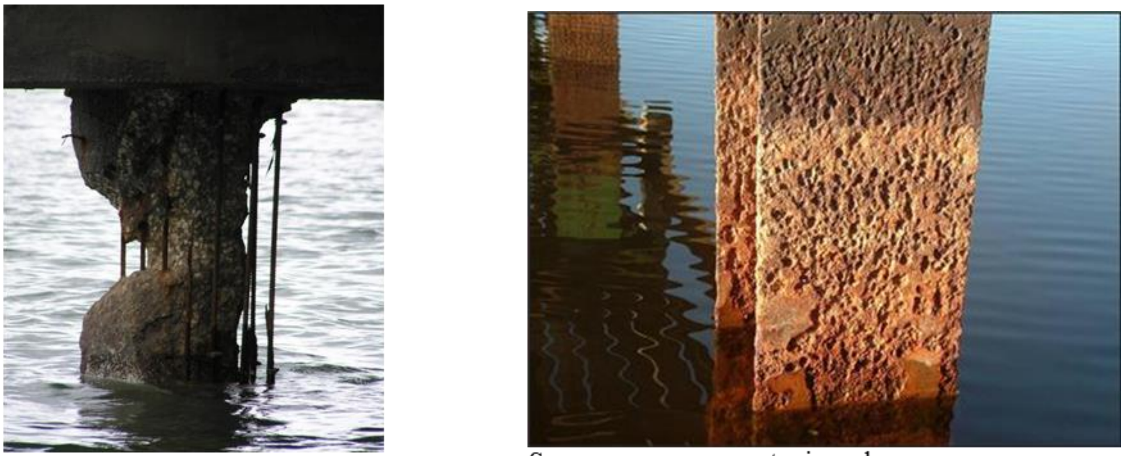

Source: www.vector-corrosion.com

Source: www.seagrant.wisc.edu

(a) Corrosion of prestressed concrete pile

(b) Corrosion of steel piles

Figure 1-5 Corrosion of conventional piles installed in corrosive and marine environments.

The vertical load transfer mechanism of the FRP pile is essential in analyzing and designing substructures [21]. The interfacial shear behavior between FRP and soil plays an important role in determining the load capacity of the foundation [22, 23]. The side friction resistance at the interface between the FRP pile and soil has a significant effect on the settlement of the foundation. Due to the high compressibility and low shear strength of marine soils [24, 25], special attention needs to be paid to settlement problems during construction. Therefore, the interface shear behavior between marine soils and FRP foundation structure should be clarified to promote wider adoption of FRP pile in marine infrastructures.

Studying the interfacial behavior between construction materials and soils is essential in foundation engineering as it is a determining factor for bearing capacities of pile foundations. Therefore, a proper pile-soil interface model plays a significant role in predicting pile behavior.

Several constitutive models have been presented for the description of the behavior of the pile-soil interface. The soil constitutive models modified from the Mohr-Coulomb model and Drucker-Prager model are commonly used. Simonini [26] presented a finite-element approach based on a elastoplastic constitutive model to predict the behavior of dense sand surrounding the pile tip in a fairly large stress range. Loukidis and Salgado [27] investigated the limit shaft resistance of ideal non-displacement piles in sands by using a two-surface-plasticity constitutive model. Basu et al. [28] also used this model to study the effects of relative density and confinement on the unit shaft resistance of piles jacked in sand. De Gennaro and Frank [29] proposed an elastoplastic interface model capable of considering phase transformation and asymptotic state of strength in sand-structure interfaces. Lashkari [30] developed an elastoplastic constitutive model to describe the dry and saturated interface behavior between granular media and structure.

The other approach is the load transfer curve (*t*-*z* curve). It is evident that the selection of a proper load transfer mechanism is the paramount issue. The load transfer curve is a simple analytical technique that can be applied in many complex situations, such as variations in the sections along a pile shaft and an inhomogeneous layered soil system. Many studies have been done using various load transfer models for the pile-soil interface, such as the concrete-soil and steel-soil interface. Chow [31] presented a simple linear load transfer curve for analyzing the behavior of vertically loaded pile groups. Since then, the more complex load transfer models such as the bilinear transfer model [32], trilinear softening model [33, 34], and nonlinear function models [35-39] were developed.

The axial pile capacities of an FRP pile and a conventional pile (e.g., timber, concrete, and steel piles), with identical dimensions and soil conditions, may be quite different due to differences in the side frictional resistance at the pile-soil interface. The above studies showed that most of the research on the shear behavior of the pile-soil interface mainly concentrates on the concrete-soil interface or the steel-soil interface, while little research has been done on the interface shear properties between FRP pile and soil.

1.2 General Introduction about soils

1.2.1 Sandy soil

Sandy soil, as a soil category, has a wide distribution in alluvial plains in China [40]. The formation of sandy soils is mainly due to geological phenomena such as weathering, erosion and sedimentation. Characterized by relatively larger particle sizes, these soils often exhibit properties of efficient drainage and high-water permeability. The engineering properties of sandy soils are closely related to variables such as particle size distribution, compaction, and moisture content. Because of their inherent mechanical properties, sandy soils have found wide application in a variety of fields, including infrastructure development, foundation engineering, and road construction.

Quartz sand

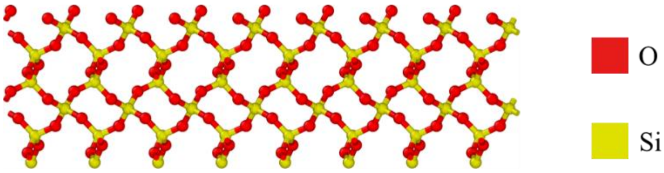

The crystal structure of Quartz

Figure 1-6 Quartz sand and the chemical structure of quartz

Quartz is one of the major important constituents of sandy soils [41]. Quartz, an abundant mineral in the earth's crust, is composed of silicon dioxide (SiO_2) units. As shown in Figure 1-6, quartz is a three-dimensional network of silicon (Si) and oxygen (O) atoms arranged in a tetrahedron. Each silicon atom is surrounded by four oxygen atoms, forming a tetrahedron. The primary interaction that holds the quartz structure together is the covalent bonds formed between the silicon and oxygen atoms. The repeating pattern of the lattice gives rise to the distinctive hexagonal symmetry of quartz crystals.

1.2.2 Clay soil

Clay minerals are a dominant component of the Earth's crust and are abundant in terrestrial, subterranean, and deep-sea environments [42, 43]. The physical and mechanical properties of different types of clay minerals vary slightly depending on their crystal structures. Layered clay minerals consist of two basic layers, silica-oxygen tetrahedra and aluminum-oxygen octahedra. These layers coalesce in two configurations: one involves a tetrahedron-octahedron bilayer structure in which tetrahedral and octahedral layers are intercalated in a 1:1 ratio, as exemplified by kaolinite; the other involves a tetrahedron-octahedron-tetrahedron arrangement characterized by tetrahedral and octahedral layers stacked in a 2:1 ratio, as exemplified by montmorillonite.

1.2.2.1 Kaolinite

As shown in Figure 1-7, kaolinite is a layered silicate mineral characterized by an alternation of tetrahedral and octahedral layers arranged in the (001) orientation. These layers are bonded by hydrogen bonds. Within the planar direction of the crystal layer, silica-oxygen tetrahedra and aluminum-oxygen octahedra form a continuous hexagonal network, forming strong interconnections. The structural layers are stacked along the *z*-axis direction and consist of primary elements such as Al, Si, O, and H. The kaolinite consists of both external and internal hydroxide group, while the tetrahedral and octahedral units are connected by shared oxygen atoms.

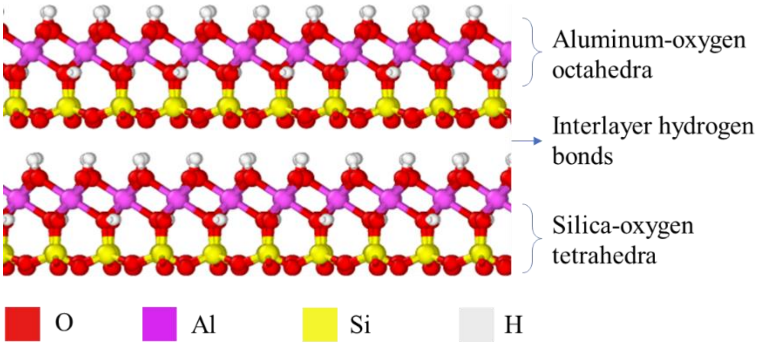

Figure 1-7 The crystal structure of kaolinite

The unit cell of kaolinite contains a single layer and exhibits two distinct surfaces: one characterized by the oxygen atoms located at the base of the silica-oxygen tetrahedra, and the other characterized by the external hydroxide group present in the octahedra. The interlayer cohesion of kaolinite is mainly due to hydrogen bonding and van der Waals forces involving hydrogen and oxygen atoms. This intermolecular interaction, which is considerably weaker than covalent and ionic bond, underscores the susceptibility of kaolinite to separate along the interlayer, resulting in the formation of thin plate-like crystals.

1.2.2.2 Montmorillonite

The physical structure of the montmorillonite particle is generally perceived in sheets and layers. As shown in Figure 1-8, monocrystalline layers of montmorillonite exhibit a sandwich arrangement characterized by two silica-oxygen tetrahedral layers enveloping an aluminum-oxygen octahedral layer [44]. These crystal layers are interconnected by van der Waals forces and electrostatic forces. The charge results from two different types of substitution: first, the substitution of Al^{3+} within the octahedral layer by ions such as Mg^{2+}, Fe^{2+}, and Fe^{3+}; second, the substitution of Si^{4+} within the tetrahedral layer by Al^{3+}. The surface of the montmorillonite mineral has an electronegative charge. Consequently, clay minerals require the adsorption of a certain number of cations to counterbalance their inherent negative charge and thereby achieve electrical neutrality.

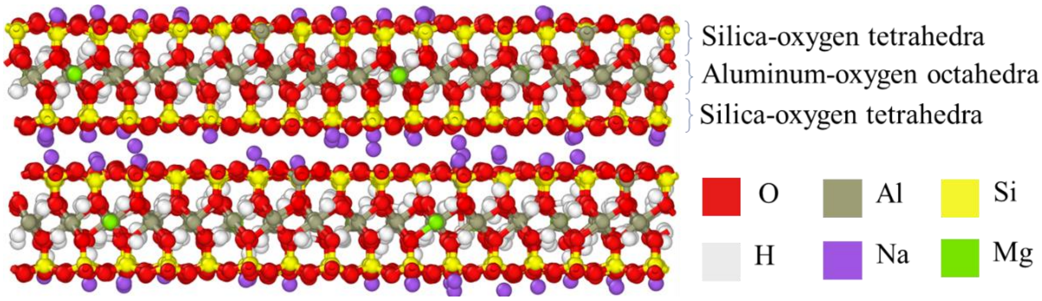

Figure 1-8 The crystal structure of montmorillonite

1.2.3 Rubber-soil mixtures

In recent years, the increasing global production of rubber tires due to the growth of motor vehicles has posed a significant challenge in terms of waste management and environmental sustainability. The recycling of discarded rubber tires has received considerable attention, driven by the need to mitigate their negative socio-economic and environmental impacts. In this context, as shown in Figure 1-9, the use of rubber-soil mixtures (RSM) as pile foundation fillers represents a compelling way to address waste management concerns of rubber and to improve the geotechnical properties of foundation soils.

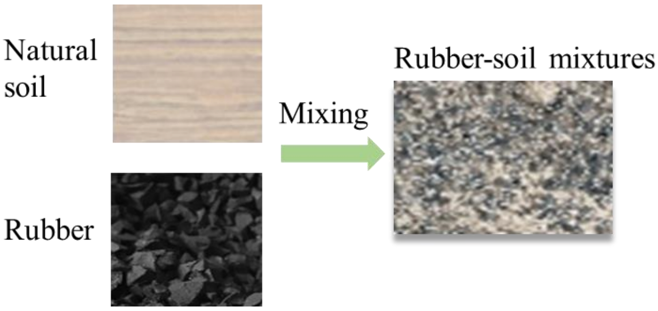

Figure 1-9 Rubber-soil mixtures

The incorporation of rubber tire particles into soil particles offers a novel approach to improving the performance of foundation soils. The use of RSM as fillers in pile foundations has gained traction due to its multiple benefits. These mixtures, which consist of a blend of soil and rubber tire granules, have unique mechanical properties that can significantly affect the behavior of the foundation. RSM have been shown to have remarkable properties such as enhanced energy dissipation capabilities [45]. These properties can translate into improved foundation performance by reducing the transmission of vibration and shock. Therefore, the nature of RSM allows structures to effectively absorb dynamic loads, making them suitable for environments where vibration and ground movement are a concern.

Chapter 2. Introduction to numerical simulation methods

The advancement of computer technology has led to the widespread use of multi-scale simulation methods in the field of civil engineering materials. Numerical simulation techniques cover a variety of time and length scales, ranging from the quantum to the macroscale. Among these techniques, molecular dynamics (MD) and finite element (FE) methods stand out as important computational tools used to address various scientific issues.

2.1 General introduction about the finite element method

2.1.1 Computational principles of the finite element method

The FE method is a widely used numerical technique for solving complex engineering and scientific problems. Fundamental to the FE method is the core concept of discretizing a continuous solution domain into a series of interconnected elements. The FE method lies in the use of approximation functions within each element. This critical phase is performed through the use of interpolation functions, resulting in an approximate solution that encompasses the entire solution domain. The element then captures local variations and allows accurate interpolation between nodes. Note that increasing the number of elements (while decreasing the element size) and increasing the precision of the interpolation function increases the accuracy of the solution approximation. By discretizing the systems, applying approximation functions, and assembling the global element matrix, the approximate solution that satisfies convergence criteria gradually approaches the exact solution using iterative solvers.

2.1.2 Basic steps of the finite element method

The process of solving problems using the finite element method involves several basic steps, which are briefly outlined below:

1. Problem Formulation: This initial step involves approximating the physical properties and geometric regions of the solution domain to suit the specific problem under consideration.

2. Solution domain discretization: The continuous solution domain is discretized into a discrete domain consisting of a finite number of interconnected elements. In particular, refining the discretization by reducing the element size improves the accuracy of the results, but at the cost of increased computational complexity and time. The choice of element type, such as beam, shell, or solid, depends on the geometry of the problem.
3. Approximation Functions: This is where the finite element formulation is derived. This involves selecting an appropriate element coordinate system, determining appropriate interpolation functions for each element, and constructing the corresponding element matrix.
4. Assembly: The process of assembling the global system of equations is performed. This assembly combines the contributions of each element. It is noteworthy that this assembly reflects the need to approximate the discrete domain of the solution domain.
5. Application of boundary conditions: In this step, the appropriate boundary conditions are imposed. The imposed boundary conditions modify the system of equations according to the constraints of the problem.
6. Solve the equations: The system of linear equations is solved, yielding approximate results for the state variables at the nodes of the elements. The accuracy of these results is evaluated by comparing them to values determined by convergence criteria. This evaluation guides the decision of whether further computations are warranted.

2.1.3 Element types for simulating the pile-soil system

The three-dimensional (3D) solid element model, depicted in Figure 2-1, employs 3D solid elements to represent both the pile and the surrounding soil. This modeling approach captures the complex soil structure and provides accurate calculations for the pile-soil interaction response.

At the same time, the use of one-dimensional element theory within the framework of the FE method is widespread. This approach involves segmentation of the pile into discrete elements, formulation of element stiffness matrices, determination of force and displacement vectors, equilibration of the distributed soil resistance on the pile with nodal forces, and culminates in the assembly of a global stiffness matrix to resolve the internal forces and deformations intrinsic to each element. The discrete spring element method, shown in Figure 2-2, introduces nonlinear spring simulations to simulate he pile-soil interaction. This technique uses load transfer curves to describe the properties of soil springs. The nonlinear soil spring model subdivides the pile and incorporates horizontal or vertical nonlinear soil springs to simulate the influence of the soil on the pile side, thus providing the parameters for pile-soil interaction. This practical approach is widely used in engineering because of its computational efficiency compared to the complications associated with the 3D solid element model.

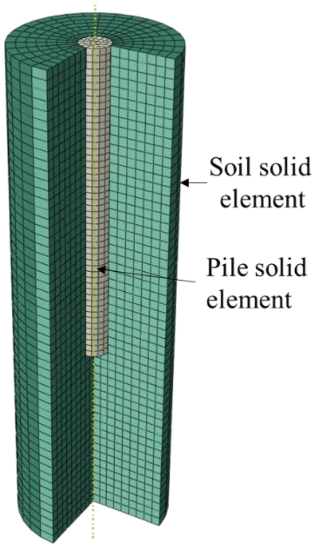

Figure 2-1 3D solid element model

In the discrete spring element model, the pile is discretized, modeled with beam elements, and connected with horizontal and vertical spring elements to capture the soil-pile interaction along the pile side. This method treats the uniform soil resistance exerted by the soil on the pile body with the concentrated forces exerted on each individual spring. However, this model has limitations, especially when dealing with highly nonlinear soil behavior. Accurate representation requires increasing the number of elements, which increases the computational burden. In addition, more nodes must be assigned to the pile body to simulate the variation of the equivalent concentrated force along its length, ensuring a more accurate representation of the soil force distribution. As a result, an accurate simulation requires a larger number of elements, which increases the computational requirements. In addition, defining the properties of each spring adds complexity to the modeling process. Therefore, it is essential to develop an efficient pile-soil integrated element method to provide an effective framework for analyzing the behavior of the pile-soil system.

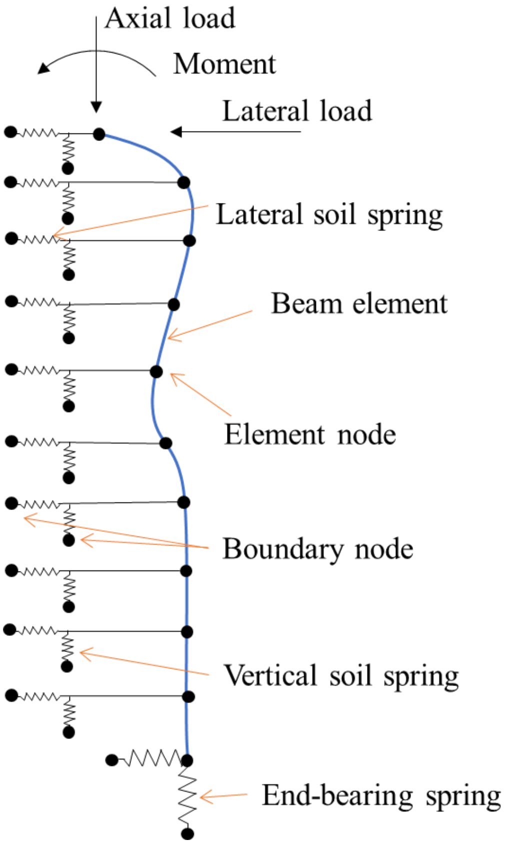

Figure 2-2 Discrete spring element model

2.2 General introduction about the molecular dynamic simulation

Nanoscale modeling and simulation methods have become a powerful tool for obtaining fundamental knowledge of mechanical properties of materials and have the potential to provide parameters for material design [46]. In recent years, the number of research works involving MD simulations of construction materials has grown significantly [47]. The MD method, which serves as an effective computational experiment to characterize material properties and to predict mechanical responses, has been widely used in civil engineering [48-52].

2.2.1 The basic process of molecular dynamics

The basic principle of MD methods is the application of classical Newtonian mechanics to atomic or molecular systems. In this approach, the Newton's equations of motion are solved by integral algorithms, yielding temporal evolutions of their configurations. Due to the complex interaction potentials between atoms, the analytical solution for the equations of motion is challenging. Consequently, finite difference method is often employed. A finite time interval (Δt) is introduced to discretize the continuous motion of atomic nuclei. This time step allows numerical integration of the equations of motion and replaces the concept of an infinitesimal time element ($\mathrm{d}t$). For every time step, each particle's position r and velocity v may be integrated with a symplectic method such as Verlet algorithm. The time evolution of r and v is called a trajectory. Given the initial positions and velocities, we can calculate all future positions and velocities. The basic procedure of molecular dynamics can be outlined as follows:

1) Construction of atomic model: obtain initial positions r_0.
2) Specification of force field: Characterize the interactions between particles confined by the force field and calculate potential energy U, which is a function of r.
3) Calculation of the force F: Derive the forces acting on each atom by differentiating its potential energy U with respect to its coordinates r.
4) Determination of acceleration a: Use the principles of classical mechanics, along with the known masses of each atom, to determine the acceleration of each atom.
5) Motion integration: Integrate the acceleration by selecting an appropriate time step Δt. This yields new velocities and displacements for each atom through successive primary and secondary integrations.
6) Configuration update: Update the atom positions to generate a new system configuration.

The above steps 3 to 6 are performed iteratively over a defined time interval until a predetermined time period is reached, which marks the end of the simulation. During the course of the MD simulation, atomic attributes such as coordinates, displacement, velocity, and acceleration are computed for each instance. These atomic details are then sampled and statistically averaged, culminating in a set of thermodynamic quantities that include temperature, pressure, energy, and stress within the material. Based on statistical mechanics, these long-term average behaviors of a limited number of particles can infer the instantaneous average behavior of a much larger collection of particles, i.e., macroscopic physical properties. The flow diagram of MD calculations is presented in Figure 2-3.

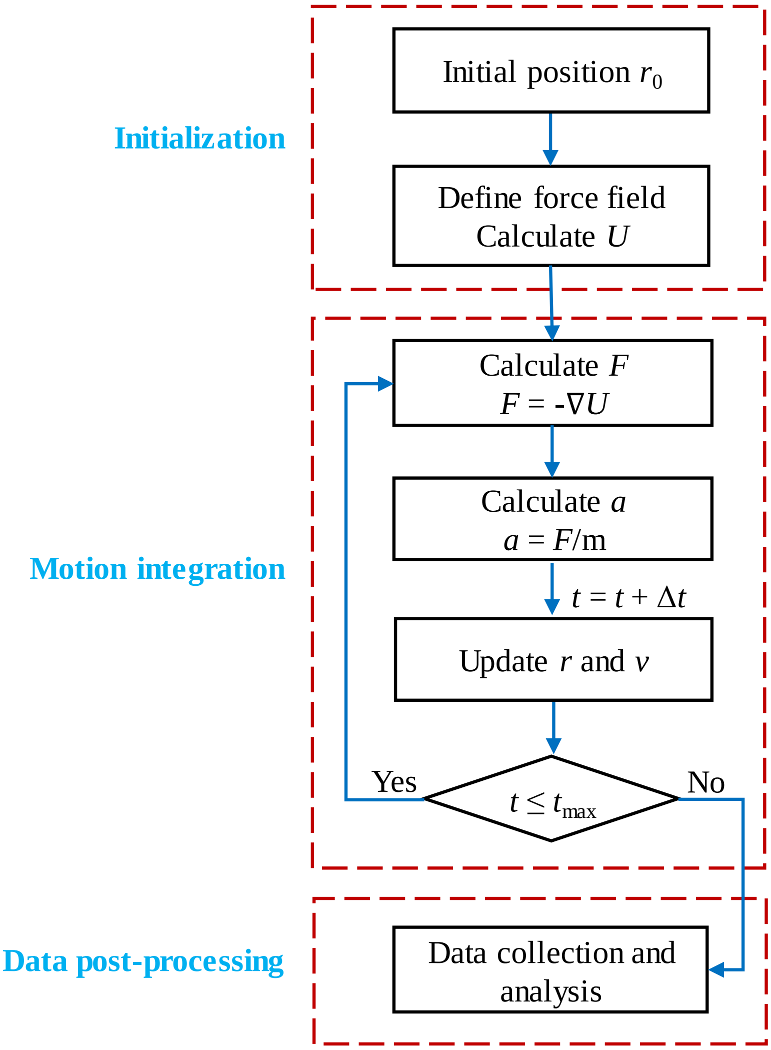

Figure 2-3 The flow diagram of the Molecular Dynamics method

2.2.2 Modeling and boundary conditions

For modeling inorganic materials, the spatial coordinates of the atoms within the lattice should first be determined using structural information of the material, typically obtained from X-ray diffraction experiments. For organic materials, the model can be constructed from their chemical structure. Usually, the unit cell or unit chain should be reduplicated to an appropriate size to represent the material.

Due to the limitations of computational resources and capabilities, achieving the equivalent scale of macroscopic materials within molecular dynamics models remains a huge challenge. To eliminate the limitations imposed by the size effect, the selection of representative cells of reasonable dimensions is necessary. Typically, the choice of cell dimensions, guided by convergence tests, depends on the various factors such as the complexity of the microstructure and composition of the material, and the objectives of the research. The implement of periodic boundary conditions can overcome surface effects and limit of model size, achieving the simulation of macroscopic material properties.

Three-dimension periodic boundary conditions are particularly useful for simulating a bulk system with no surfaces present. Furthermore, when simulating planar surfaces, two-dimension (e.g., X and Y) periodic boundaries are often used, while leaving the third (e.g., Z) direction with different boundary conditions. such as remaining vacuum to infinity.

2.2.3 Energy minimization

Initial structures obtained from X-ray diffraction experiments often show interactions with high energy levels. Achieving a stable configuration for the system typically requires an initial phase of energy minimization. At absolute 0 K, kinetic energy is neglected, and a lower potential energy can be achieved by adjusting the atomic configuration, specifically the positional arrangement of the particles, to eliminate unstable conformations. The minimization process culminates in a structure with the lowest achievable energy level. The relaxation process then incorporates the consideration of kinetic energy by performing MD simulations within a predefined system. After a certain amount of simulation time, the thermodynamic information of the system and the corresponding physical quantities stabilize and converge.

2.2.4 Force field

The force fields are used to characterize the interactions between atoms and molecules. The choice of a suitable force field involves defining potential energy formulas and associated parameters for each atom, thereby capturing the forces that govern their interactions. It is crucial for the accuracy of the simulation results.

The Consistent Valence force field (CVFF) [53] and CLAYFF [54] are the most widely used force fields for organic components and phyllosilicate minerals, respectively. In these force fields, the total potential of the system $U(r_{\mathrm{ij}})$ is the sum of non-bonded and bonded potentials. The non-bonded potentials include van de Waals (VDW) interactions and coulomb interactions (see Eq. 2.2). The VDW potentials are calculated by 12-6 Lennard-Jones (LJ) potential model. The bonded potentials consist of energies formed between valence bonds, angles, dihedral angles and out-of-plane angles.

$$U(r_{ij}) = U(r_{ij})_{\text{non-bonded}} + U(r_{ij})_{\text{bonded}} \tag{2.1}$$

$$U(r_{ij})_{\text{non-bonded}} = \sum_{\text{VDW}} 4\varepsilon_{ij}\left[\left(\frac{\sigma_{ij}}{r_{ij}}\right)^{12} - \left(\frac{\sigma_{ij}}{r_{ij}}\right)^{6}\right] + \sum_{\text{Coul}} \frac{1}{4\pi\varepsilon_0\varepsilon_r}\frac{q_i q_j}{r_{ij}} \tag{2.2}$$

$$U(r_{ij})_{\text{bonded}} = \sum_{bond}\frac{1}{2}K_{r,ij}\left(r_{ij} - r_{0,ij}\right)^2 + \sum_{\text{angle}}\frac{1}{2}K_{\theta,ijk}\left(\theta_{ijk} - \theta_{0,ijk}\right)^2 + U_{Dihedral} + U_{out-of-plane} \tag{2.3}$$

where r_{ij} is the distance between particle i and j. $\varepsilon_{\mathrm{ij}}$ is the depth of the potential well and σ_{ij} is the distance at which the inter-particle potential is zero. LJ parameters $\varepsilon_{\mathrm{ij}}$ and σ_{ij} are obtained from Lorentz-Berthelot (LB) mixing rules [55], as shown in Eq. 2.4.

$$\sigma_{ij} = \frac{\sigma_i + \sigma_j}{2},\ \varepsilon_{ij} = \sqrt{\varepsilon_i \varepsilon_j} \tag{2.4}$$

2.2.5 Ensembles

The concept of statistical mechanics holds that the statistically averaged state of all constituent atoms within the system provide insight into the macroscopic properties of a system (such as temperature, pressure, and density). The thermodynamic state of a system is usually defined by a small set of parameters, such as the number of particles *N*, the temperature *T*, the pressure *P*, the energy *E*, the stress σ, and the chemical potential μ. The selection of ensemble for the simulated system depends on the computation of intended physical quantities and the experimental conditions under which these computations are performed.

The simulated system can be broadly classified into two primary categories: closed systems with a constant number of particles, including the microcanonical ensemble (NVE), the canonical ensemble (NVT), and the isothermal-isobaric ensemble (NPT); and open systems characterized by a variable number of particles, exemplified by the grand canonical ensemble (μVT). In the NVE system, the simulated environment remains adiabatic, with constant particle number, volume, and energy. An NVE molecular dynamics trajectory may be seen as an exchange of potential and kinetic energy, with total energy being conserved. The NVT system maintains constancy in particle number, volume, and temperature. The energy of endothermic and exothermic processes is exchanged using a Nosé-Hoover thermostat. Other techniques for temperature control include velocity calibration, Berendsen thermostat, and Langevin dynamics. The NPT system maintains constancy in particle number, pressure, and temperature. It is most commonly used under laboratory conditions at room temperature and pressure. Alternatively, the constant temperature and enthalpy (NσT) system, similar to NPT, is rarely used in practice. The μVT regime is mainly used in Monte Carlo methods where the chemical potential is kept stable by modulating the particle number, a strategy that is difficult to apply in molecular dynamics simulations.

2.2.6 Steered molecular dynamics

Steered molecular dynamics (SMD) [56] is a computational technique used to study the force-induced deformation of molecules. SMD simulations are widely used to study the mechanical properties and behavior of atoms under external forces. An external force is applied to specific atoms or groups of atoms in the SMD simulation. The equations of motion for the system are integrated as in traditional MD simulations, with the additional consideration of the applied external force. The dynamics of the system are governed by Newton’s equations of motion, taking into account both the internal interactions within the atoms and the externally applied forces. Throughout the simulation, atomic behavior can be monitored and analyzed, which provides valuable insights into the response of the atom subjected to mechanical forces and can be compared to experimental data.

The basic idea of SMD simulation is to apply an external force to the SMD atoms by a virtual spring with a spring constant. By pulling the SMD atoms with a constant velocity or force and holding another set of atoms fixed, relative motion can be simulated. In constant force SMD simulations, constant forces are applied to selected atoms in a given direction. On the other hand, a constant velocity SMD simulation applies a constant velocity to one or more selected atoms.

Part II:
Results

Chapter 3. Soil resistance on fiber-reinforced polymer pile: role of clay minerals

Abstract

Due to the geotechnical design requirements of the fiber-reinforced polymer (FRP) pile embedded in clay, interface friction evolution between the FRP pile and clay plays a crucial role in determining the pile shaft resistance. It is observed from the experimental evaluation that the earth pressure and shear rate affect the pile-soil interface behavior. Existing investigations are limited to the macroscale and have not been well established at the nanoscale for interface friction behavior between FRP (epoxy) and clay (kaolinite). In this study, a cross-linked epoxy resin is created to contact a siloxane surface of kaolinite in the molecular dynamic simulation. The interfacial accommodation between kaolinite and epoxy resin is studied. In order to investigate the effect of normal stress and sliding velocity on nanoscale friction characteristics, the steered molecular dynamics is utilized to simulate the sliding of the kaolinite model on the surface of the epoxy resin. Simulation results show that the calculated peak interface shear coefficient decreases nonlinearly as the normal stress increases, which follows a logarithmic relationship consistent with the FRP-soil interface shear test. On the other hand, it is observed that two distinct velocity regions, slow pulling mode (5 to 200 m/s) and fast pulling modes (300 to 800 m/s), are well fitted by extended Bell theory. The stick-slip motion is only found in slow sliding velocity mode. This increasing tendency of the energy barrier with the normal stresses indicates that higher pulling forces are required for the FRP to slide along the soil at higher normal stress. The present work provides a fundamental understanding of the friction mechanisms between kaolinite and epoxy resin.

Keywords: FRP pile; kaolinite; epoxy; interface friction; molecular dynamics.

3.1 Introduction

Conventional timber, concrete, or steel piles are widely used to support offshore structures. However, corrosion of steel and degradation of concrete and timber have become major problems. These materials have a limited lifespan and huge maintenance costs in harsh environments. In recent decades, fiber-reinforced polymer (FRP) pile has been increasingly used in civil engineering [57, 58]. The FRP materials offer high strength, lightweight, durability, and resistance to corrosive environments, providing a longer service life than conventional pile material [59, 60]. FRP composite materials are typically composed of a reinforcement, such as carbon or glass, and a polymer matrix, such as epoxy, polyester, or vinyl ester resin. Epoxy is a commonly preferred matrix due to its exceptional mechanical properties and adhesive bonding characteristics in FRP structures [61, 62].

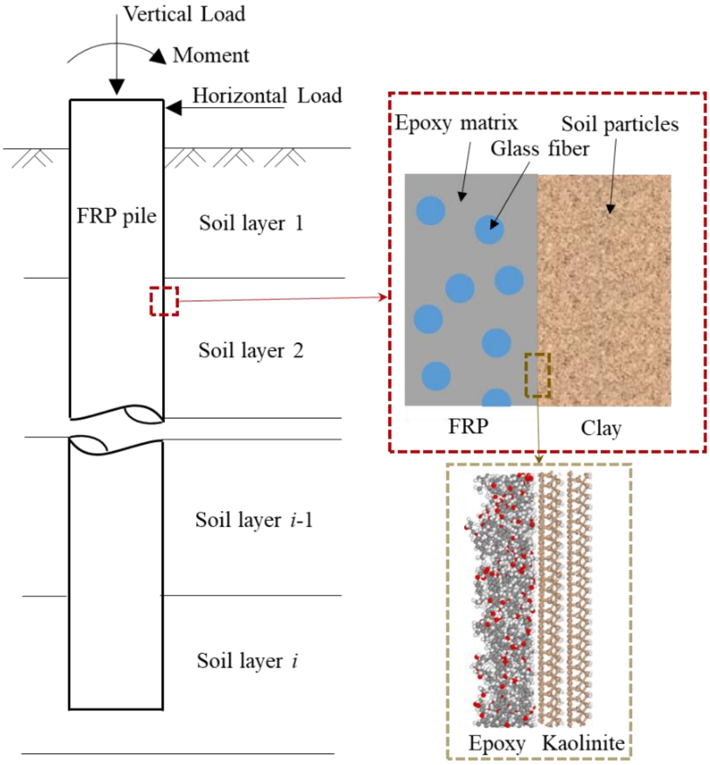

Figure 3-1 Schematic diagram of interface between FRP pile and surrounding soil from macroscale to nanoscale

In order to accurately study the friction behavior of pile-soil interaction in civil engineering applications, it is necessary to determine the interface shear strength characteristics between soil and pile [60]. As shown in Figure 3-1, when a pile is subjected to an axial load, the soil will have shaft resistance and pile tip resistance. The effect of pile tip resistance on the bearing capacity is usually neglected, especially in soft soils. In such a case, the bearing capacity is considered to be exactly equal to the shaft resistance. Soft clay is widely deposited in the eastern coastal area of China [63]. Therefore, it is essential to have a fundamental understanding of the interface shear strength in the geotechnical design of the FRP pile embedded in clay.

To promote the use of the FRP pile as the load-bearing pile, several researchers have conducted experiments to study the shear behavior between FRP and clay. One such study was conducted by Giraldo and Rayhani [21], who investigated the performance of FRP piles in soft clay. They compared the axial load transfer behavior of FRP piles with that of steel piles and found that the surface topology, pile texture, and waviness pattern of FRP piles have a significant impact on their axial capacity. Additionally, Giraldo and Rayhani [64] investigated the frictional performance of hollow FRP piles in clay and found that the compressive capacity of FRP piles is 40% higher than that of steel piles, indicating the feasibility of using FRP piles as an alternative to steel piles in soft clay. Hosseini [65] studied the seismic performance of hollow FRP piles compared to traditional piles in soft clay using shaking table tests. From a micromechanical perspective, the shear behavior between FRP and soil is attributed to the preferred orientation of particles and contact forces between them [66, 67]. Several researchers, including Frost and Han [68], Pando et al. [69], and He et al. [70], have investigated the effect of applied normal stress or sliding velocity on the shear behavior of the FRP-sand interface through shear tests. However, there is a limited amount of research investigating the impact of normal stress and sliding velocity on the FRP-clay surface through mechanical experiments. On the other hand, due to the scale and precision required to study these phenomena, it is difficult to explain some of these effects solely with macroscopic experiments.

Molecular dynamics (MD) simulations are regarded as an excellent tool for understanding the interface shear strength characteristics [71-73]. The shear behavior of epoxy resin interfaces with various other materials under different pulling forces or velocities, such as the carbon fibers [74, 75], carbon nanotube-polymer [76], silica substrate [77, 78], calcium silicate hydrate [79], and graphene [80], have been studied. Kim and Kim [81] investigated the moisture related hygroscopic characteristics and mechanical properties of polymer-clay nanocomposites (PCNs) using MD simulations as a function of the weight fraction of nanoclay. This PCNs structure consist of epoxy and nanoclay. Van et al. [82] presented a novel molecular model approach to investigate the morphology and thermomechanical properties of PCNs. Chen et al. [83] characterized the interfaces in PCNs via the manner of fracture mechanics. They revealed that the chain length of surfactants played an essential role in the mechanical performance of these interfaces. The above MD studies mainly focus on the mechanical properties of the PCNs. The shear strength characteristics between epoxy (surface of FRP pile) and clay have not been studied at nanoscale.

In order to promote the wide use of newly developed FRP piles in clay, the research focus on the shear behaviors of the FRP pile-soil interface using the MD simulation method. Kaolinite is a prevalent clay mineral commonly found in soft soils, along with other clay minerals such as smectite, chlorite, and illite [84, 85]. It is reported that surface sediments in the Pearl River drainage basin in southern China are mainly composed of kaolinite (35%-65%), with smaller quantities of chlorite (20%-35%) and illite (12%-42%), while smectite is uncommon (<5%) [86]. For the present study, kaolinite has been selected as a representative of kaolinite-dominated soft clay. The kaolinite/epoxy surface model herein will be constructed as the FRP-clay coating layer interface. The kaolinite is subjected to an external force along the epoxy in the steered molecular dynamics (SMD) simulation. A critical mechanical parameter, the peak interface friction coefficient, will be obtained to study the effects of normal stress in the interface friction process. The extended Bell theory is used to calculate the energy barrier with different sliding velocities. The simulation results aim to provide an explanation of the friction mechanism between the FRP-clay interface.

3.2 Model construction and simulation details

3.2.1 Force field

LAMMPS [87] code is used for molecular dynamics simulations in this work. The Consistent Valence Forcefield (CVFF) [53] and CLAYFF [54] are used to determine the atomic interaction of epoxy and kaolinite, respectively. Interaction between epoxy and kaolinite is controlled by non-bonded VDW and Coulombic interaction. Both CVFF and CLAYFF use 12-6 Lennard-Jones (LJ) expressions for the VDW potential energy, which is given by:

$$E_{LJ} = 4\varepsilon_{ij}\left[\left(\frac{\sigma_{ij}}{r_{ij}}\right)^{12} - \left(\frac{\sigma_{ij}}{r_{ij}}\right)^{6}\right] \tag{3.1}$$

where r_{ij} is the distance between two types of atom i and j; The LJ parameters between two atom types i and j are denoted as σ_{ij} and ε_{ij}. To calculate these parameters, the Lorentz-Berthelot (LB) mixing rule, as shown in Eqs. 3.2 and 3.3, is employed. This mixing rule is widely utilized in both the CVFF and CLAYFF for determining the LJ parameters (σ_{ij}, ε_{ij}) [88-90].

$$\sigma_{ij} = \frac{\sigma_i + \sigma_j}{2} \tag{3.2}$$

$$\varepsilon_{ij} = \sqrt{\varepsilon_i \varepsilon_j} \tag{3.3}$$

The cut-off distance of non-bonding interaction between two atoms is set as 10 Å. The long-range electrostatics are obtained by the particle-particle particle-mesh (PPPM) algorithm [91] with a tolerance of 10^{-4}. The timestep value is 1.0 fs, and the Nosé-Hoover thermostat [92] is employed to control the temperature throughout the whole simulation.

3.2.2 Kaolinite model

As shown in Figure 3-2(a), kaolinite consists of a repeating layer of one octahedral alumina sheet and one tetrahedral silica sheet. The composition of the unit cell is $Al_2Si_2O_5(OH)_4$, and its lattice parameters used in this work are a = 5.154 Å, b = 8.942 Å, and c = 7.391 Å with α = 91.93°, β = 105.05°, and γ = 89.80° [93]. A periodic 12a × 4b × 2c kaolinite supercell is constructed by replicating the unit cell in x-, y- and z-directions. A kaolinite substrate (total 3264 atoms) with the size of $x = 61.8$ Å, $y = 35.8$ Å, $z = 14.8$ Å is shown in Figure 3-2(b). The *x*-, *y*- and *z*-directions are related to the crystal directions (100), (010), and (001), respectively. The (001) surface of kaolinite is the basal plane and the main exposed surface of kaolinite crystals [94]. Two stable surfaces of kaolinite, denoted as hydroxylated and siloxane (001) surfaces, will be regarded as the potential contact surfaces with the epoxy resin in the simulation model.

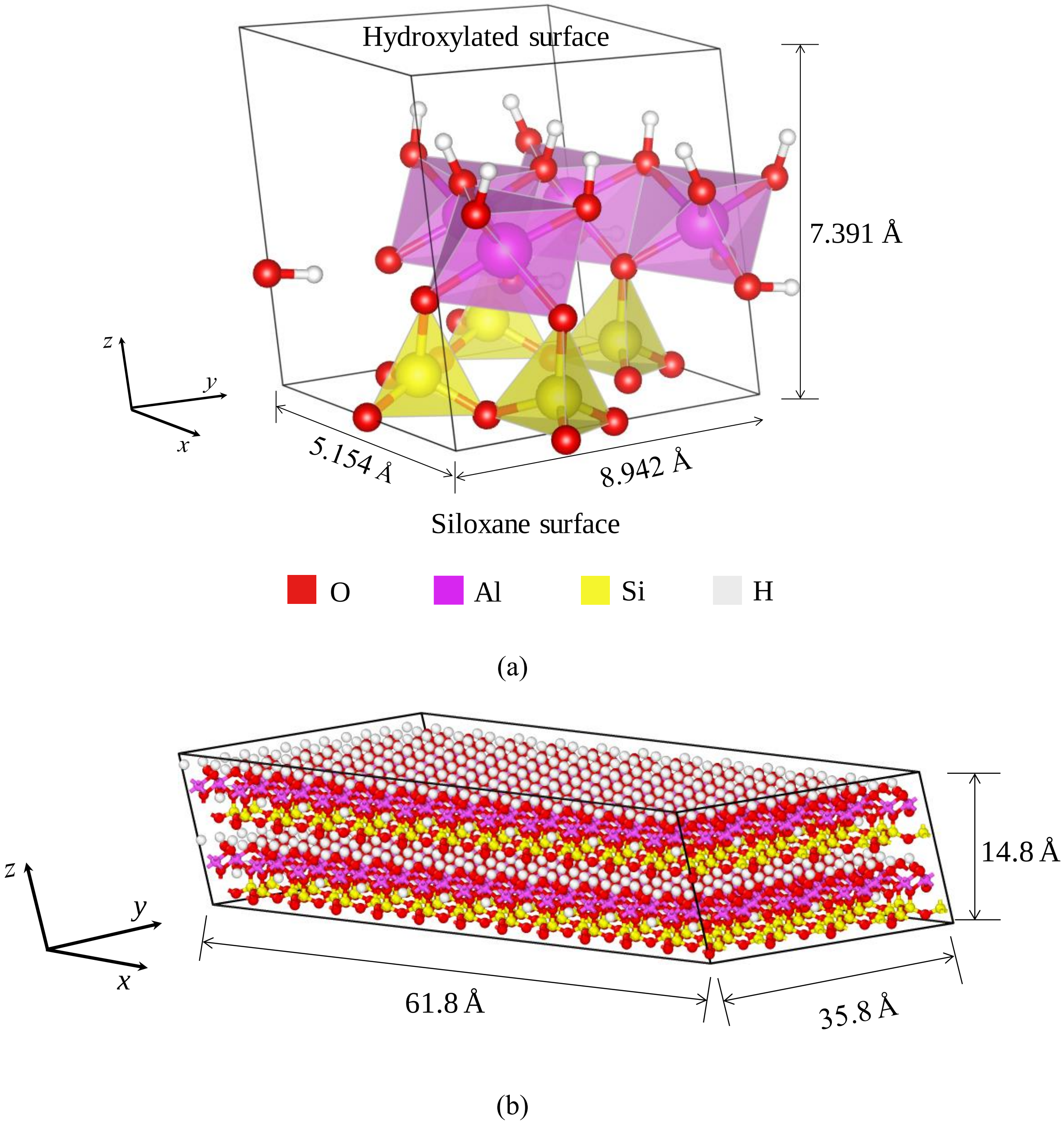

Figure 3-2 The molecular structure of (a) the kaolinite unit cell and (b) the 12a × 4b × 2c kaolinite supercell

3.2.3 Surface energy of kaolinite

Kaolinite has two different surfaces, one is hydroxylated surface and the other is siloxane surface in the *z*-direction. As shown in Figure 3-3, two different models are constructed to find the most stable surface of kaolinite in the (001) surfaces. The difference of total energy between the two equilibrated states 1 and 2 per unit contact area is the surface energy of the contact surface, which is defined as

$$E_{surface} = \frac{E_{\mathrm{state2}} - E_{\mathrm{state1}}}{2A} \tag{3.4}$$

where A is the area of the contact surface; and, E_{state1} and E_{state2} are the total energy of before and after separation, respectively.

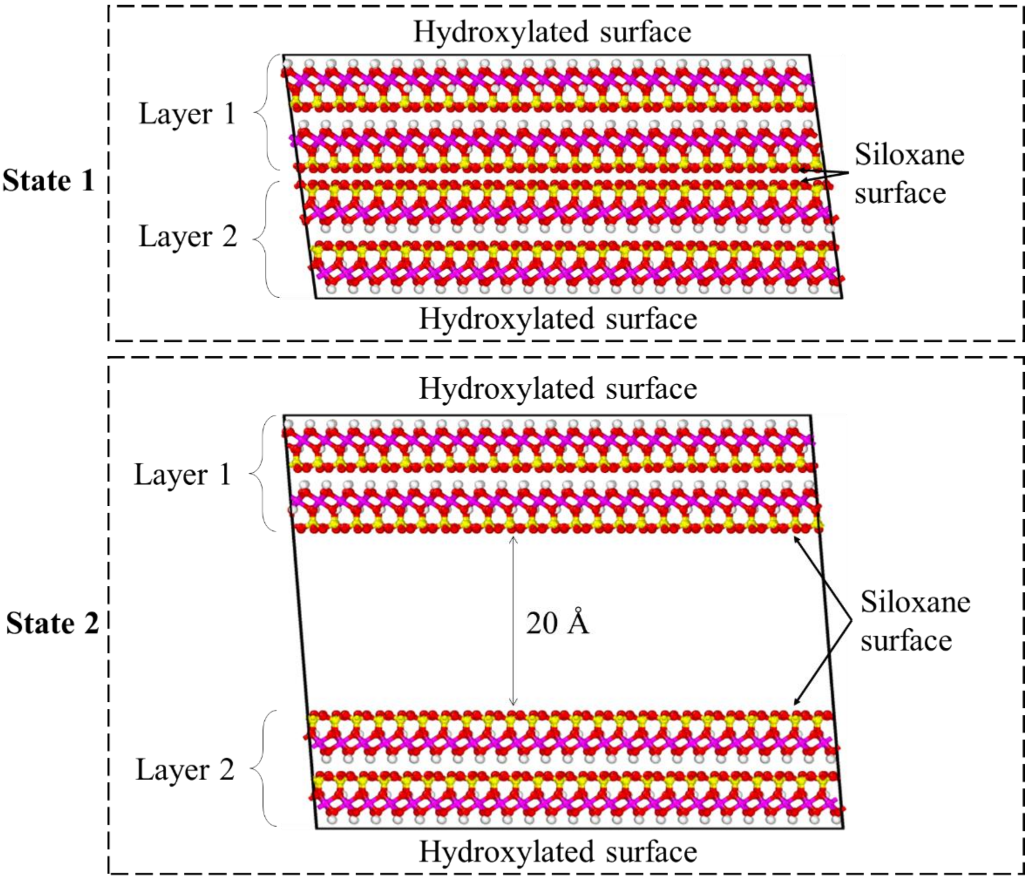

(a)

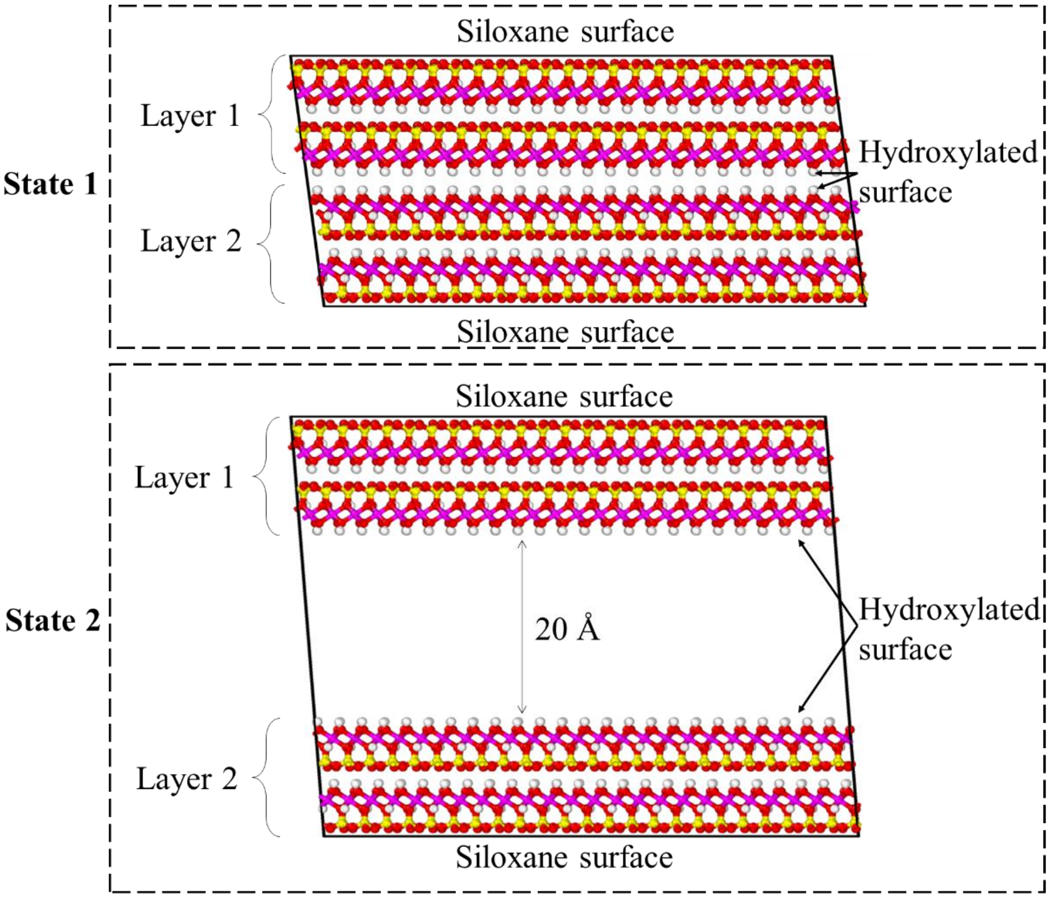

(b)

Figure 3-3 Schematics of the calculation of surface energy for two different kaolinite surfaces (a) Siloxane surface (b) Hydroxylated surface

Four kaolinite models in Figure 3-3 are equilibrated for 1 ns with a time step of 1.0 fs with the NVT (constant Number, Volume and Temperature) ensemble. The curves of total energy versus time are plotted in Figure 3-4.

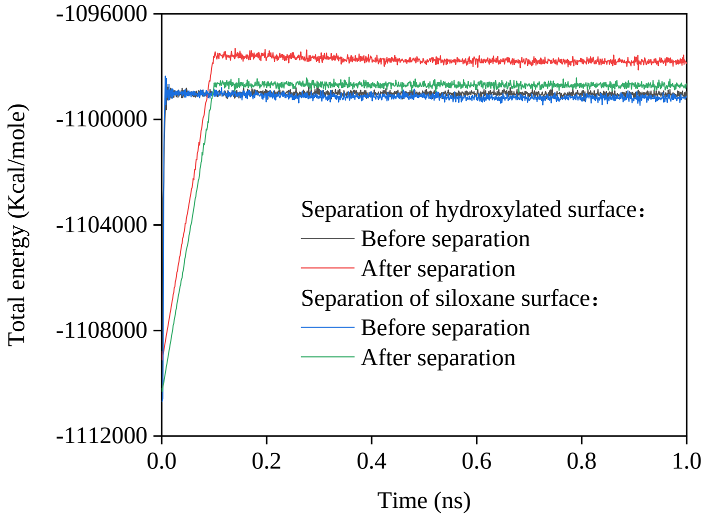

Figure 3-4 Total energy of kaolinite versus simulation time in different states

The surface energy of kaolinite for siloxane and hydroxylated surfaces are presented in.Table 3-1. The average value of 134.7 mJ/m^2 is found in agreement with results of the density functional theory (DFT) [95]. It can be seen that the surface energy of the siloxane surface is smaller than the hydroxylated surface, which indicates that the siloxane surface is a stable surface. Therefore, the siloxane surface of the kaolinite model is chosen as the contact surface with epoxy resin in this work.

Table 3-1 Surface energy of kaolinite

	This work			DFT [95]
	Siloxane surface	Hydroxylated surface	Average value	
Surface energy (mJ/m^2)	74.3	195.1	134.7	132.3

3.2.4 Cross-linked epoxy model

As shown in Figure 3-5, representative cross-linked molecules of the epoxy resin are composed of diglycidyl ether of bisphenol A (DGEBA) and triethylenetetramine (TETA), which have been widely used in previous studies [96-99]. Each TETA molecule can react with up to six molecules of DGEBA, and ideal composition ratio for DGEBA/TETA in the cross-linked epoxy resin is 6:2 [100]. In this work, 48 molecules of DGEBA and 16 molecules of TETA are constructed. The epoxy model contains 2800 atoms with a size of 61.8 Å × 35.8 Å × 40.0 Å. In the cross-linking process, the reactive CH_2 site is generated from the broken C–O bonds in the epoxide group of DGEBA. The C-N covalent bonds are created between C atoms in epoxide groups of DGEBA and N atoms in nitrogen groups of TETA when the reactive distance is less than 5 Å, which falls within the reasonable range of 3 to 10 Å reported in previous studies [101, 102]. The final conversion from DGEBA and TETA into the final cross-linking epoxy model is 75%, which has also been reported in previous research [103-105] as an acceptable conversion rate. The detailed cross-linking process can be found in reference [105].

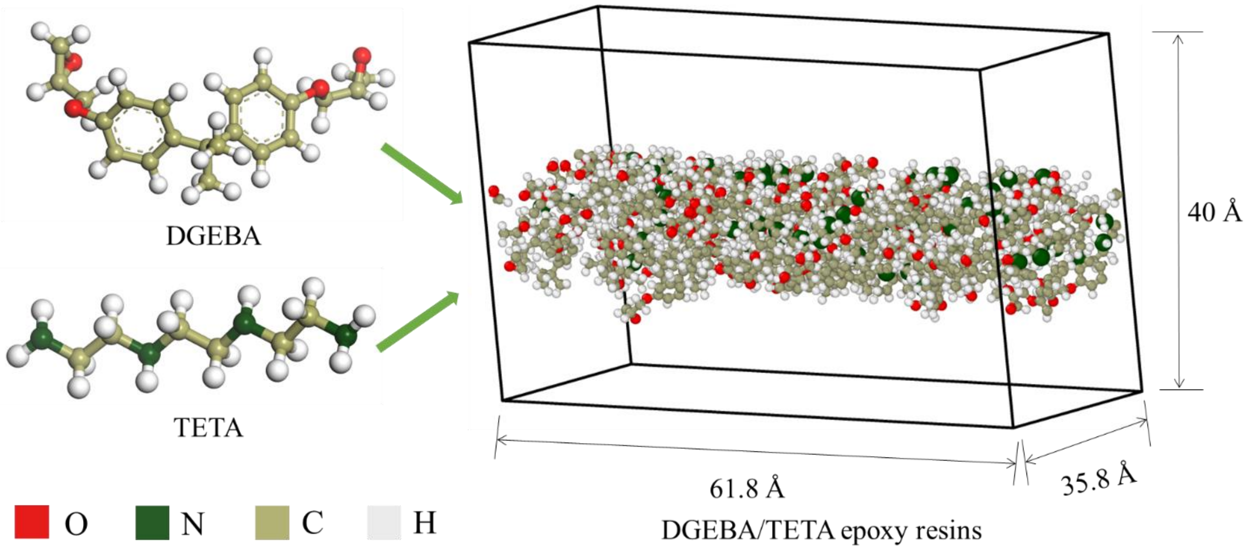

Figure 3-5 Model of the cross-linked epoxy resin

Figure 3-6 shows the density of the cross-linked epoxy model with the variation of temperature (T) from 250 K to 600 K. Two linear regions in this curve correspond to the glass and rubber states of the polymeric material, respectively. The abrupt change in the slope of the density-temperature curve determines the glass transition temperature (T_g) of the cross-linked epoxy. The system is equilibrated under NPT ensemble for 1 ns, and the density data is collected after the 0.5 ns equilibrium procedure, which is presented in Figure 3-6. The data at temperature above and below T_g are fitted using the linear regression. Coefficient of thermal expansion (CTE) is calculated from the slopes of volume change curves. The volumetric CTE for both glassy and rubbery is obtained from the slope of the two curves as their equations are shown in Figure 3-7. The volumetric CTE (α) and the linear thermal expansion coefficient (β) are given by

$$\alpha = \frac{1}{V}\left(\frac{\partial V}{\partial T}\right)_P \tag{3.5}$$

$$\beta = \frac{\alpha}{3} \tag{3.6}$$

where T is the temperature; P is the pressure; and, V is the volume. The value of T_g, ρ, α_1, β_2, α_1, and β_2 obtained by simulations and experiments are collected in Table 3-2. It can be seen that those values in this work have good agreement with the results of MD simulations and experiment, indicating the validity of the epoxy model.

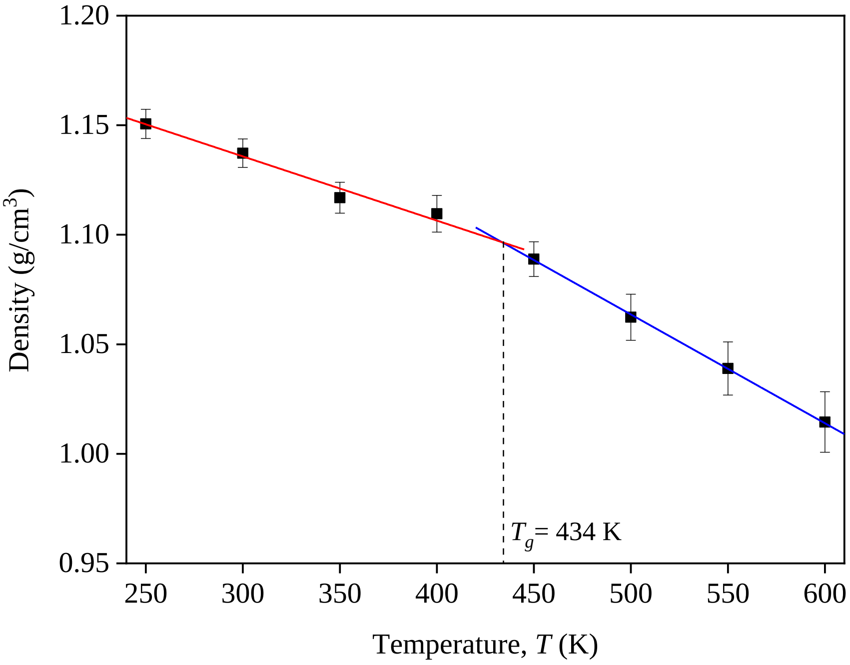

Figure 3-6 Density of DGEBA/TETA epoxy system with the variation of temperature

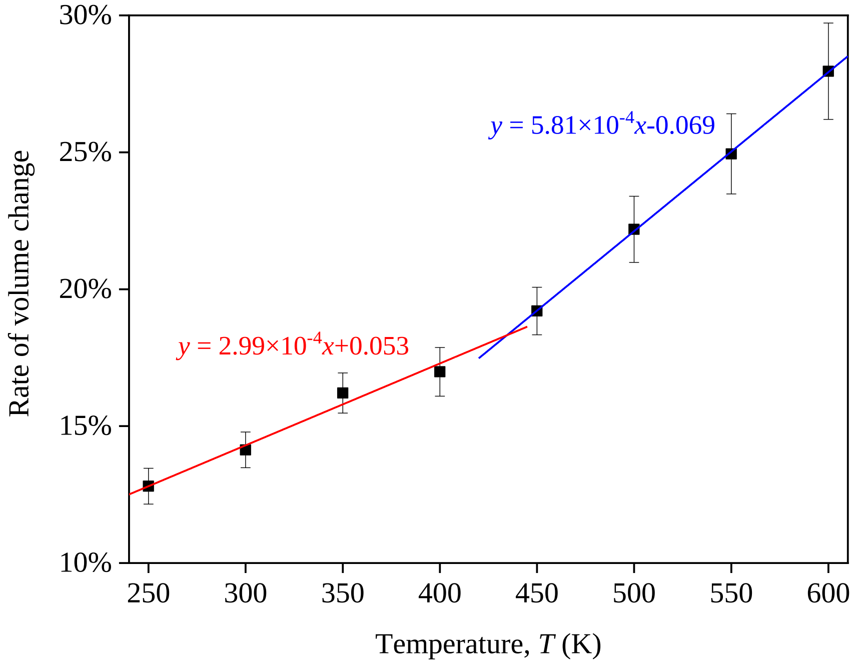

Figure 3-7 Volume of DGEBA/TETA epoxy system with the variation of temperature

Table 3-2 Material properties of MD simulation and experimental data for epoxy resin

Material properties	MD simulations					Experiment
	Present study	Ref. [102]	Ref. [106]	Ref. [107]	Ref. [108]	Ref. [109]
T_g (K)	434	440			383	436
ρ (g/cm^3)	1.14	1.13	1.175			1.131
α_1 (ppm/K)	299		272.16	310.8	166	
β_1 (ppm/K)	99.6		90.72	103.6	55.3	
α_2 (ppm/K)	581				554	
β_2 (ppm/K)	193				184.7	

3.3 Kaolinite-epoxy system

Figure 3-8 illustrates a schematic view of the kaolinite-epoxy system created by combining the kaolinite model (Figure 3-2(b)) and the cross-linked epoxy resin model (Figure 3-5). The simulation box of the system measures 61.8 Å × 35.8 Å × 70 Å and contains a total of 6064 atoms. Firstly, the interfacial accommodation between kaolinite and epoxy resin will be studied in this simulation box in Section 3.1.

Secondly, in order to study the effect of normal stress and sliding velocity on friction behavior between kaolinite and epoxy resin, the atomic force microscope experiment is considered by SMD to simulate the (001) kaolinite model sliding over an (001) surface of the epoxy model in Sections 3.2&3.3. A series of normal stresses of 0.5 to 5 GPa are applied in the rigid layer of kaolinite with a fixed sliding velocity of 50 m/s to study effects of normal stress, and also a set of sliding velocities of 5 to 800 m/s are applied with a fixed normal stress of 1 GPa to study velocity effects. To avoid structural failure, a normal stress of up to 5 GPa is chosen, which is well below the ultimate compressive strength of kaolinite, reported to be 14.4 GPa [110]. Given the absence of published work on the choice of interaction force and shear velocity at the atomic scale in pile-soil systems, the values used in this study are based on similar values reported in other nanofriction simulations, ranging from 0.5 to 5 GPa for normal stress and 5 to 800 m/s for sliding velocity [111-113]. It is important to note that the forces and velocities applied at the nanoscale are several orders of magnitude larger than those at the macro scale, mainly due to the fact that the actual contact area of surfaces prone to friction is almost $1/10^5$ of the visible area of contact [114].

The kaolinite-epoxy system (Figure 3-8) is divided into four parts from top to bottom: (1) a rigid kaolinite layer (2 Å) that is subjected to normal stress and pulling force with no structural deformation; (2) a free layer of kaolinite (~13 Å) and an equally thick free layer of epoxy for simulating friction; (3) a fixed epoxy layer (6 Å) to ensure that the whole system does not move around. The simulation of the kaolinite-epoxy system is conducted under NVE ensemble. A temperature-controlled layer of kaolinite (~4.5 Å) is employed to maintain the system at 300 K. NVT ensemble is used for the temperature-controlled layer. This analogous configuration for friction simulation has been previously reported by Hu et al. [111, 112] and Wei et al. [115].

To address the boundary effect in the model, periodic boundary conditions are applied to both the *x* and *y* directions. The thickness of the free layer is also ensured to be larger than the cutoff distance in the model to minimize the impact of the rigid and fixed layers on the contact surface between the epoxy and kaolinite. Additionally, a sufficient vacuum layer is established in the *z*-direction to prevent any interaction between the kaolinite and epoxy on the opposing side.

The normal stress is applied on each atom of the rigid layer of kaolinite with the thick of 2 Å, and there is no structural deformation. A pulling force is also applied on the kaolinite rigid layer to provide a constant sliding velocity along the *x*-direction.

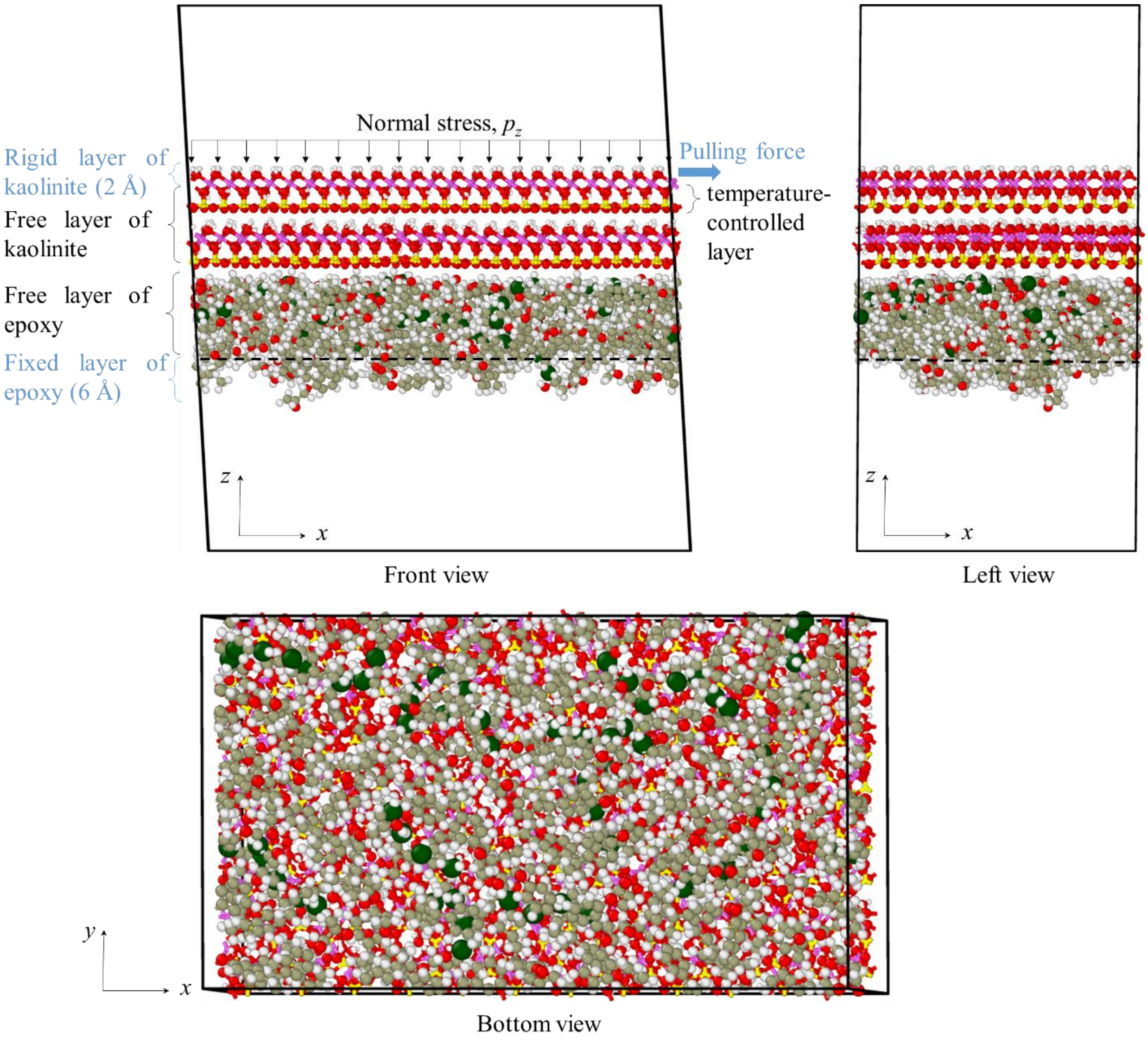

Figure 3-8 The kaolinite-epoxy system in the simulation box

3.4 Results and discussions

3.4.1 The interfacial accommodation between kaolinite and epoxy resin

Surface roughness can lead to atom interlocking, wherein the epoxy infiltrates into the six-membered silicate rings of the kaolinite surface, potentially affecting the equilibrated configuration and total energy of the system. To address this issue, a series of simulations with different initial interfacial distances are conducted to identify the optimal initial distance for achieving the minimum total energy of the kaolinite-epoxy system and eliminating possible atom interlocking effects during equilibration. This methodology has been previously utilized in related study [116]. These simulations are respectively equilibrated for 1 ns with a timestep of 1.0 fs in the NVT ensemble. The epoxy resin is adsorbed on the siloxane surface of kaolinite during the equilibration. The total energy versus interfacial distance curve is presented in Figure 3-9. It can be seen that the minimum total energy of the kaolinite-epoxy system is found at the interfacial surface distance of 2.9 Å. Thus, the optimal interfacial distance of 2.9 Å is chosen to obtain the most stable combined system, which will also be employed to study the friction behavior between kaolinite and epoxy resin in Sections 3.2&3.3.

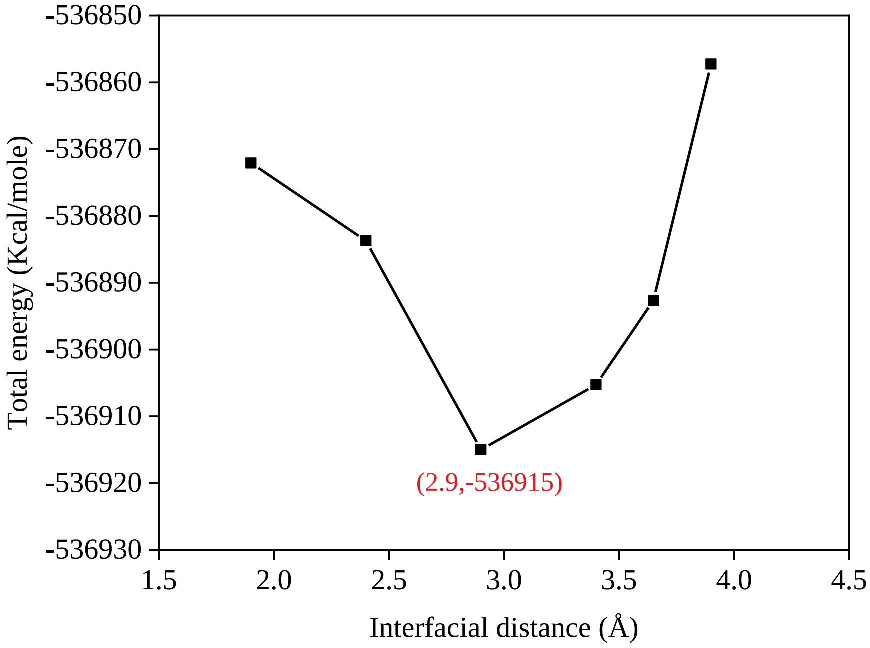

Figure 3-9 Variation of total energy of kaolinite-epoxy system with interfacial distance

Work of adhesion, the energy needed per unit area to separate an interface into two free surfaces, is a fundamental interfacial quantity for an interface [117]. Work of adhesion between epoxy and kaolinite is used to evaluate and predict the mechanical properties of the interface and calculated by:

$$W = \frac{E_{\text{kaolinite}} + E_{\text{epoxy}} - E_{\text{kaolinite+epoxy}}}{2A} \tag{3.7}$$

where A is the area of the contact surface; $E_{\text{kaolinite+epoxy}}$ is the total energy of the epoxy-kaolinite system; and, $E_{\text{kaolinite}}$ and E_{epoxy} are the total energy of kaolinite and epoxy systems, respectively. As shown in Figure 3-10, calculations have been done in the NVT ensemble with a temperature of 300 K and an equilibration length of 1 ns in the kaolinite, epoxy, and kaolinite-epoxy systems, respectively. The total energy of all three systems is calculated by the average values after 0.1 ns in the equilibrium state, and the calculated work of adhesion between epoxy and kaolinite obtained by Eq. 3.7 is 159 mJ/m^2. To our knowledge, experimental values for the work of adhesion between epoxy and kaolinite have not been reported. The work of adhesion values investigated by a series of experiments for epoxy-montmorillonite [118], epoxy-silica [119], and MXene-epoxy [120] interfaces are found to be 98.6, 178, and 123.6 mJ/m^2, respectively, which are similar to or lower than the calculated work of adhesion between kaolinite and epoxy in this study.

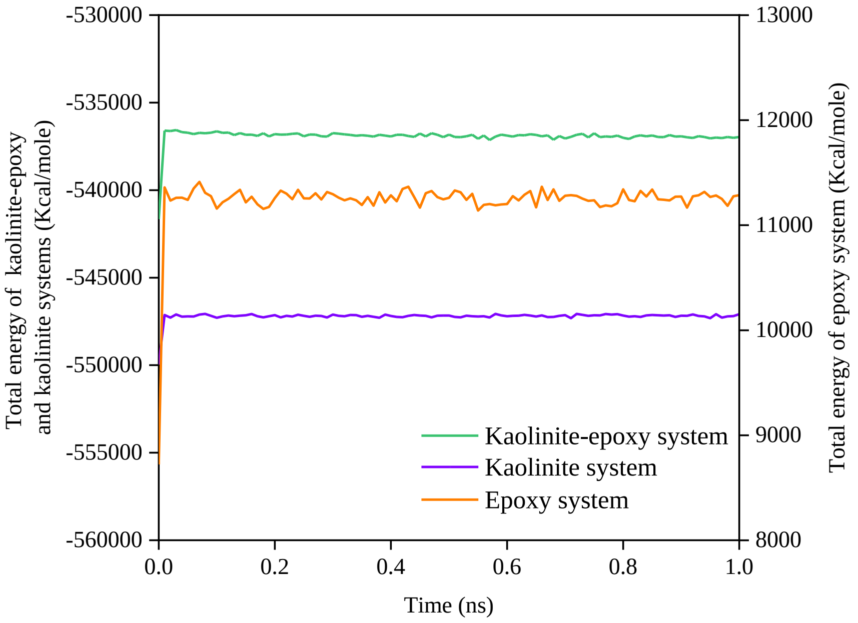

Figure 3-10 Variation of total energies of three systems with simulation time

The bonding information of the interface is characterized by the radial distribution function *g*(*r*), which is the probability of finding a given particle at a distance from a reference particle. Figure 3-11 compares the radial distribution function of the oxygen atom ($O_{kaolinite}$) in kaolinite interaction surface with other atom types in the epoxy model, such as nitrogen atom (N_{epoxy}), oxygen atom (O_{epoxy}), carbon atom (C_{epoxy}), and hydrogen atom (H_{epoxy}). $O_{kaolinite}$ represents the oxygen atom in the siloxane surface of kaolinite. The first peaks of all these atom pairs are larger than 2.5 Å, which means that the main interaction mechanism between epoxy and kaolinite is van der Waals interaction.

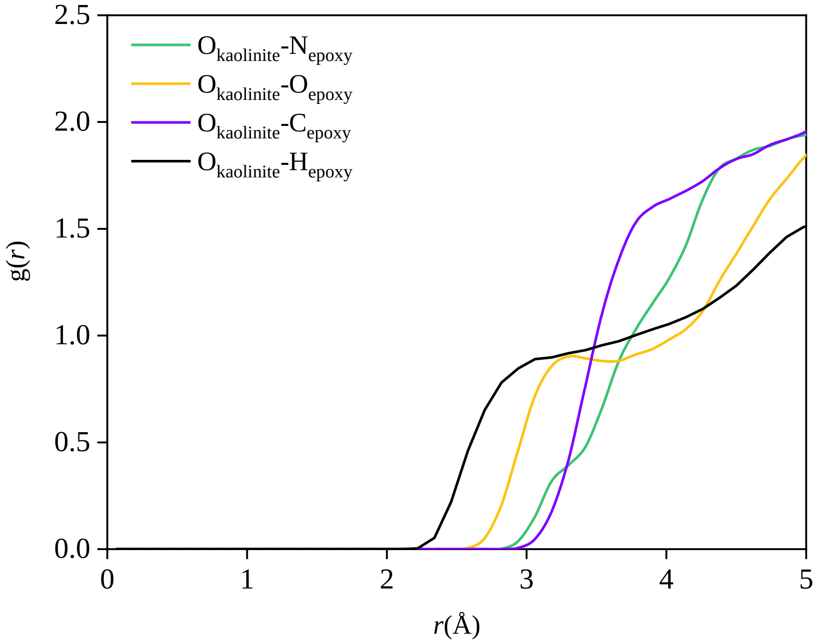

Figure 3-11 Radial distribution function curves of the kaolinite-epoxy system

3.4.2 Influence of normal stress on friction behavior

FRP piles are commonly subjected to lateral earth pressures from the surrounding soil [121, 122]. The friction behavior is affected by the soil pressure on the piles. Lateral earth pressure is therefore simulated by applying normal stress to the kaolinite in the kaolinite-epoxy system. The rigid layer of the kaolinite is subjected to a pulling force along the epoxy resin with the constant sliding velocity (v). The normal stresses (p_z) of 0.5 to 5 GPa are applied on the rigid layer of the kaolinite with a sliding velocity of 50 m/s during the SMD simulation.

Figure 3-12 shows the variation of friction force with the increase of sliding distance in the *x*-direction at different normal stresses. It can be seen that the normal stress during the sliding process has an essential effect on the surface friction behavior, and the friction force increases with the increment of the normal stress. On the other hand, the wave phenomenon of the friction force represents the stick-slip motion during the sliding process, which has been frequently observed for various contacting materials under different sliding conditions [115, 123-127].

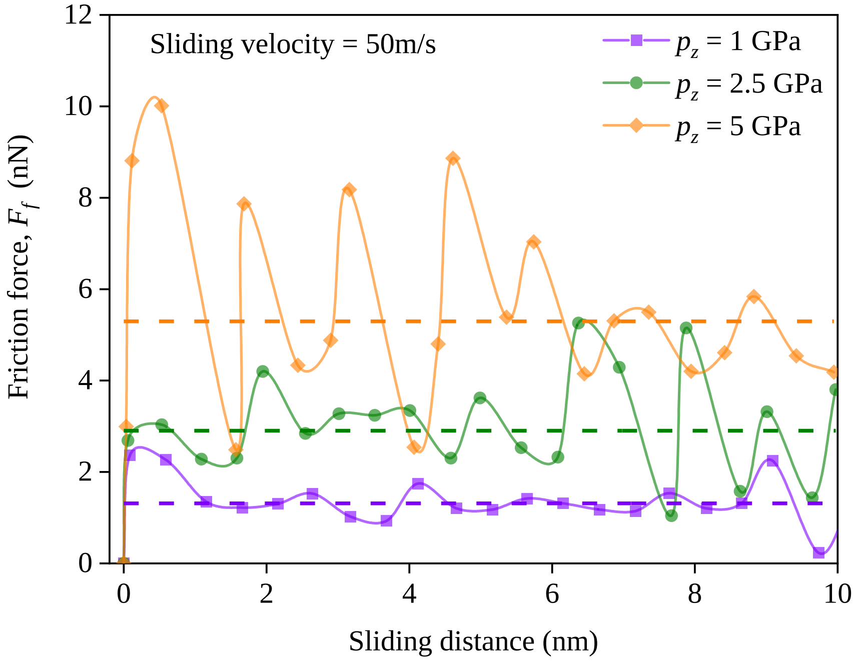

Figure 3-12 Friction force versus sliding distance curve under different normal stresses

The friction force versus normal force relation [113, 128] is given by:

$$\mu = \frac{F_f}{F_n} = \frac{\sum_i^N F_{fi}}{\sum_i^N F_{ni}} \tag{3.8}$$

where μ is the friction coefficient; F_f is the calculated friction force; F_n is the normal force; N is the number of kaolinite atoms; and, F_{ni} and F_{fi} are the interaction forces of atom i along the direction of x and z. The normal and friction forces at different normal stresses are plotted in Figure 3-13 to describe the friction behavior. It can be seen that the normal and friction forces rise linearly with the increasing normal stress. The peak interface friction coefficient is an important parameter to analyze the interface friction process, which is calculated by the formula [129]:

$$\mu_p = C_1 \ln\left(p_z\right) + C_2 \tag{3.9}$$

where C_1 and C_2 are the constants, and μ_p is the peak interface friction coefficient, which is obtained from the peak value of the coefficient of friction. Figure 3-14 shows that the peak interface shear coefficient decreases nonlinearly as the normal stress increases, which is consistent with the trend of the FRP-soil interface shear test results [129].

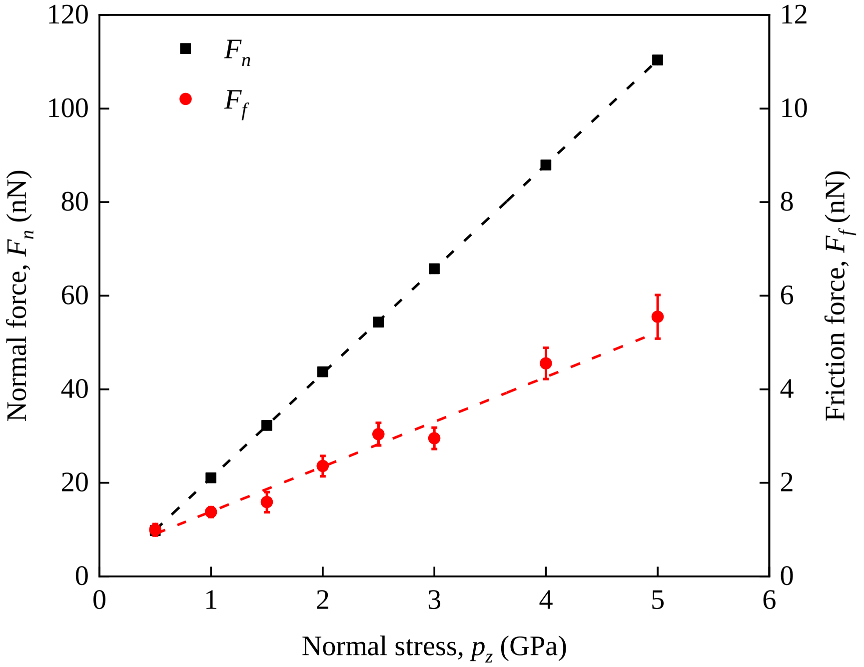

Figure 3-13 Variation of calculated friction and normal forces with applied normal force

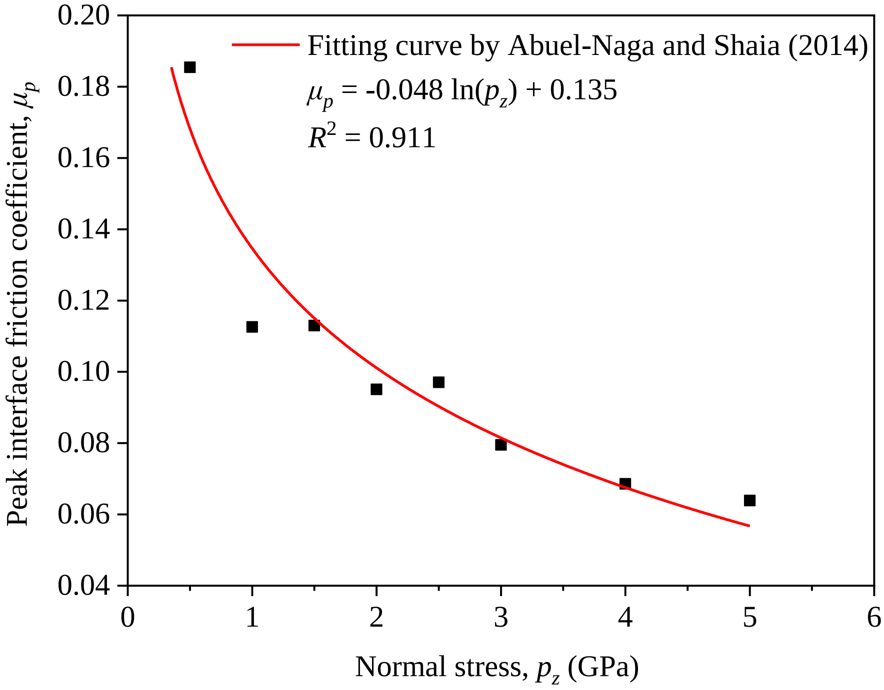

Figure 3-14 Variation of peak interface friction coefficient with normal stress

Hydrogen bonds would be formed by the oxygen atoms on the siloxane surface in the condensed phases [110]. The hydrogen atom in epoxy and the oxygen atom in kaolinite have the potential to form the hydrogen bonds. It can be seen in Figure 3-15 that obvious peaks of radial distribution function for $O_{kaolinite}$-O_{epoxy} and $O_{kaolinite}$-N_{epoxy} under different normal stresses are formed at around 3.0 Å. It indicates that oxygen and nitrogen atoms in the epoxy are closely attached to the siloxane surface of kaolinite. It is also observed that the values of the first peak of $O_{kaolinite}$-N_{epoxy} at the normal stress of 5 GPa are significantly larger than those at lower normal stress, which indicates more epoxy atoms near the kaolinite surface, thereby causing higher interaction energy. A cutoff distance of 3.5 Å with an angle cutoff of 30° has been used as the criterion for hydrogen bond formation by Pokhrel et al. [130]. The number of hydrogen bonds between kaolinite and epoxy under different normal stresses during the equilibration simulation is shown in Figure 3-16. The increasing normal stress increases with the number of hydrogen bonds and makes hydrogen bonds form faster, which may lead to a higher average friction force. It indicates that hydrogen bond plays an essential role in enhancing the friction force between kaolinite and epoxy.

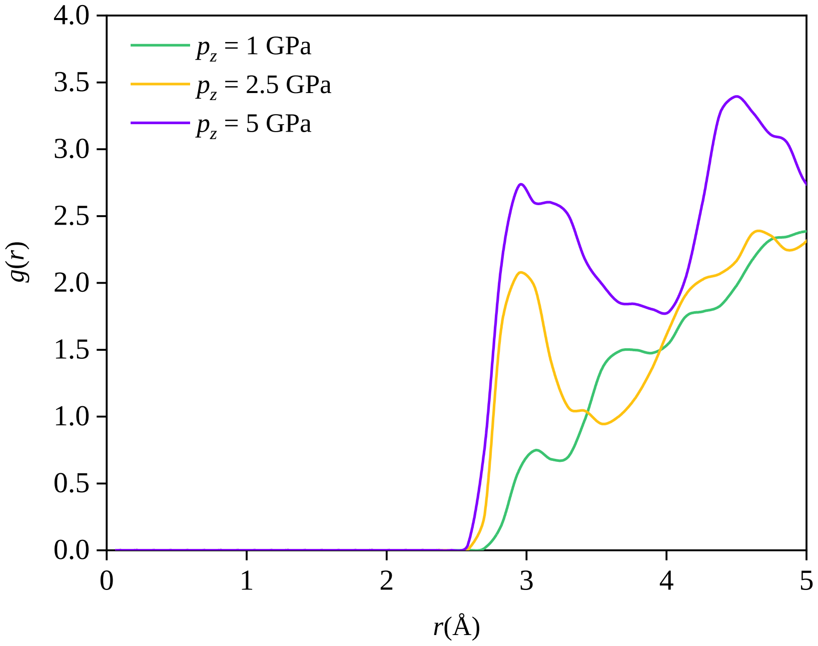

(a)

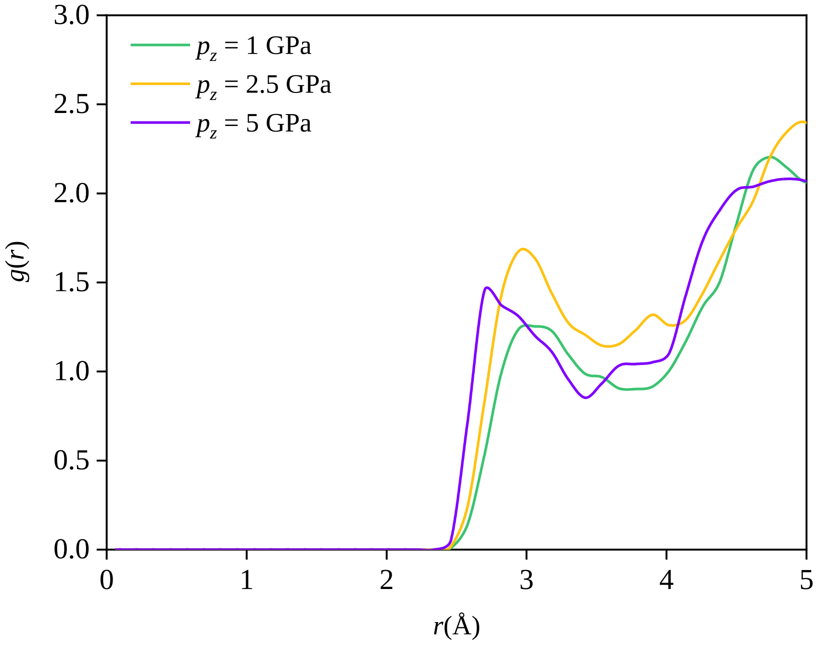

(b)

Figure 3-15 Radial distribution function curves under different normal stresses (a) $O_{kaolinite}$-N_{epoxy} (b) $O_{kaolinite}$-O_{epoxy}

The snapshot views of interface structure at the normal stresses of 1, 2.5, and 5 GPa are depicted in Figure 3-17. The distance between the top of kaolinite and the bottom of the free layer of epoxy (*d*) gradually decreases from 23.4 to 20.3 Å with increasing normal stress in three systems, indicating an increase in compression of the epoxy and kaolinite. The increased normal stress will increase the van der Waals forces between kaolinite and epoxy due to the shortening of the distance between the two layers.

The stick-slip phenomenon arises from potential barriers at the interface and has been reported to be influenced by surface roughness and the bonding formation [125, 126]. The approximate periodic force versus displacement curve in Figure 3-12 can be attributed to the lattice structure of kaolinite, where surface atoms are uniformly arranged. However, the surface of the epoxy resin has a certain "roughness", due to its non-homogeneous surface atoms. As the normal stress increases, atoms of the epoxy surface may experience dislocation, and the formation of interfacial hydrogen bonds becomes faster, resulting in larger energy barriers and a more distinct stick-slip behavior.

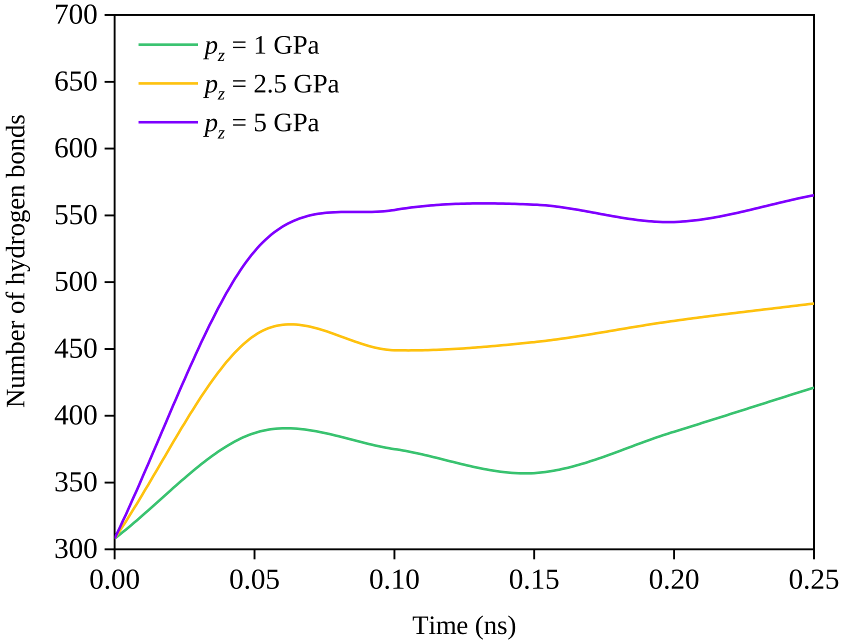

Figure 3-16 The variation of the number of the hydrogen bonds with simulation time under different normal stresses

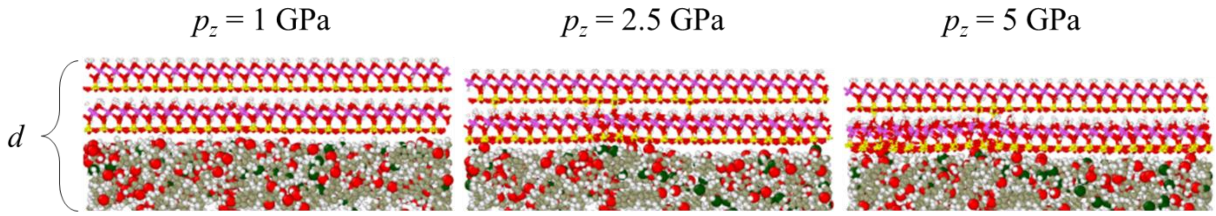

Figure 3-17 Snapshot views of the interface friction behavior after sliding 10 nm under different normal stresses

3.4.3 Influence of sliding velocity on friction behavior

The relationship between the friction load and the sliding velocity at the nanoscale is complex. This is because the atomic friction process involves complex surface effects such as the adhesion effect and surface contact mode. In order to explore the effect of sliding velocity on friction behavior, the relationships between the pulling force and sliding displacement with the sliding velocities of 5 to 800 m/s are studied and depicted in Figure 3-18. The normal stress applied in kaolinite is constant and fixed at 1 GPa. It can be seen that the higher the sliding velocity, the higher the average pulling force. On the other hand, stick-slip motion is found in slow sliding velocity (5 to 100 m/s) but not in fast sliding velocity (500 to 700 m/s). The response of interfacial bonding during friction is more adequate at slow sliding velocities, resulting in a noticeable stick-slip motion. However, at fast sliding velocities, interfacial atoms do not have sufficient time to respond, resulting in a smoother curve. The similar effect at slow and fast sliding velocities is also observed in the friction behavior between two montmorillonite portions [115].

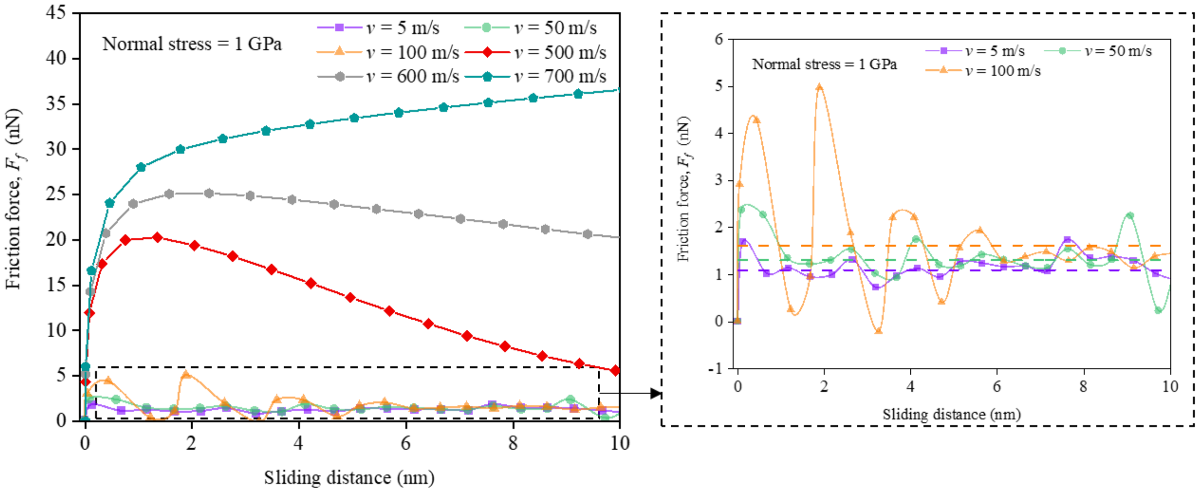

Figure 3-18 Friction force versus displacement curve under different sliding velocities

The transition from the static friction stage to the kinetic friction stage is a process in which the atoms move from a stable equilibrium state to a neighboring one [131]. The movement of an atom requires it to overcome an energy barrier (E_b) formed by the surrounding atoms. The extended Bell theory [77, 132] can be used to calculate the energy barrier, which is given by:

$$v = v_0 e^{\frac{F_f x_b}{k_b T}} \tag{3.10}$$

$$v_0 = \omega_0 x_b e^{-\frac{E_b}{k_b T}} \tag{3.11}$$

where k_b is the Boltzmann constant; T is the temperature; v_0 is the natural bond-breaking velocity; and, ω_0 is the natural vibration frequency. F_f can be obtained from Eqs. 3.10&3.11 and written by:

$$F_f = \left(\frac{Tk_b}{x_b}\right)\ln v - \frac{k_b T \ln v_0}{x_b} = a\ln v + b \tag{3.12}$$

where a and b are the constants.

The average friction force as a function of dimensionless ln(v/v^*) is recorded in Figure 3-19, where $v^* = 1$ m/s. It is observed that nanofriction between kaolinite and epoxy exhibits two distinct velocity regions: slow pulling mode (5 to 200 m/s) and fast pulling modes (400 to 800 m/s). Two regions follow a logarithmic relationship between the average friction force relative to the sliding velocity. Both modes can be well fitted by extended Bell theory.

The slow pulling mode allows the more detailed dynamic evolution of the system during the SMD simulation, leading to a more accurate calculated energy barrier [133]. In this regard, cases with normal stresses of 2.5 and 5 GPa are also studied in the slow pulling mode, as seen in Figure 3-19. The linear regression equation's parameters (a and b) are obtained from the relationship between the logarithmic velocity and the associated average friction force. The system's dynamic evolution can be more comprehensively observed in response to the applied pulling force in the slow pulling mode [133], which allows for a more precise calculation of the intrinsic energy barrier. The calculated energy barriers with the normal stresses of 1, 2.5, and 5 GPa are 5.695, 8.504, and 8.976 Kcal/mole-Å in the slow pulling mode, respectively. This increasing tendency of the energy barrier with increasing normal stress is consistent with the experimental phenomenon that higher pulling forces are required for the FRP to slide along the soil at higher normal stress [129]. It can also be found that the sliding velocity for distinguishing between the slow and fast pulling modes is 384 m/s.

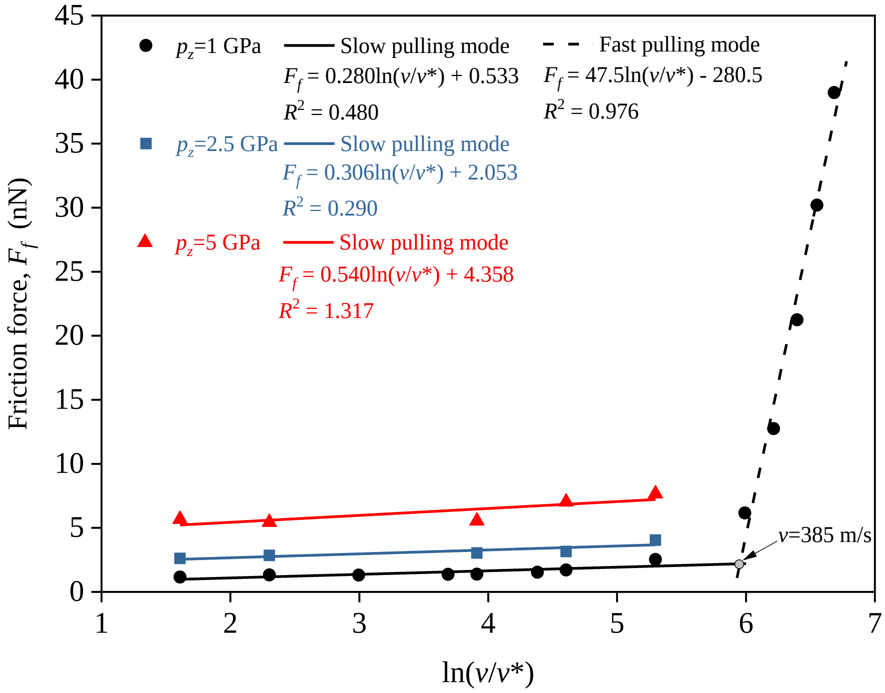

Figure 3-19 Friction force as a function of sliding velocity variation for slow and fast pulling mode ranging from 5 to 200 m/s and from 300 to 800 m/s respectively

3.5 Conclusions

This study investigates the friction behaviors between the FRP pile (epoxy) and clay (kaolinite) from an atomic scale using the MD simulation. Research in this area is essential for providing intrinsic information to bridge micro- to macro-scale structure-soil mechanical behaviors. The main conclusions are drawn below：

(1) The siloxane surface is chosen as the contact surface with epoxy resin in this work due to its smaller surface energy (74.3 mJ/m^2) compared with hydroxylated surface (195.1 mJ/m^2). A cross-linked epoxy resin is constructed with a surface well-fit-kaolinite. Thermal properties and density of the epoxy resin have good agreement with previous results of MD simulations and experiments.

(2) The work of adhesion between epoxy and kaolinite is calculated as 159 mJ/m^2. The main interaction mechanism between epoxy and kaolinite is van der Waals interaction.

(3) The peak interface shear coefficient decreases nonlinearly as the normal stress increases and follows a logarithmic relationship, which is similar to the trend of the FRP-soil interface shear test results. The increased normal stress will increase the van der Waals forces between kaolinite and epoxy due to the shortening of the interface distance and the compression between epoxy and kaolinite.

(4) Nanofriction between kaolinite and epoxy also depends on shear velocity. The higher sliding velocity leads to a higher average pulling force. Two distinct velocity regions, slow pulling mode (5 to 200 m/s) and fast pulling modes (300 to 800 m/s), are observed, and both regions can be well fitted by extended Bell theory. The stick-slip motion is only found in slow sliding velocity.

(5) The calculated energy barriers with the normal stresses of 1, 2.5, and 5 GPa are 5.695, 8.504, and 8.976 Kcal/mole-Å, respectively. This increasing tendency of the energy barrier explains why higher pulling forces are required for the FRP to slide along the soil at higher normal stress.

Chapter 4. Molecular dynamics simulations of the interface friction behavior between fiber-reinforced polymer pile and sand

Abstract

The interfacial friction performance of the fiber-reinforced polymer (FRP) pile-sand interface plays an essential role in determining the load capacity of the foundation. It is necessary to identify its friction behavior in the marine environment due to the unique pile-soil interaction characteristics, which have not been well established at the nanoscale. The cross-linked epoxy resin and crystalline silica substrate are utilized to investigate the nanoscale friction characteristics with different normal stresses and sliding velocities in the dry, pure water, salt water systems using the molecular dynamics (MD) simulation. The coefficients of friction in the three systems are ranked as dry > salt water > pure water systems. The water molecules located between the epoxy and silica act as a lubricant to make the friction amplitude smaller, while the NaCl ions weaken the lubrication effect. An extra interaction force between the epoxy and the silica substrate can be induced by the water molecules in the *z*-direction and can be reduced by the NaCl ions. On the other hand, the lubrication effect of the water molecules weakens as the sliding velocity increases during the initial sliding stage. The increase in normal stress shortens the distance between the silica and the epoxy and increases the van der Waals force between the two layers, resulting in the increase of maximum friction force in the three systems.

Keywords: FRP pile; Sand; Friction behavior; Coefficient of friction; Molecular Dynamics

4.1 Introduction

Different pile types (e.g., timber, concrete, and steel piles) have been used in engineering to support marine structures such as wind turbines, sea bridges, and artificial islands [134-136]. The corrosion is a huge risk to the service life of conventional pile types. It will lead to high maintenance costs when used in a harsh marine environment. The fiber-reinforced polymer (FRP) pile brings sustainability advantages to marine structures and thus experiences particular interest. FRP is a new type of corrosion-resistant material fabricated in the form of a polymer matrix reinforced with fibers. Usually, the polymer is epoxy, vinyl ester, or polyester, and fibers are made of glass, carbon, and aramid [137]. The FRP pile has the potential to replace conventional pile types due to its non-corrosive nature, lightweight, and superior mechanical properties [13, 20, 138].

The axial load transfer mechanism of the FRP pile is essential in analyzing and designing substructures [21]. The interfacial friction between FRP and soil plays an important role in determining the load capacity of the foundation [22, 23], which has a significant effect on the settlement of the foundation. In comparison with structural steel or concrete, FRP materials have significantly lower stiffness and surface hardness, which results in unique pile-soil interaction characteristics for the FRP piles [6]. Due to the fact that friction behaviors of the FRP-sand interface may be quite different from the conventional cases, special attention needs to be paid to settlement problems during the construction of the FRP pile. Therefore, the study of interface friction behavior between the FRP pile and sand is important to improve the application of FRP piles in marine structures.

Earlier investigations on the interface friction behavior between FRP pile and sand have focused on the macroscale mechanical tests. Frost and Han [68] reported that the interface surface roughness and the applied normal stress would affect the interface shearing behavior of the FRP pile and sand. Pando et al. [69] found that the interface friction angles of FRP composite piles depended on the values of relative roughness parameters. The molecular dynamics (MD) method has been widely used in civil engineering to predict mechanical responses and characterize material properties [48-52]. The silica is a dominant component of the sand fraction [139]. Employing the MD simulation, sand surfaces have been investigated by silica models to understand various interface phenomena [140-143]. The friction interface of epoxy/silica (the subsystem of FRP pile and sand interface) has not been well established at the nanoscale. Extensive efforts have been focused on the material properties and mechanical responses of the FRP-concrete bonding system through the epoxy-silica interface. Büyüköztürk et al. [77] studied a layered material system consisting of a single chain of epoxy and silica substrate with under moisture effect. Lau et al. [144] combined the experiment and MD simulation to study the effect of moisture on the bonding between epoxy and silica. Yaphary et al. [133] studied the effect of NaCl solution on the adhesion of epoxy-silica interface. Jian et al. [78] investigated the interfacial creep behavior in epoxy-bonded bilayer material systems consisting of SU-8 monomer and silica substrate. The above MD studies focus on epoxy-silica bonding behaviors by considering epoxy as a single polymer chain. However, such a single chain of epoxy with a limit size may not provide a clear understanding of the friction behaviors when focusing on the interactions between FRP pile and sands.

In this study, MD simulations are carried out to study the interface friction behavior between FRP and sands through an understanding of interactions between the cross-linked epoxy resin and silica substrate. The dry, pure water, salt water systems are developed because the friction behavior of FRP pile in the marine environment may be influenced by water and NaCl ions. The silica substrate is subjected to an external force along the epoxy in the steered molecular dynamics (SMD) simulation. Normal stress and sliding velocity, the two most critical mechanical parameters controlling friction behavior, will be taken into account to study their effects on the epoxy-silica interface. The findings in this study reflect the effect of environmental conditions, normal stresses, and sliding velocities on the friction behavior at the FRP-sand interface. This comprehensive study can further explore the applications of FRP pile in the marine environment.

4.2 Simulation method and model

This atomic simulation focuses on the interface friction behaviors between the cross-linked epoxy resin and crystalline silica substrate in dry, pure water, salt water systems. The initial model starts from constructing a silica-epoxy interfacial model built by software Materials Studio. The atomistic MD simulations are implemented by using LAMMPS software [87]. The Open Visualization Tool software [145] is applied for the visualization. The Consistent Valence Forcefield (CVFF) is used to determine the atomic interaction of epoxy and silica. The CVFF has been validated and parameterized in various experiments and simulations for water, ions, epoxy, and silica [78, 102, 146, 147]. The model construction processes and simulation approach are described in the following section.

4.2.1 Construction of the silica model

The lattice parameters of crystalline silica [148] used in this work are a = 4.913 Å, b = 4.913 Å and c = 5.405 Å with $\alpha = \beta = 90°$ and $\gamma = 120°$. This unit cell contains three Si and six O atoms. The entire silica substrate is constructed from a unit cell of crystalline silica by repeating the unit cell in the x-, y- and z-directions. In order to represent the non-periodic boundary condition of the silica substrate in the z-direction, the created open bonds in this direction are terminated by hydrogen atoms. A bulk silica substrate (1760 atoms) with the size of a = 49.1 Å, b = 34.0 Å, c = 12.8 Å, and $\alpha = \beta = \gamma = 90°$ is shown in Figure 4-1.

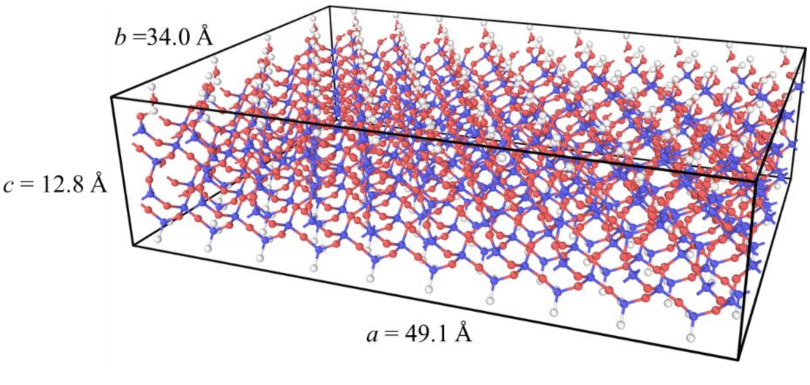

Figure 4-1 Model of silica substrate (Si, blue; O, red; H, white)

4.2.2 Models of cross-linked epoxy resin

The cross-linked epoxy resin is composed of diglycidyl ether of bisphenol A (DGEBA) and triethylenetetramine (TETA) (Figure 4-2). As shown in Figure 4-3, the reactive CH site is created by breaking the C-O bond in the epoxide group of DGEBA. The reactive site for nitrogen in TETA is achieved by removing hydrogens. Energy minimization is performed, and then the system is equilibrated for 0.1 ns in an NVE ensemble to relax the system. In the cross-linking process, the covalent bonds are created between C and N atoms in reactive sites under a certain distance in the mixture of DGEBA and TETA. The reactive distance is set at 5 Å in this work. The system is relaxed by another circle for 0.1 ns in the NVE ensemble to remove the unfavorable interactions due to the creation of new C-N bonds. Cross-linking simulation is repeated until the conversion rate of the model reaches the required value. In the end, the reactive C and N atoms without bonding in this system need to be saturated with hydrogen atoms.

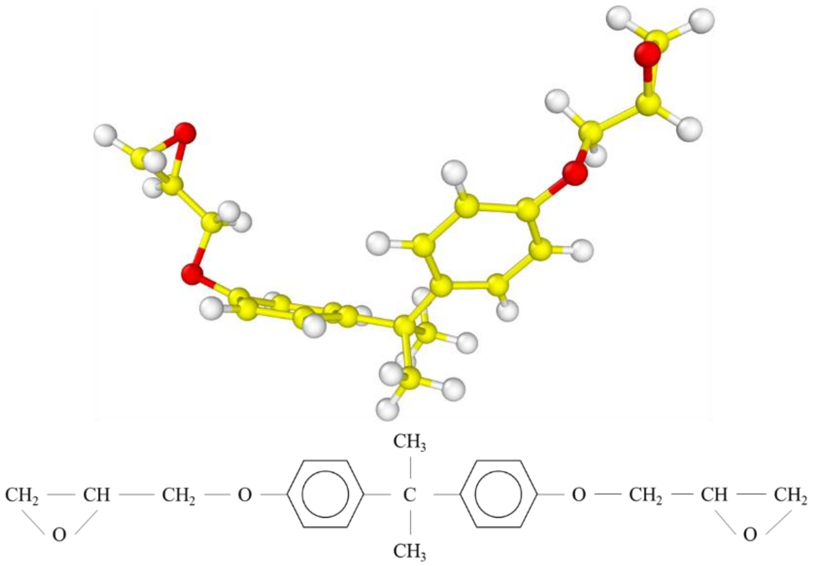

(a) DGEBA

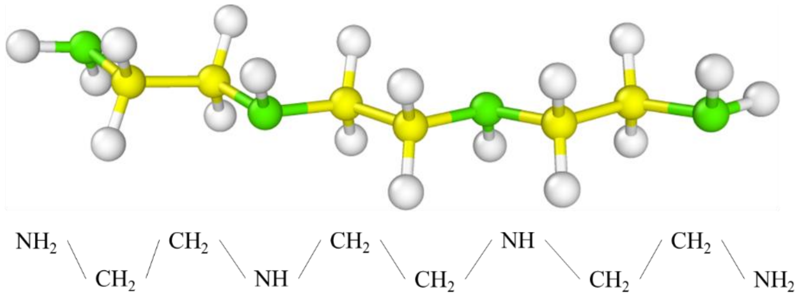

(b) TETA

Figure 4-2 Chemical structures of DGEBA and TETA (C, Yellow; N, green; O, red; H, white)

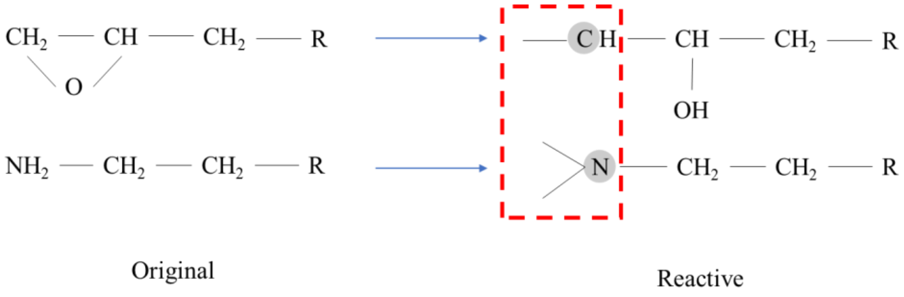

Figure 4-3 Conversion of functional groups used in the cross-linked procedure

The ideal composition ratio for DGEBA/TETA in the cross-linked epoxy resin is 6:2 [100]. 54 molecules of DGEBA and 18 molecules of TETA are constructed. As shown in Figure 4-4, the cross-linked epoxy model contains 2829 atoms with the size of 49.1 Å × 34.0 Å × 35.0 Å. The final conversion from DGEBA and TETA into the final epoxy model is 88.9%, which is a reasonable conversion ratio that could occur naturally in the experiment [101, 104]. The Voigt-Reuss-Hill model [149] is employed to calculate the mechanical properties of the cross-linked epoxy. As shown in Table 4-1**,** the calculated results of the Young's, shear, and bulk moduli, Poisson's ratio, and density in this study are compared with other simulation and experimental results, which are in good agreement.

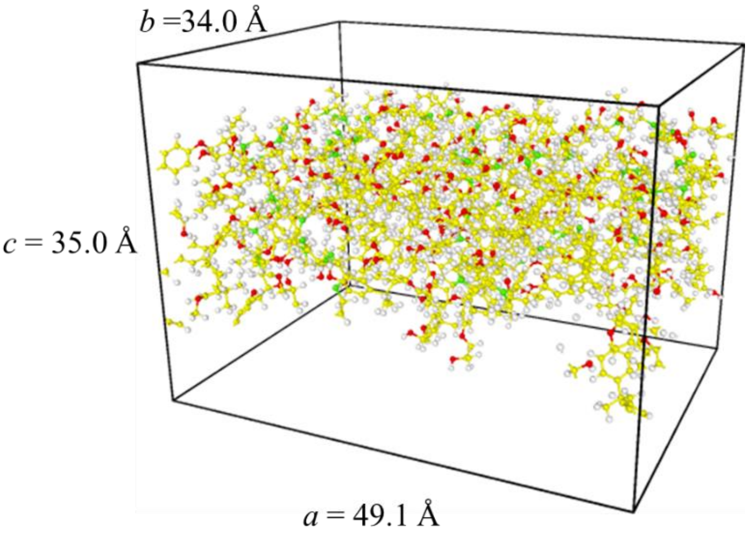

Figure 4-4 Final model of cross-linked epoxy resin

Table 4-1 Mechanical properties of the epoxy resin

Mechanical properties	MD simulations			Experimental values [150, 151]
	This study	Jeyranpour et al., 2015 [105]	Yu et al., 2009 [150]	
Young's modulus (GPa)	3.518	2.73	3.548	3.24
Bulk modulus (GPa)	1.536	1.42	/	/
Shear modulus (GPa)	1.573	1.06	1.296	/
Poisson's ratio	0.118	0.18	/	/
Density (g/cm^3)	1.1010	1.1084	/	1.1240

4.3 Construction of silica-epoxy interfacial models in three systems

The simulation boxes for the three systems are presented in Figure 4-5. A sufficient vacuum layer is set in the z-direction to avoid the interaction between silica substrate and epoxy resin on the other side. The size of the simulation box of the three systems is 49.1 Å × 34.0 Å × 55.6 Å, 49.1 Å × 34.0 Å × 64.0 Å, and 49.1 Å × 34.0 Å × 64.0 Å, respectively.

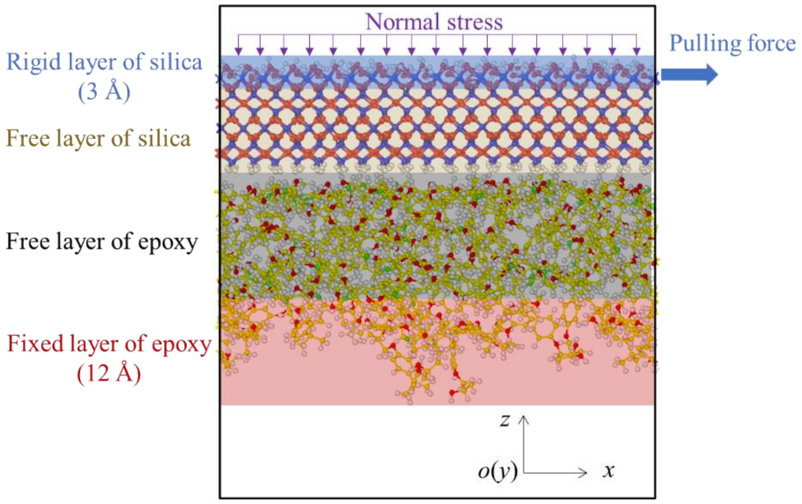

(a) Dry system

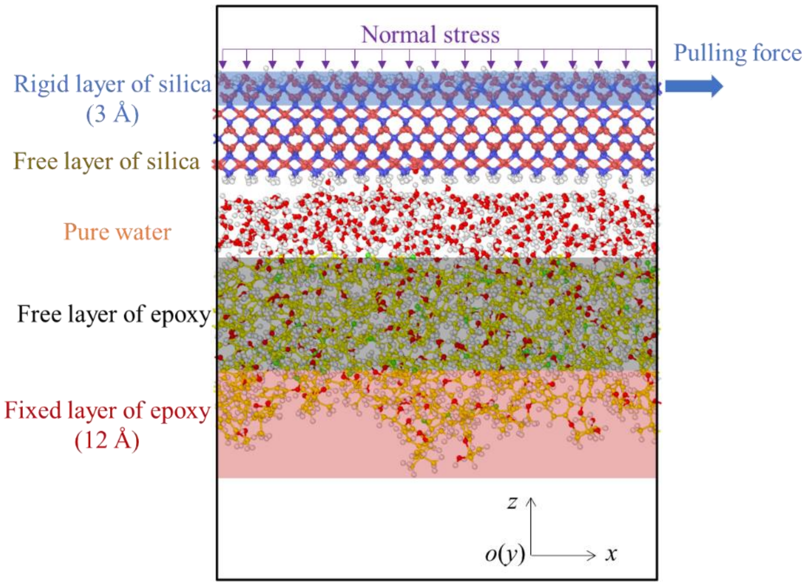

(b) Pure water system

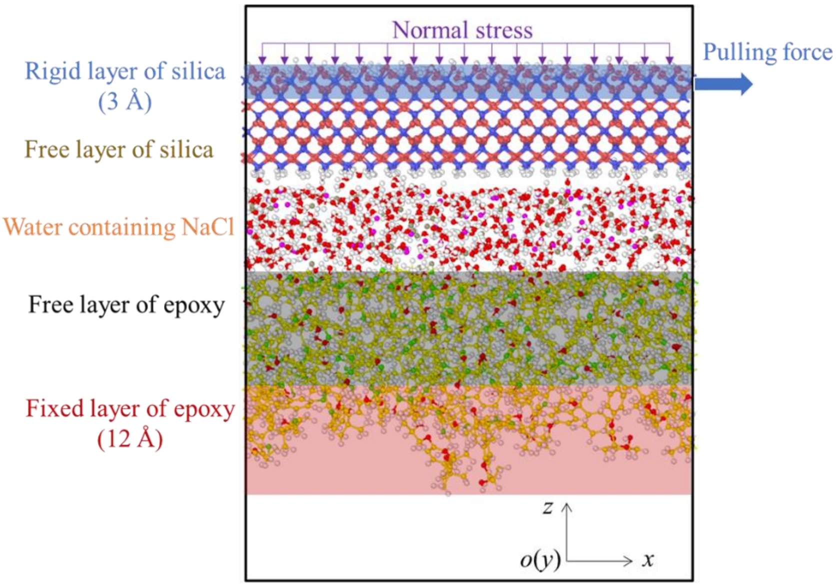

(c) Salt water system

Figure 4-5 The contact model of epoxy and silica in different systems

The SPC model is used to describe the water molecules. The amount of H_2O in the simulation box of both pure water and salt water systems is 446 molecules. The moisture content of soil ($M_{\mathrm{water}}/M_{\mathrm{silica}}$) is 29.1%, which is within the range of the moisture content of saturated sand [152]. There are 72 Na^+ ions and 72 Cl^- ions in the saturated salt water system. Figure 4-6 shows the variation of density for the pure water model and saturated salt water model. Two models are equilibrated under NPT ensemble with 300 K and 1 atm. The obtained density for the pure water and the salt water are 1.024 g/cm^3 and 1.207 g/cm^3, respectively. The experimental results for the densities of pure water and saturated salt water is 0.996 g/cm^3 and 1.200 g/cm^3, respectively [153]. It can be seen that the simulation in this study produces nearly identical results of density with experiment.

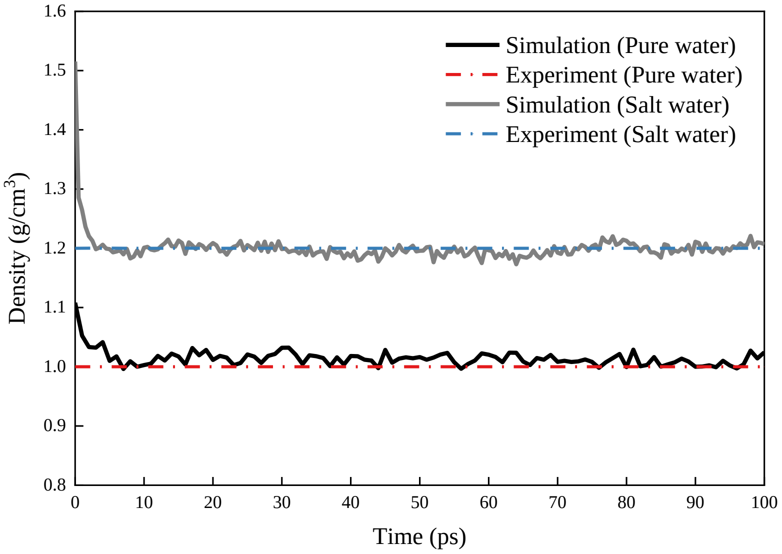

Figure 4-6 The variation of density during the equilibrium

4.4 Simulation procedures

All calculations are performed in the simulation box with periodic boundaries in the *x*-, *y*-, and *z*- directions. The van der Waals interaction is calculated with a cutoff distance of 10 Å. The particle-particle particle-mesh (PPPM) algorithm with a tolerance of 10^{-4} is applied to calculate long-range electrostatics. The timestep value is set to 1.0 fs, and the Nosé-Hoover thermostat [92] is employed to control the temperature through the whole simulation. During the SMD simulation, the lower part of epoxy is fixed so that it does not wander away. The simulation process in three systems is shown in Figure 4-7. Initially, the silica substrate, epoxy, water, and salt water models are combined for different systems. Then, a 100 ps equilibrium for three systems is performed under the NVT ensemble at 300 K. SMD is employed to simulate the interface friction process. As shown in Figure 4-5(a), the rigid layer of silica substrate is subjected to a pulling force in the *x*- direction with the constant sliding velocity (v). The normal stress (p_z) is applied on the rigid layer of silica substrate during the NVT equilibration and SMD simulation.

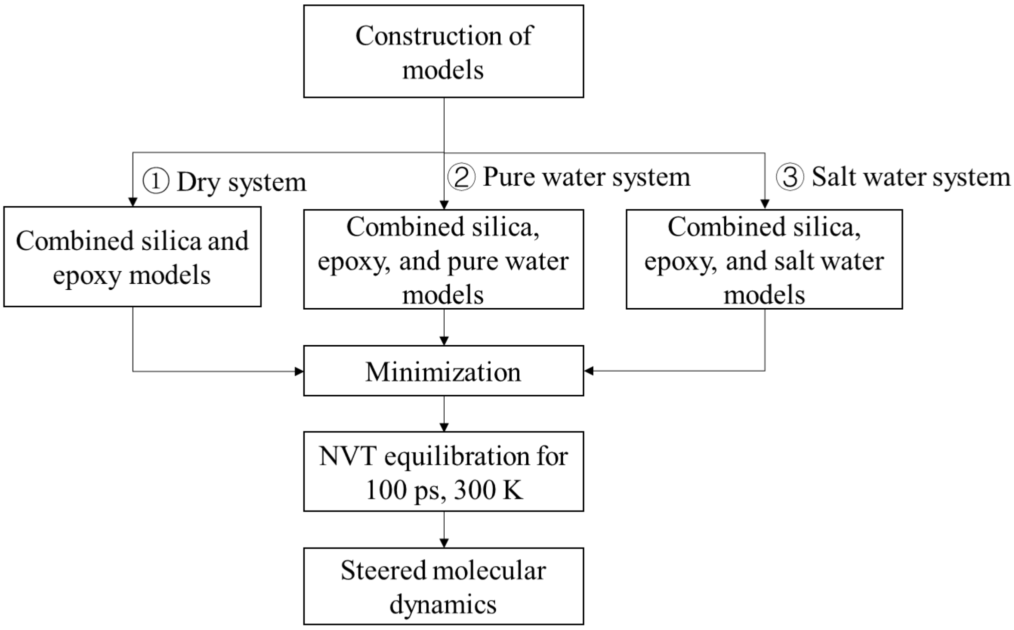

Figure 4-7 Molecular dynamics simulation process for three different systems.

4.5 Results and discussions

The forces on the silica atoms in the *x*- and *z*-directions are defined as friction force (F_x) and normal force (F_z), respectively. The friction performance in the surface can be expressed by the coefficient of friction (μ), which is given by

$$\mu = \frac{F_x}{F_z} = \frac{\sum_i^N F_{xi}}{\sum_i^N F_{zi}} \tag{4.1}$$

where N is the number of silica atoms; F_{xi} and F_{zi} are the interaction forces of atom i along the direction of x and z, respectively. In order to study the effect of normal stress on the friction behavior in different systems, normal stresses of 200, 400, 600, 800, and 1000 MPa are applied in the rigid layer of silica with a high sliding velocity of 100 m/s. The high sliding velocities have been employed to study friction mechanism in MD simulations by many researchers [115, 123, 154, 155]. It has been found that the high sliding velocities used in MD simulations can closely simulate the sliding state of materials in the vicinity of the sliding interface in the experiment, especially during the initial sliding stage [154]. The friction force, normal force, and the coefficient of friction are calculated by averaging the output value every 1ps during the sliding process in simulations. Figure 4-8 shows the variation of friction force at different normal stresses in the dry, pure water, and salt water systems. In order to deal with noisy data, the smooth curves of the friction force are obtained by the mean values of the original data. The friction force can be divided into the nonlinear zone during the initial sliding stage and the steady-state zone during the stable sliding stage. It increases more rapidly when higher normal stresses are applied during the initial sliding stage in three systems. Then, in the dry system, the friction force will decrease before it reaches the stable sliding stage (Figure 4-8(a)). In the pure water and salt water systems, the friction force continues to increase nonlinearly with the sliding displacement until it converges after the displacement is about 3.5 nm (Figure 4-8(b)&(c)). The interaction between silica and epoxy persists during the stable sliding stage, and the original curves of friction force fluctuate around a relatively fixed value. It can also be seen that the maximum friction force increases with the increment of the normal stress in the three systems. Hence, the normal stress during the sliding process has an essential effect on the surface friction behavior between silica and epoxy.

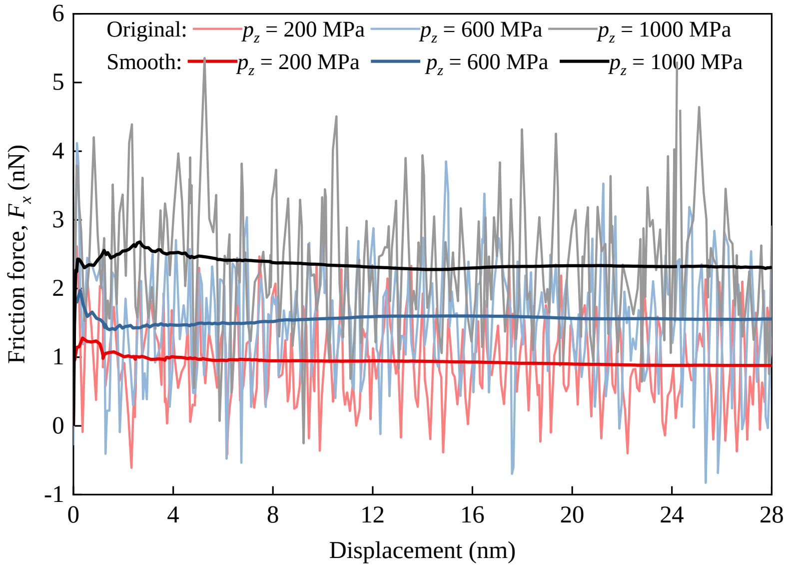

(a) Dry system

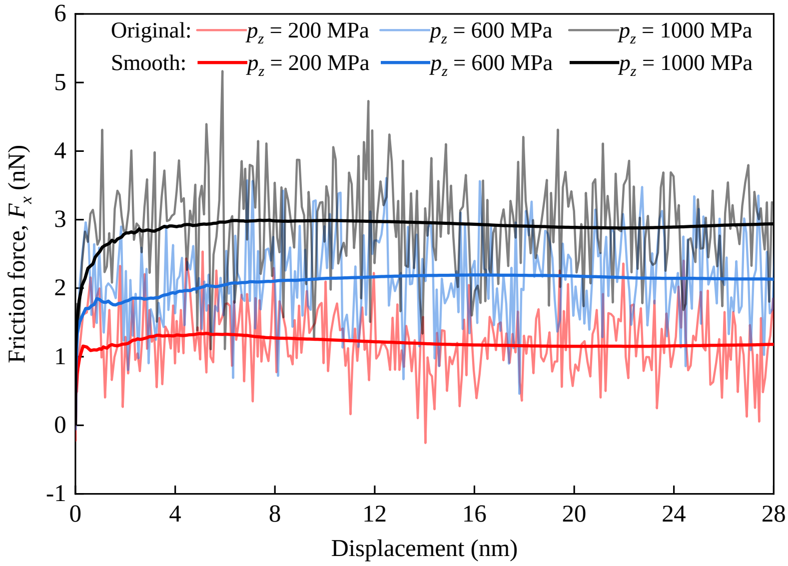

(b) Pure water system

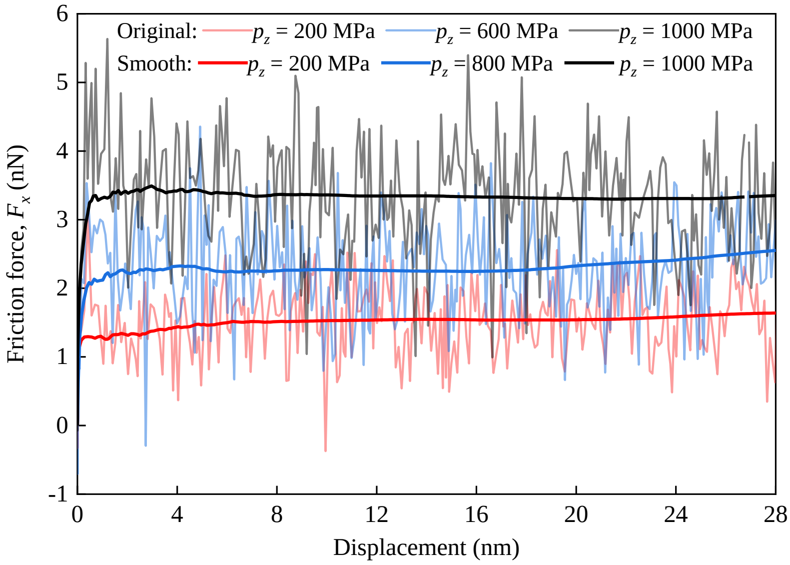

(c) Salt water system

Figure 4-8 Friction force versus displacement curve under different normal stress

To gain insight into the influence of normal stress on the friction behavior, the evolutions of interface structure at the normal stresses of 200, 600, and 1000 MPa in the three systems are depicted in Figure 4-9. There is direct contact between the epoxy molecules and the silica in the dry system, whereas water molecules and NaCl ions occupy the gaps between epoxy and silica in the salt water system. The distance between the rigid layer of silica and the fixed layer of epoxy gradually decreases with increasing normal stress in three systems, indicating an increase in compression of the epoxy, silica, and water. The increased normal stress will increase the van der Waals forces between silica and epoxy due to the shortening of the distance between two layers. This leads to an increase in the maximum friction force with increasing normal stress.

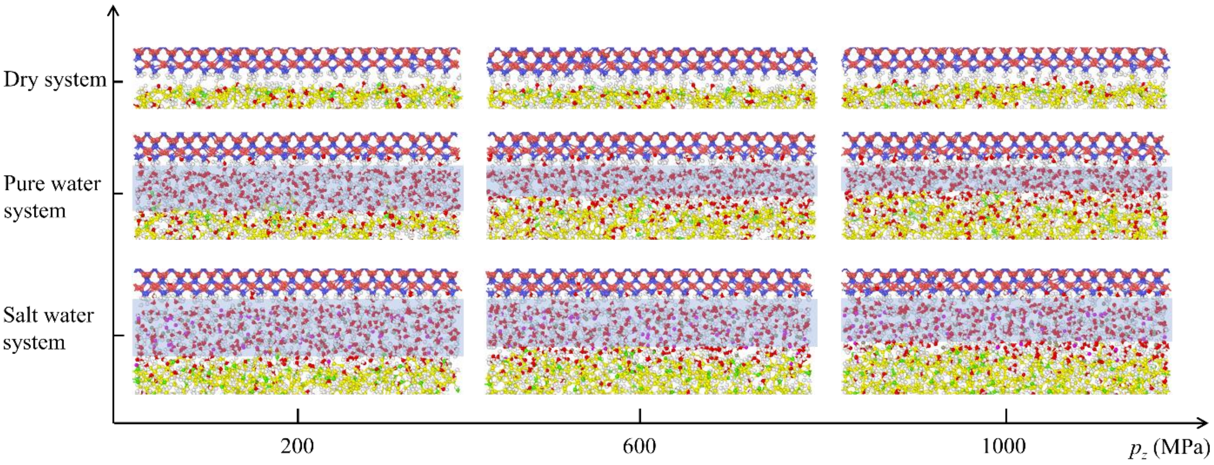

Figure 4-9 Snapshot views of the interface friction behavior after sliding for 100ps.

The tendency of the friction oscillation curve during the sliding process has a correlation with energy dissipation [156]. The silica substrate accumulates the potential energy in its original position before it moves. A sudden slip of silica substrate occurs when the potential energy is released, and the silica substrate will move forward in a non-uniform step. The diffusions of water molecules will be caused by the sliding of silica substrate, which is beneficial for the hydrodynamic lubrication at the contact interface [157]. In order to indicate the effect of the normal stress and water environment on friction oscillation, the amplitude of the friction force is presented in Figure 4-10 by using the friction force in Figure 4-8. It can be seen that the amplitude of friction force in the pure water system is smaller than that in the dry system. It indicates that the water molecules located between the epoxy and silica perform the role of lubricant to minimize the amplitude of the friction force in the pure water system. For the salt water system, water molecules have little effect on the amplitude of the friction force compared with the dry system. It indicates that the NaCl ions affect the lubricating properties of the water molecules, especially when the normal stress is high. On the other hand, the amplitude of friction force in the pure water system increases with increasing normal stress. In order to explain this phenomenon, mean-squared displacement (MSD) and self-diffusion coefficient (*D*) of the pure water along the *z*-direction in different normal stresses is shown in Figure 4-11 to study the diffusions of water molecules, which are calculated by

$$MSD(t) = \frac{1}{n}\sum_{j=1}^{n}\left|r_j(t) - r_j(0)\right| \tag{4.2}$$

$$D = \frac{MSD(t)}{6t} \tag{4.3}$$

in which $r_j(t)$ is the position of atom j in the z-direction at time t; n is the number of atoms for the pure water model. The diffusions of water molecules are induced by the sliding of silica substrate. The change of relative position in the z-direction for the water molecules on the contact interface promotes hydrodynamic lubrication [123]. The higher MSD and self-diffusion coefficient are observed at lower normal stress. This indicates that the lubricating effect of water molecules is more pronounced at lower normal stress because the distribution of water molecules becomes scattered in the contact surface.

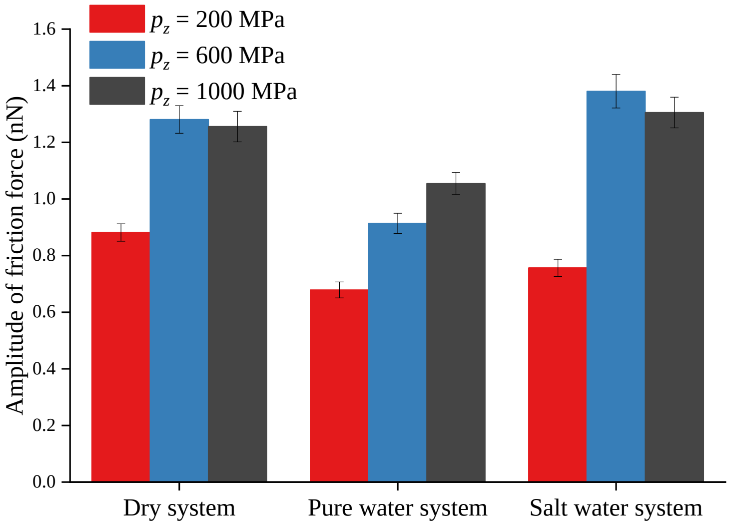

Figure 4-10 The average amplitude of friction force in three systems under different normal stresses

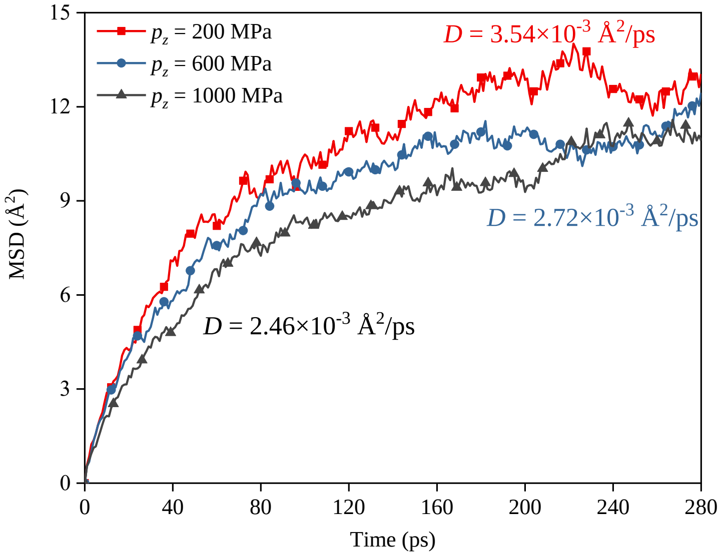

Figure 4-11 Mean-squared displacement of the pure water along the *z*-direction under different normal stresses.

In order to further describe the friction behavior, the average coefficient of friction, normal force, and friction force calculated from Figure 4-8 at different normal stresses are shown in Figure 4-12. It can be seen that the normal force rises linearly with the increasing normal stress in the three systems. The highest and lowest values of the coefficient of friction are obtained for the dry and pure water systems, respectively. The difference in the average friction force is small in three systems at the same normal stress with high sliding velocity (v = 100 m/s). The values of coefficient of friction for salt water system are found between the highest and lowest values. The coefficient of friction has shown the trend of reduction in the three systems, which is consistent with the trend in the experimental results of Frost and Han [68]. On the other hand, the calculated normal force is highest in the pure water system with the same applied normal stress, followed by the salt water system, and lowest in the dry system. This indicates that water molecules induce an extra interaction force between the epoxy and the silica substrate in the *z*-direction, while the NaCl ions reduce this interaction force.

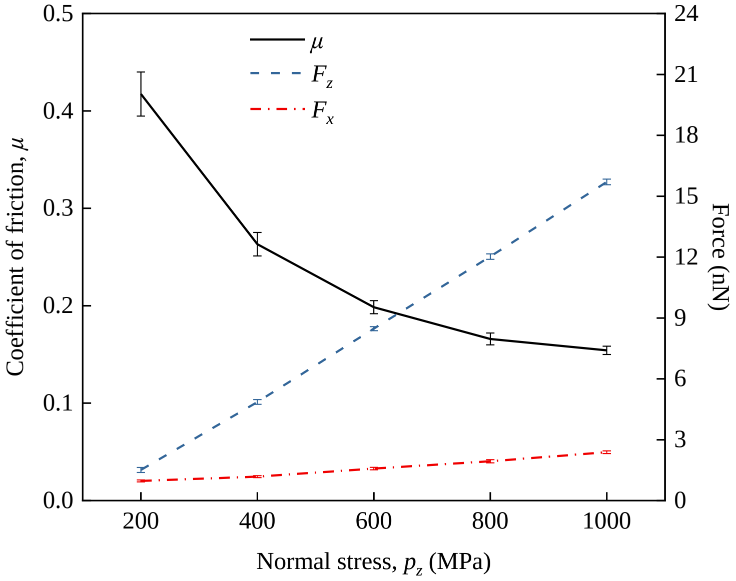

(a) Dry system

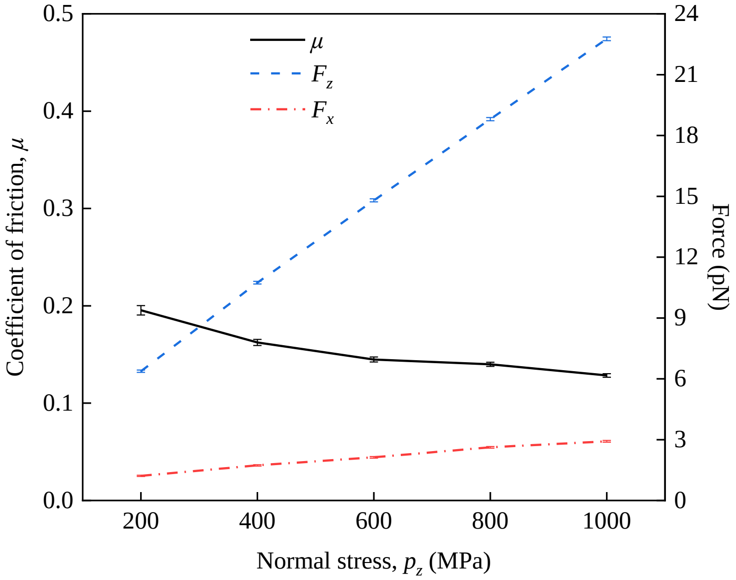

(b) Pure water system

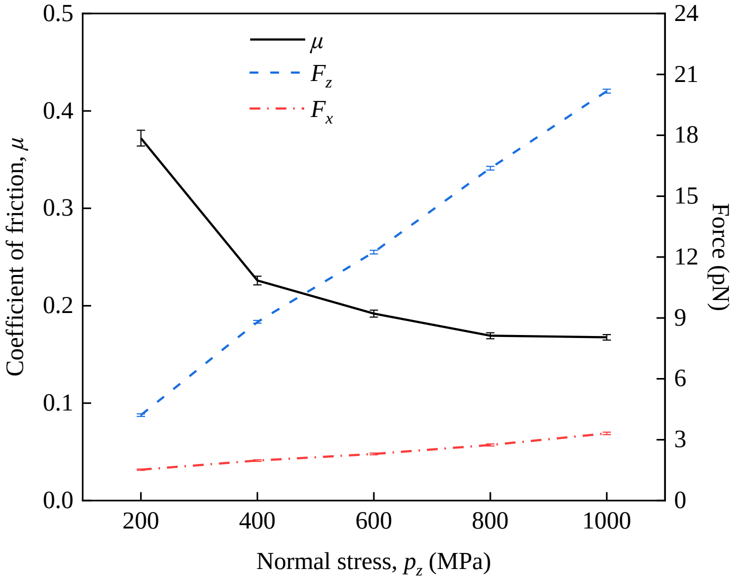

(c) Salt water system

Figure 4-12 The variation of the average coefficient of friction, friction force, and normal force under different normal stresses

The tangential stiffness, the typical output from the shearing tests, is defined as the tangent to the force-displacement curve [158, 159]. Figure 4-13 shows the tangential stiffness-displacement curves calculated by the slope of two data points on the force-displacement curve. The tangential stiffness drops gradually until reaching the steady-state zone where the tangential stiffness equals zero, which is consistent with the trend of the experimental results in reference [158, 160]. The tangential stiffness curves with lower normal stress reduce to zero more quickly. The part of the tangential stiffness curve that is less than zero in the dry system indicates that the friction force is decreasing with increasing sliding displacement. On the other hand, the initial tangential stiffness in dry systems is higher than that of pure water and salt water systems.

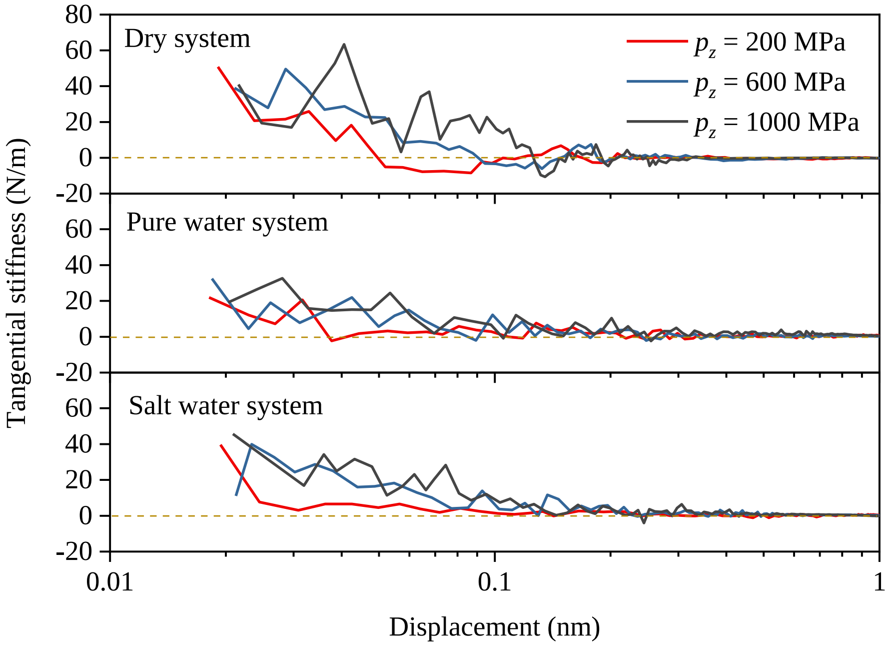

Figure 4-13 Tangential stiffness versus sliding displacement under different normal stresses

The roughness of FRP-sand surface can be described by the relationship between the peak interface friction coefficient and the normal stress, which has been studies by Frost and Han [68] with experiment. The peak interface friction coefficient is plotted against the normal stress in Figure 4-14. It can be seen that the peak interface friction coefficient tends to decrease with an increase of the normal stress. According to Archard's theory [161], the relationship between peak interface friction coefficient and normal stress is given by

$$\mu_p = C_1 {p_z}^{C_2} \tag{4.4}$$

where μ_p is the peak interface friction coefficient; and, C_1 and C_2 are the constants. The constant C_2 ranged from -0.33 to 0 indicates the change from a perfectly smooth surface to an extremely rough surface [161]. The constant C_2 describes the roughness of the interface materials and can be obtained by fitting Eq.4.4. In the case of a relatively rough interface surface, the constant C_2 is higher. On the contrary, a lower constant C_2 with a relatively smooth interface surface is obtained. The modeling results of constants C_2 in this study fall within this range from -0.33 to 0. The highest constant C_2 is found in a dry environment, which is larger than that in pure water and salt water systems. The constant C_2 denotes the threshold for maintaining the interfacial stability, and a higher friction force is required to achieve the sliding of silica substrate in the dry system than pure water and salt water systems.

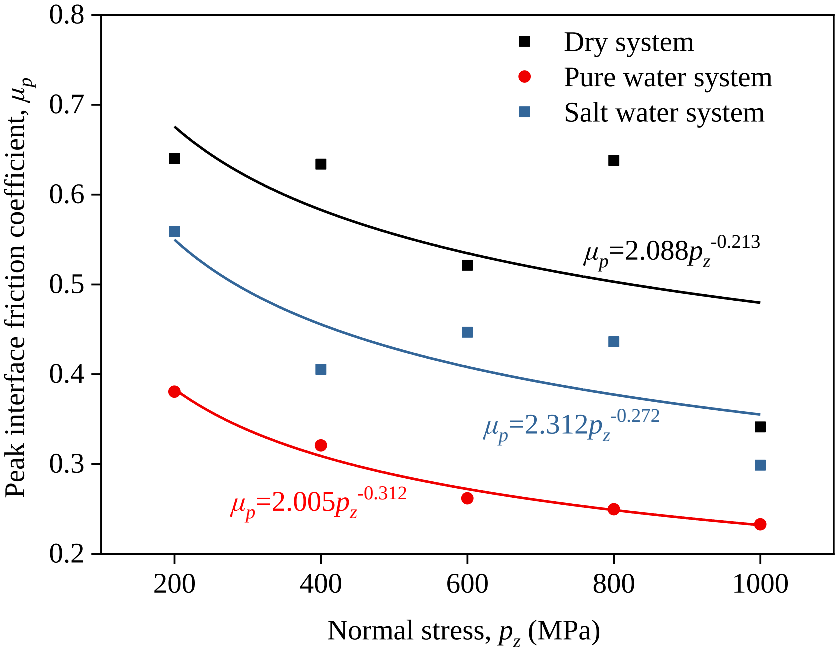

Figure 4-14 Peak interface friction coefficient versus normal stress

The relationships between the friction force and sliding displacement for three systems with the sliding velocities of 1, 10, and 100 m/s are depicted in Figure 4-15. The normal stress of 600 MPa is applied in the rigid layer of silica. In order to better investigate the friction behavior during the initial sliding stage, the friction force within a sliding distance of 3.5 nm is selected for this study. During the initial sliding stage, when the accumulated pulling force is higher than the van der Waals force between the silica and the epoxy and reaches the peak, the silica substrate has a maximum stretching. As the movement continues, the silica substrate tends to recover its shape and retract until the pulling force is equal to the van der Waals force between the two layers. Then, the sliding stage of silica substrate has entered the next stage called the steady-state zone. There will be a sharp peak in the friction force versus displacement curve. It can be seen from Figure 4-15 that the friction force increases more quickly in the three systems when a higher sliding velocity is imposed. In the dry system, there is a sharp peak in the smooth curve of friction force versus displacement at a velocity of 100 m/s, whereas this does not occur at lower velocities. The increasing sliding velocity can change the sliding state in the pure water and salt water systems, where the increase in maximum friction force is more pronounced than in the dry system.

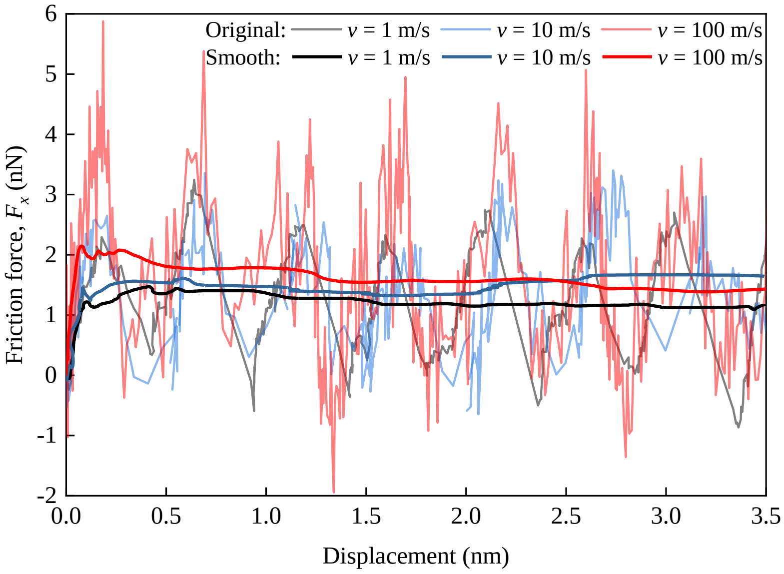

(a) Dry system

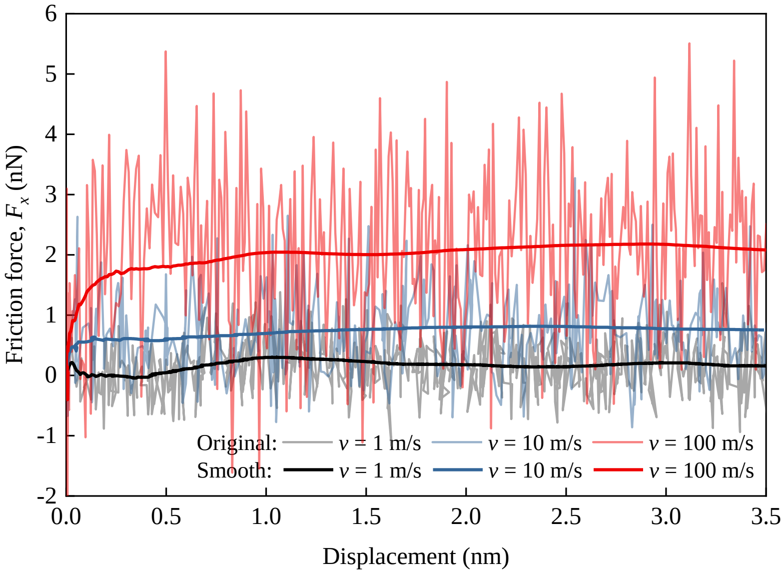

(b) Pure water system

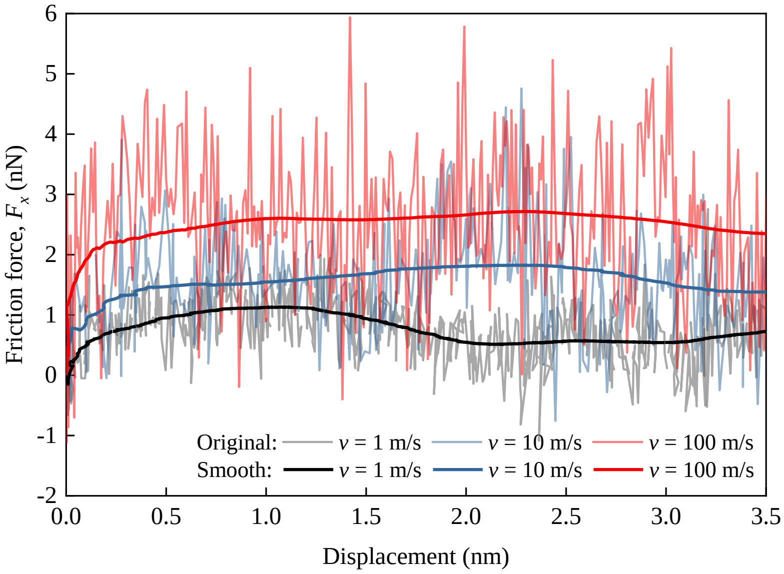

(c) Salt water system

Figure 4-15 Friction force versus displacement under different sliding velocities

The average amplitude of friction force in three systems under different sliding velocities is shown in Figure 4-16, which is obtained from the friction force in Figure 4-15. The results show that an increase in sliding velocity increases the amplitude of the friction force during the initial sliding stage in three systems. The water molecules located between the epoxy and silica play a very small role as a lubricant at a velocity of 100 m/s during the initial sliding stage. The lubricant effect becomes gradually apparent as the sliding velocity is reduced. The MSD and self-diffusion coefficient of the pure water along the *z*-direction in Figure 4-17 decreases with the increase of sliding velocity. It indicates that the diffusions of water molecules are fierce with lower sliding velocity, which has more beneficial for the hydrodynamic lubrication at the contact interface.

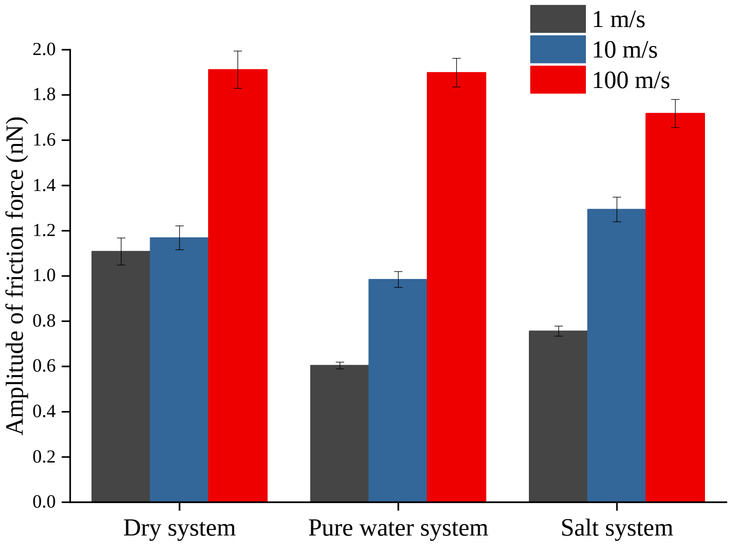

Figure 4-16 The average amplitude of friction force in three systems under different sliding velocities

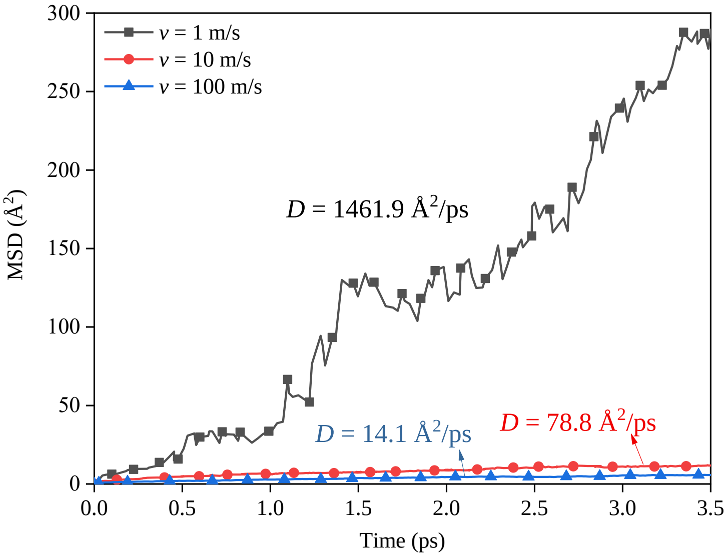

Figure 4-17 Mean-squared displacement of the pure water along the *z*-direction under different sliding velocities

The coefficient of friction, normal force, and friction force at different normal stresses are shown in Figure 4-18. These results indicate that the coefficient of friction and friction force increase with the increase in sliding velocity. The change in the sliding velocity can influence the friction properties of the silica-epoxy surface. The normal force is almost constant with sliding velocity in the pure water system, which indicates that the sliding velocity has little effect on the extra interaction force between the epoxy and the silica substrate induced by water molecules. The average friction force in the dry system is significantly higher than that in the pure water system at the same normal stress with low sliding velocity (1 m/s ≤ v ≤ 10 m/s), and this difference is small with high sliding velocity (v = 100 m/s). The coefficient of friction in the dry system is higher than that in the pure water and salt water systems under the sliding velocities of 1, 10, and 100 m/s during the initial sliding stage.

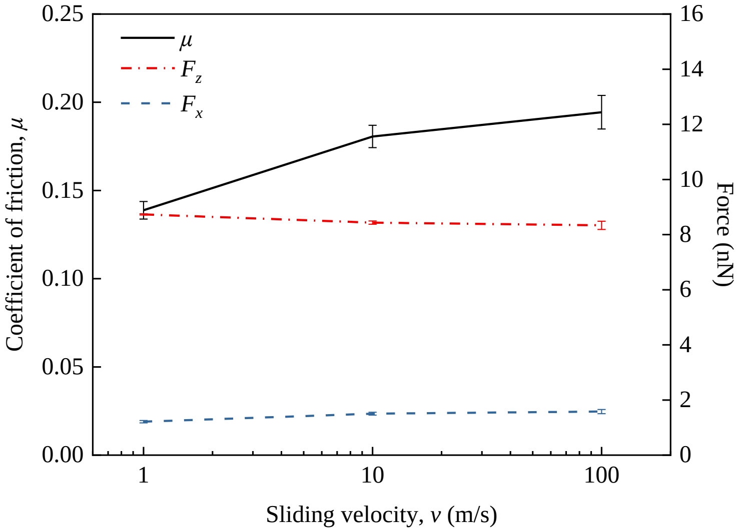

(a) Dry system

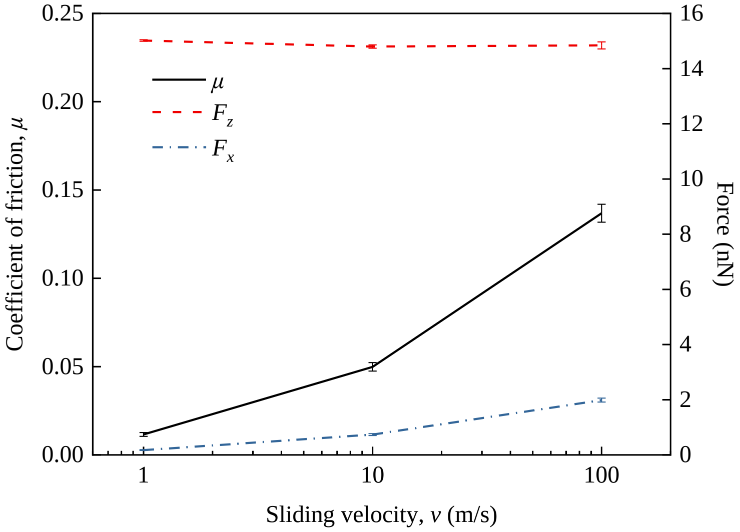

(b) Pure water system

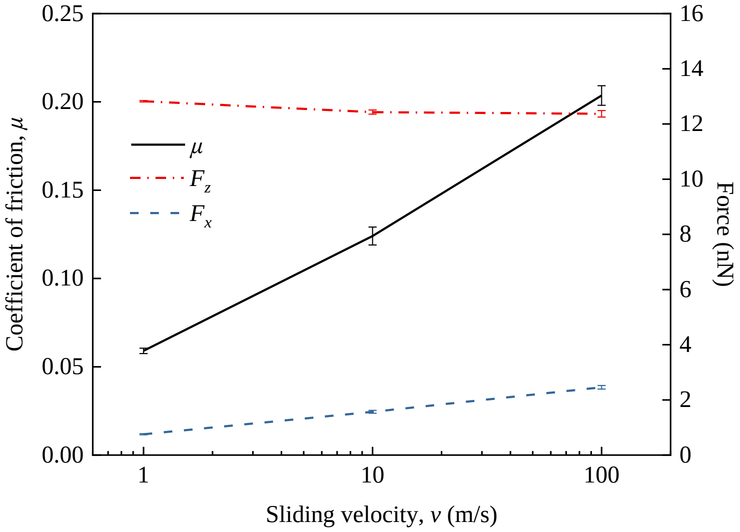

(c) Salt water system

Figure 4-18 The variation of the coefficient of friction, friction force, and normal force under different sliding velocities

4.6 Conclusions

MD simulation is conducted in this work to study the interfacial friction performance of the FRP pile-sand interface with different environments, normal stresses, and sliding velocities. The molecular models of cross-linked epoxy resin and crystalline silica substrate interface are constructed at room temperature in the dry, pure water, and salt water systems. The following conclusions can be drawn:

(1) The friction force-displacement curves can be divided into the nonlinear zone during the initial sliding stage and the steady-state zone during the stable sliding stage. The friction force increases nonlinearly with displacement during the initial sliding stage, and the tangential stiffness gradually decreases to zero to reach the steady-state. The tangential stiffness curves with lower normal stress (200 MPa) reduce more quickly to zero. The initial tangential stiffness in dry systems is higher than that in the pure water and salt water systems.

(2) The maximum friction force increases with the higher normal stress in three systems

because the shortening of the distance between silica and epoxy increases the van der Waals forces between two layers. The nonlinear characteristic of the friction force is closely related to the diffusions of water molecules and the NaCl ions effect during the initial sliding stage. The water molecules act as a lubricant in the friction oscillation, which makes the friction amplitude smaller, while the ion reduces the lubrication effect. The distribution of water molecules becomes scattered in the contact surface at lower normal stresses, which further contributes to the hydrodynamic lubrication of water molecules.

(3) The coefficient of friction is the highest in the dry system with the same applied normal stress, followed by the salt water system, and the lowest in the pure water system. The water molecules will induce an extra interaction force between the epoxy and the silica substrate in the z-direction, while this interaction force can be weakened by the NaCl ions. This results in a higher normal force and a lower calculated coefficient of friction in the pure water system. The relationship between the roughness of the interfaces in the three different systems has also been verified by an analytical equation based on Archard’s elastic deformation friction theory.

(4) An increase in sliding velocity has a negligible effect on the calculated normal force and increases the maximum friction force, leading to an increase in the coefficient of friction. The water molecules play a minimal role as a lubricant at a higher sliding velocity during the initial sliding stage. The lubricant effect of water molecules becomes gradually apparent as the sliding velocity is reduced or the sliding stage of silica substrate has reached the steady-state zone. By analyzing the effects of sliding velocity, normal stress, water, and NaCl ions on the FRP pile-sand friction interface performance, this study can provide the fundamental insight for determining the settlement of FRP pile and the failure mechanism of the pile-soil system. It could be beneficial to estimate the load capacity in design for the FRP pile embedded in sand with different environments.

Chapter 5. Insight into enhancing foundation stability with rubber-soil mixtures: A nanofriction study

Abstract

Ground vibration during earthquakes can lead to loss of soil strength and structural damage. Rubber-soil mixtures (RSM) show promise in mitigating the residual ground deformation under dynamic loading. The influence of clay minerals on soil frictional strength and system stability is essential in the context of earthquake mechanics. This study employs molecular dynamics (MD) simulations to investigate the friction behavior of the rubber-clay interface within the RSM system. The results indicate a direct correlation between normal stress and friction force, with denser soil systems exhibiting higher friction forces, analogous to natural soils. The increase in friction can be achieved by compacting the rubber and clay components in the RSM systems. The inclusion of rubber in the RSM significantly reduces the stick-slip motion at the montmorillonite-rubber interface, providing a damping effect that reduces the intensity of the stick-slip vibration during sliding. The friction force between the montmorillonite and rubber exhibits a velocity enhancement behavior. The higher the sliding velocity, the less the adaptation time for interfacial atoms, resulting in a higher friction force. The rubber/montmorillonite surface exhibits a higher friction coefficient at higher sliding velocities, effectively limiting the buildup of shear stress responsible for initiating stick-slip behavior. Comparisons with experimental data validate the accuracy of the calculated mechanical properties, work of adhesion, and friction coefficients. These results contribute to a better understanding of the friction behavior within the RSM system, facilitating its application in improving seismic resistance.

Keywords: rubber-soil mixtures; rubber; montmorillonite; friction behavior; molecular dynamics

5.1 Introduction

Pile foundations, which rely on the strength of the soil to support entire structures, are particularly susceptible to the effect of ground vibration induced by earthquakes. Under such conditions, the interaction between the pile and soft soil can result in significant tilting and settlement of the entire system, leading to severe structural damage. As shown in **Fig. 1**, rubber-soil mixtures (RSM), which are primarily a combination of natural soil (e.g., clay and sand) and rubber granules, have potential applications in mitigating adverse effects of residual ground deformation under dynamic loading [162-165]. The use of RSM as a viable replacement for soil or rock in a wide range of fill applications has been included in ASTM standards [166]. When incorporated into the soil, the rubber granules act as a barrier to transmit seismic energy, thereby reducing the structure response during an earthquake and enhancing the stability of the foundation. As a lightweight and environmentally friendly material, the utilization of RSM shows considerable promise in improving the overall seismic resistance of structures [167, 168].

To further explore the application of RSM, extensive research has been conducted to investigate the pile-soil interaction through experiments and simulations when RSM is employed. Xiong and Li [169] conducted shaking table experiments and observed that a rubber content of 35% in the RSM layer provides effective seismic protection while meeting the superstructure bearing capacity requirements. Pitilakis et al. [170] developed a finite element model of a soil-structure system to validate the beneficial effects of using RSM as a foundation layer on the structural response under dynamic loading. Through dynamic vibration tests, Panah and Khoshay [171] demonstrated that RSM in a sleeved pile system meets the requirements of a seismic isolation system due to the energy-absorbing capabilities of the rubber particles. Tsang and Pitilakis [172] employed the finite element method to investigate the effect of soil liquefaction on pile behavior and to evaluate the improvements achieved through the utilization of RSM. Dutta and Nanda [173] found that a 2 m wide and 2.5 m deep RSM layer surrounding the pile can reduce pile head displacement by 40%.

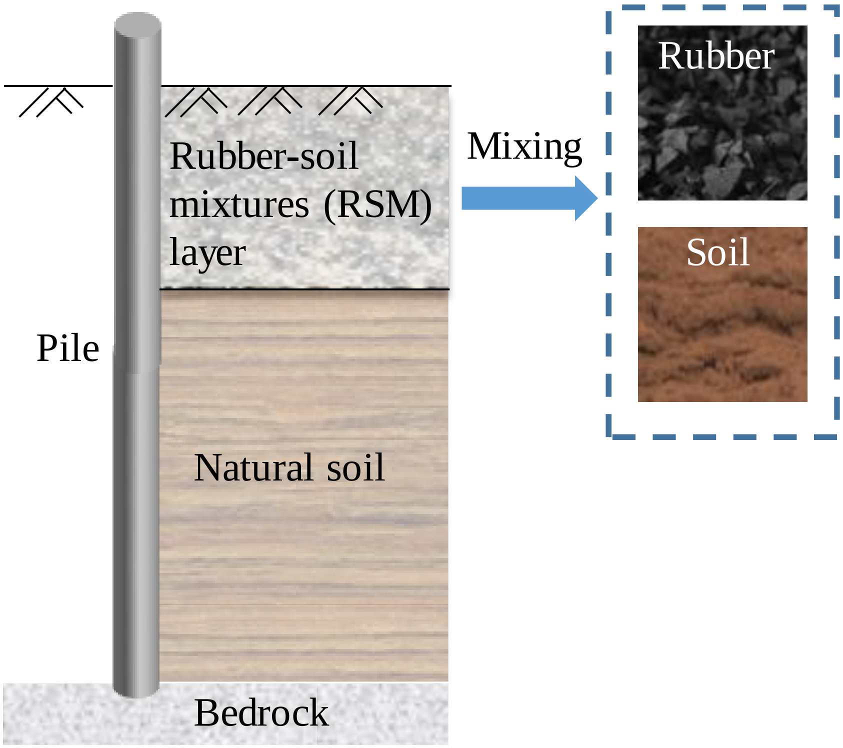

Figure 5-1 The pile foundation using rubber-soil mixtures (RSM) layer

As an abundant geomaterial, clay minerals play an important role in controlling soil behavior in geotechnical applications [174, 175]. Understanding how clay minerals influence friction strength and stability behavior in earthquake mechanics is essential for geotechnical engineering [176]. In contrast to the inelastic response of natural clay, RSM possesses important properties such as low stiffness and a nearly linear elastic response, making it an effective material for seismic isolation and contributing to the dissipation of seismic motion [177]. Therefore, the friction behavior within the RSM surrounding the pile under seismic loading differs from that of natural clay, due to the unique properties and multiphase hybrid nature of RSM. Although macroscopic experiments provide valuable insights, they may not fully elucidate the mechanisms occurring at the particle contact surface. To gain a deeper understanding of the fundamental friction mechanisms at the atomic scale, molecular dynamics (MD) simulations have proven to be an excellent tool. Researchers have recently employed MD simulations to investigate the nanoscale friction characteristics of montmorillonite, which enables the prediction of the shear strength properties of clays in geotechnical engineering [115, 174, 178]. However, the friction properties between rubber and clay within the RSM system have not yet been investigated at the nanoscale. Thus, there is a need to extend the study of friction mechanisms in rubber/clay systems from the macroscopic to the microscopic level. The simulation results will not only enhance our understanding of the intricate interactions between rubber and clay but also pave the way for more accurate modeling and design approaches for RSM in geotechnical engineering applications.

Understanding the friction behavior of RSM at different sliding velocities and normal stresses is essential for assessing their dynamic response during seismic events. Montmorillonite clay, due to its low friction coefficient and high expansibility, has a significant impact on controlling soil strength [115]. The optimal interfacial distance and work of adhesion between the montmorillonite and rubber are calculated. In the steered molecular dynamics (SMD) simulation, an external force is applied to the montmorillonite along the rubber surface. This approach allows for a comprehensive investigation of the friction behavior and underlying mechanisms within the RSM system. The friction behavior of the rubber/clay interface is investigated under different contact conditions. The variation of the normal stress and the influence of the sliding velocity on the friction coefficient for the RSM systems are thoroughly investigated. The primary objective of these simulation results is to elucidate the friction mechanism at the interface between rubber and montmorillonite in the RSM system. The findings may have implications for the design and optimization of engineering applications involving RSM materials, allowing for considerations of different soil pressures and sliding velocities.

5.2 Methodology

5.2.1 CVFF and CLAYFF force field

The accurate description of the atomic interactions using a force field is crucial for the simulation of the interface model. In this study, the Consistent Valence Force Field (CVFF) [53] is used to determine the atomic interactions in the rubber model. The CVFF has been widely used in rubber simulation studies [179-182], demonstrating its effectiveness. The CLAYFF force field [54], which is widely used for clay minerals [82, 110, 183, 184], is employed to govern the interactions between montmorillonite atoms. The intermolecular interaction between montmorillonite and rubber is non-bonding interaction contributions for van der Waals (VDW) and electrostatic potential. Both CLAYFF and CVFF utilize the identical expression for VDW energy, which is based on the 12-6 Lennard-Jones potential with the Lorentz-Berthelot combination rule [55]. The non-bonding interaction between two atoms is truncated at a cut-off distance of 10 Å. The long-range electrostatics are calculated using the the particle-particle particle-mesh method [91], with a tolerance of 10^{-4}. The timestep for the MD simulations is set to 1.0 fs and the Verlet algorithm is employed to integrate the motion equation. The simulations are performed using the LAMMPS code [87], and the visualization of the models is performed using the OVITO software [145].

5.3 Model construction

5.3.1 Montmorillonite model

In this work, the Wyoming-type Na-montmorillonite model is utilized, which consists of a tetrahedral-octahedral-tetrahedral structure. This structure includes an alumina octahedral sheet sandwiched between two silica tetrahedral sheets. The lattice parameters introduced by Viani et al. [185] are as follows: a = 5.18 Å, b = 8.98 Å, c = 15.0 Å, and $\alpha = \gamma = \beta = 90°$. The chemical formula of the model is $Na_{0.75}(Si_{7.75}Al_{0.25})(Al_{3.5}Mg_{0.5})O_{20}(OH)_4$, in which aluminum ($Al^{3+}$) and (silica) Si^{4+} are isomorphically substituted at random by magnesium (Mg^{2+}) and aluminum (Al^{3+}), respectively. This substitution scheme has been extensively investigated in various studies [183, 186-188].

To create a montmorillonite supercell, the unit cell is replicated in the in x-, y-, and z-directions, resulting in a periodic $8a \times 6b \times 4c$ supercell. The montmorillonite substrate consists of a total of 7824 atoms and has the dimensions of x = 41.4 Å, y = 53.9 Å, and z = 38.4 Å, as depicted in Figure 5-2. Here, the x-, y-, and z-directions correspond to the crystal directions (100), (010), and (001), respectively.

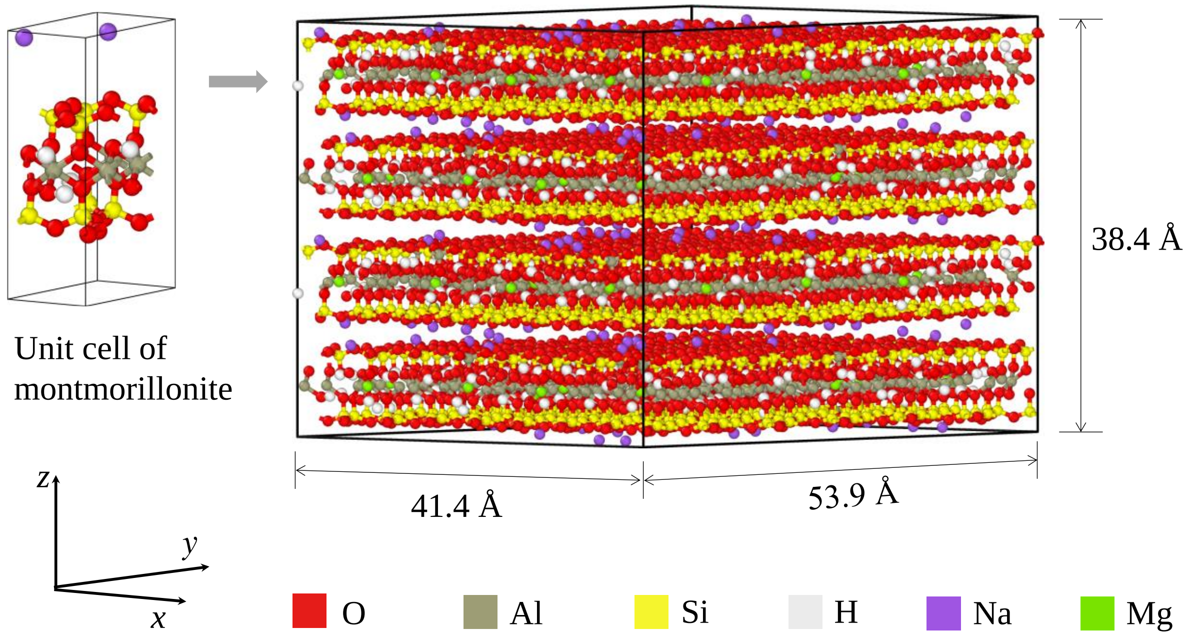

Figure 5-2 The molecular structure of the montmorillonite unit cell and the 8a × 6b × 4c montmorillonite supercell

5.3.2 Rubber model

The majority of rubber particles have diameters in the range of 1 to 2 mm and consist of material components such as rubber hydrocarbon, carbon black, acetone extracts and other components. Rubber hydrocarbon, which consists primarily of cis-1,4-polyisoprene repeating units, is the main component and constitutes 45.2% of the rubber particles [182]. In a study by Sharma et al. [189], a chain length of 32 monomeric units (n = 30) is found to adequately represent the polymer-like behavior of rubber. Therefore, in order to accurately and effectively predict the structural and mechanical properties of the rubber phase, this simulation includes 32 repeating units in a chain. The rubber model constructed for this purpose consists of a total of 20 chains and is shown in Figure 5-3. The model contains a total of 8420 atoms and is enclosed in a box with dimensions of x = 41.4 Å, y = 53.9 Å, and z = 65 Å, and $\alpha = \beta = \gamma = 90°$.

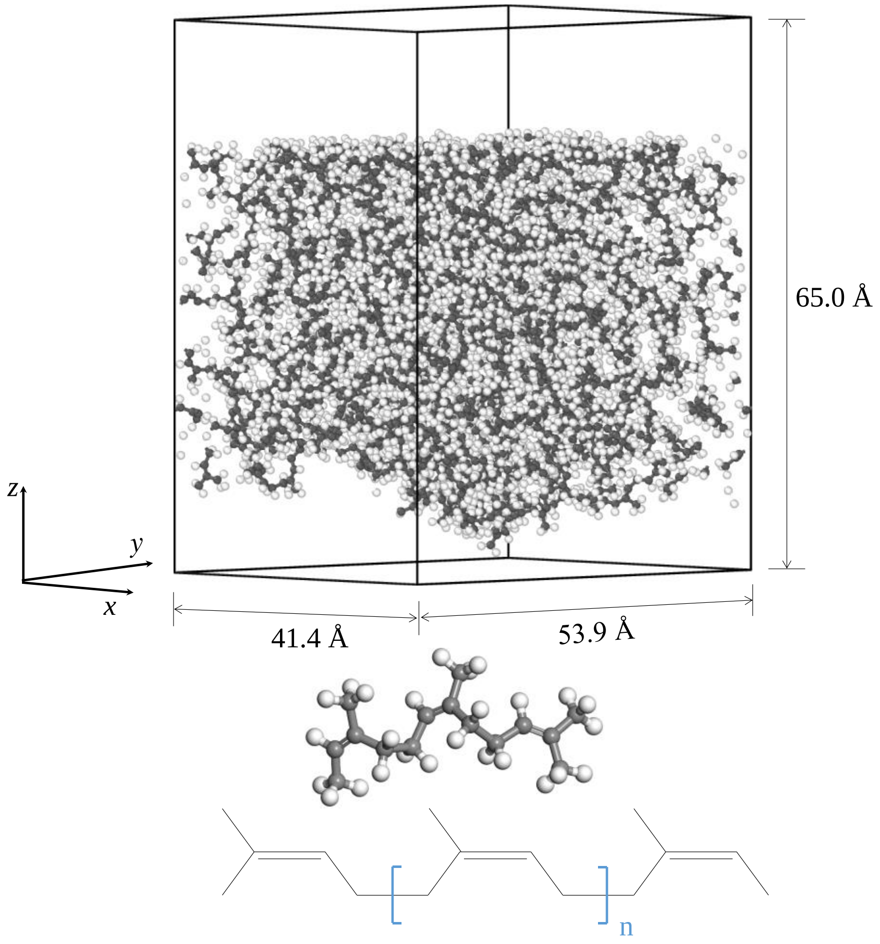

Figure 5-3 Chemical structure of cis -1,4-polyisoprene and rubber model

The calculated and experimental densities (ρ) of rubber at 298 K and 1 atm pressure have been presented in Table 5-1. Then, the glass transition temperature (T_g) of rubber is determined by analyzing the temperature dependence of the polymer density. Figure 5-4 illustrates the density of the rubber model as a function of temperature (T), ranging from 125 K to 300 K. The curve exhibits two linear regions corresponding to the glassy and rubbery states of the polymer material. The abrupt change in the slope in the density-temperature curve indicates the occurrence of the glass transition, as presented in Figure 5-4. The equilibration of the system under the NPT ensemble is carried out for 1 ns, and the density data is collected after a 0.4 ns equilibration procedure.

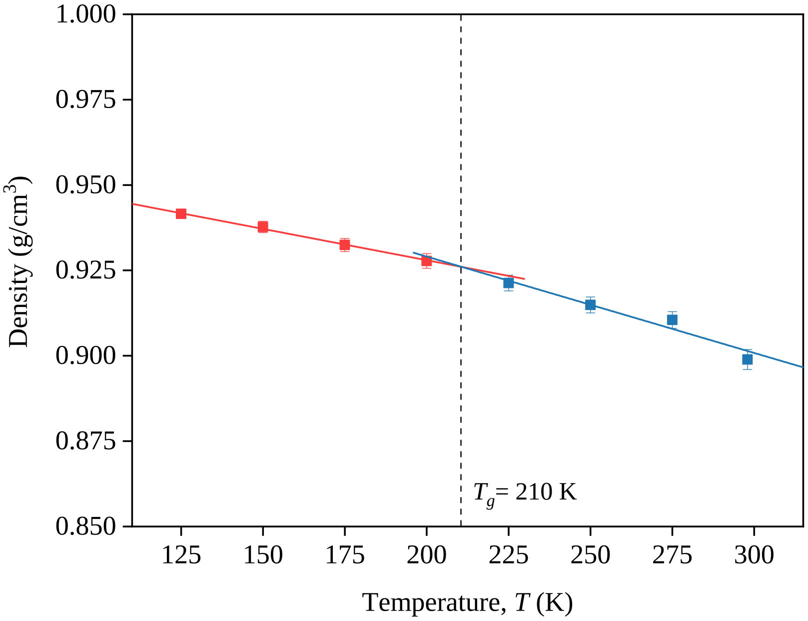

Figure 5-4 Density of rubber model with the variation of temperature

Linear regression is employed to fit the data, allowing the coefficient of thermal expansion (CTE) to be calculated from the slopes of the volume change curves, as shown in Figure 5-5. The equation for the volumetric CTE (α) is given by:

$$\alpha = \frac{1}{V}\left(\frac{\partial V}{\partial T}\right)_P \tag{5.1}$$

The values of α are calculated by analyzing the slopes of the volume-temperature curves within a temperature range above T_g [189]. The calculated α values, along with the experimental values for rubber, are also listed in Table 5-1. It is worth noting that all calculated ρ, α, and T_g values exhibit less than a 5% error when compared to the corresponding experimental values, thereby validating the accuracy of the rubber model constructed in this study.

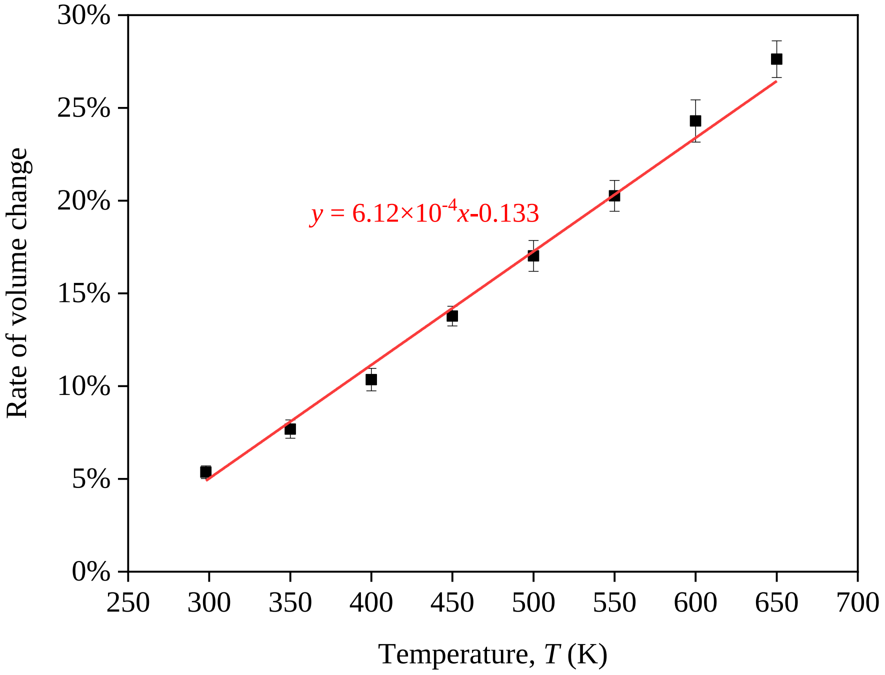

Figure 5-5 Rate of volume change with the temperature

Table 5-1 Material properties of MD simulation and experimental data for rubber

Material properties	MD simulations		Experiments [190-194]
	Present sudy	Sharma et al., 2016 [189]	
ρ (g/cm^3)	0.90	0.908	0.91
T_g (K)	210	209	200
α (K^{-1})	6.12×10^{-4}	5.1×10^{-4}	6.1×10^{-4}

5.3.3 Montmorillonite-rubber system

The schematic representation of the montmorillonite/rubber system in a box with dimensions of $x = 41.4$ Å, $y = 53.9$ Å, and $z = 110$ Å, and $\alpha = \beta = \gamma = 90°$, consisting of a total of 16244 atoms, is shown in Figure 5-6, which merges the montmorillonite model from Figure 5-2 and the rubber model from Figure 5-3.

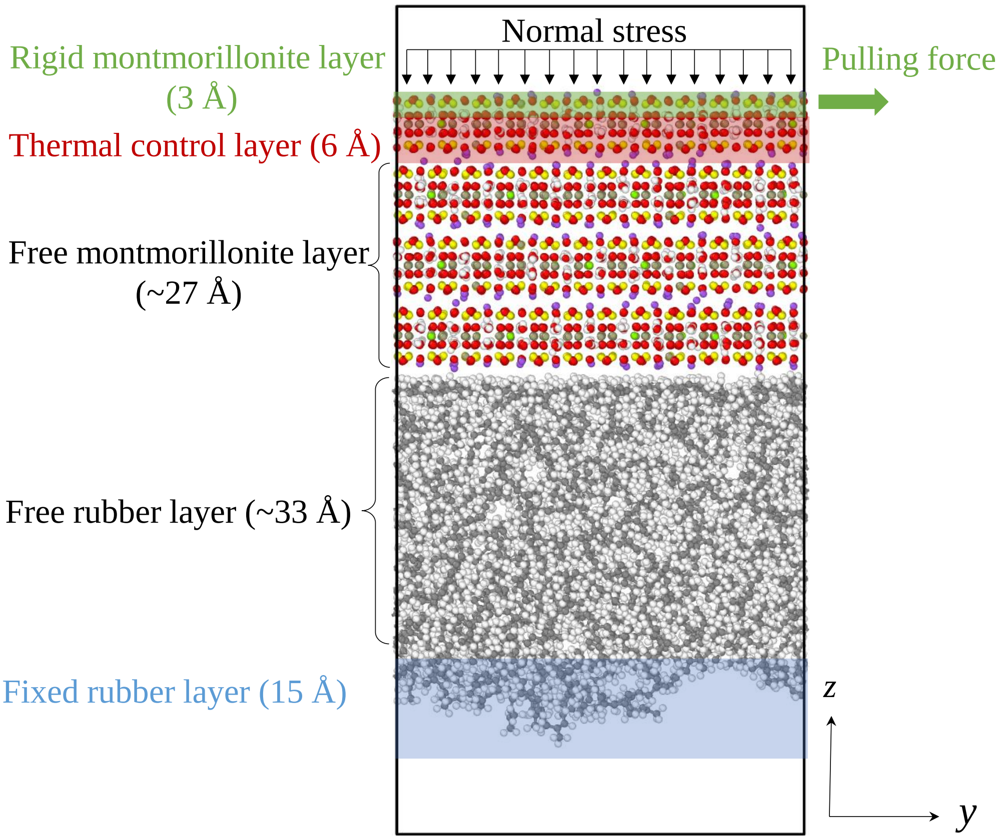

Figure 5-6 Schematic view of the montmorillonite-rubber system

To determine the optimal interfacial distance between montmorillonite and rubber, a series of simulations are run with different initial interfacial distances. These simulations were equilibrated for a duration of 1 ns within the NVT ensemble using a time step of 1.0 fs and a temperature of 300K. The plot in Figure 5-7 exhibits the relationship between total energy and interfacial distance. It is evident that the minimum total energy of the montmorillonite-rubber system is observed at an interfacial distance of 4.4 Å. As a result, the optimal interfacial distance of 4.4 Å is chosen to establish the most stable combined system, which will also serve as the basis for investigating the friction behavior between montmorillonite and rubber.

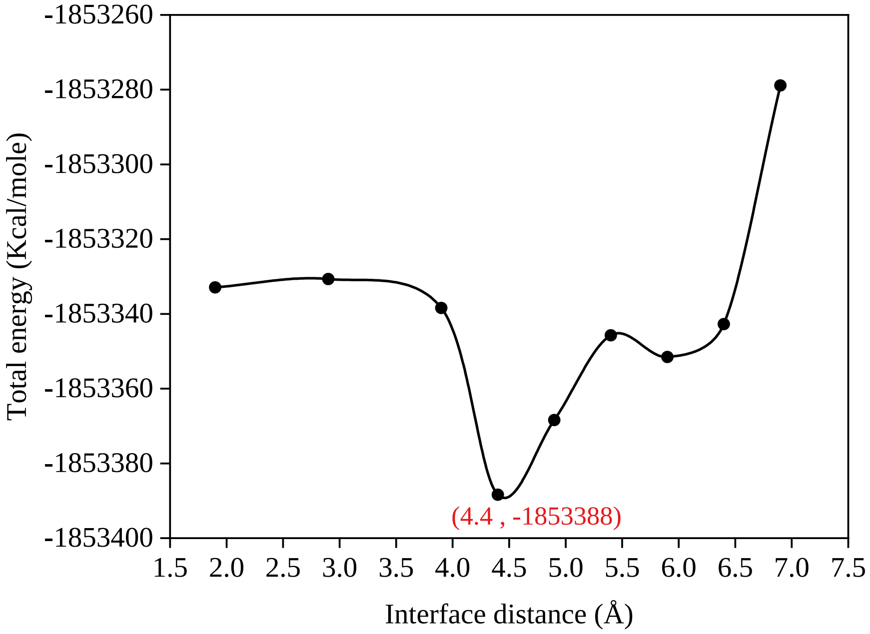

Figure 5-7 Variation of total energy of montmorillonite/rubber system with initial interfacial distance

The work of adhesion, which represents the energy required per unit area to separate an interface into two free surfaces, is a basic interfacial parameter [195]. It serves as a valuable metric for evaluating and predicting the mechanical properties of the interface between rubber and montmorillonite. The work of adhesion is calculated using the following equation:

$$W = \frac{E_M + E_R - E_{Combine}}{2A} \tag{5.2}$$

where A is the area of the contact surface; E_{combine} represents the total energy of the montmorillonite-rubber system; and, E_{M} and E_{R} correspond to the total energies of the montmorillonite and rubber systems, respectively.

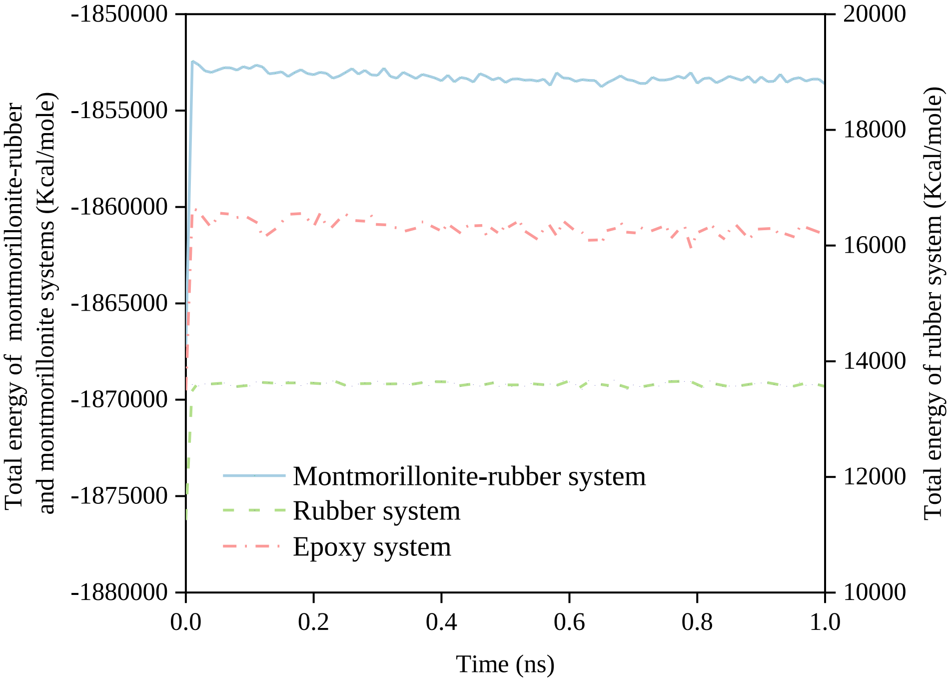

Figure 5-8 Variation of total energies of three systems with simulation time

Figure 5-8 illustrates the calculations performed in the NVT ensemble, employing a temperature of 300 K and an equilibration duration of 1 ns for the montmorillonite, rubber, and montmorillonite/rubber systems. The total energy of all three systems is determined by averaging the values after 0.1 ns in the equilibrium state. According to Eq. 5.2, the calculated work of adhesion between montmorillonite and rubber is found to be 75.2 mJ/m^2. Table 5-2 presents the experimental results of the work of adhesion between montmorillonite and rubber, indicating that the results obtained in this study are generally consistent with the experimental results. On the other hand, the calculated values are relatively smaller when compared to the results observed for montmorillonite with other polymers, such as epoxy and polystyrene.

Table 5-2 Work of adhesion for different interfacial material

Work of adhesion (mJ/m^2)	Methods	Interfacial material
75.2	MD simulation	Montmorillonite and rubber in this study
67.63	Experiments	Unmodified clay and rubber [196]

82.9		Unmodified clay and rubber [197]
70.26		Montmorillonite and rubber [198]
98.6		Montmorillonite and epoxy [118]
92.5		Montmorillonite and polystyrene [199]

5.4 Simulation details

The simulation box dimensions of the montmorillonite/rubber system are x = 41.4 Å, y = 53.9 Å, and z = 110 Å, with $\alpha = \beta = \gamma = 90°$. As shown in Figure 5-6, the system is partitioned into five distinct sections, arranged from top to bottom as follows:

(a) a rigid montmorillonite layer (3 Å) experiencing normal stress and pulling force, without undergoing structural deformation.

(b) a thermal control layer consisting of a free montmorillonite layer (6 Å)

(c) another free montmorillonite layer (~27 Å)

(d) a free rubber layer (~33 Å)

(e) a fixed rubber layer (~15 Å) to keep the system stable.

To prevent interaction between the montmorillonite and the rubber on the opposite side, an appropriate vacuum region is created in the system along the z-direction. Periodic boundary conditions are employed in both the x- and y-directions to address boundary effects in the model. The thickness of the free layer is set to be larger than the cutoff distance in the model to minimize the influence of the rigid and fixed layers on the contact surface between the montmorillonite and rubber.

A MD simulation conducted at 300 K revealed an ultimate stress of 28.05 GPa for Na-montmorillonite in the z-direction [200]. To prevent structural failure, a series of normal stresses from 1 to 10 GPa are selected, which are well below the reported ultimate stress. The macroscopic velocity of earthquake-induced sliding motion of the soil can reach 30 m/s [201]. Since there is a lack of existing literature specifically addressing the friction force and sliding velocity in atomic-scale RSM systems, the values employed in this study are based on comparable parameters reported in previous nanofriction simulations. A range of values for normal stress (1 to 10 GPa) and sliding velocity (10 to 100 m/s) are employed, which have been previously utilized by several researchers investigating interfacial friction [115, 202-205].

Table 5-3 illustrates the simulation procedures for the friction process, wherein the minimization procedure is implemented to determine the geometric conformation of all models using the conjugate gradient method. Then, simulations of the montmorillonite-rubber system are conducted under various normal stresses within the NVE ensemble for a duration of 1 ns, allowing the systems to reach their equilibrium states. Simultaneously, a thermal control layer composed of montmorillonite is employed to maintain the system at a constant temperature, which is achieved by thermally scaling the atom temperatures to 300 K using the Langevin algorithm [87] with a damping constant of 100 fs. Once relaxation is achieved for all systems, the interfacial friction process is simulated using SMD simulations. In the following step, the rigid layer of montmorillonite is subjected to constant-velocity pulling forces for the interfacial friction behavior between montmorillonite and rubber, thus simulating shear phenomena. This similar configuration for simulating friction has been previously documented by Dai et al. [206], Chatterjee et al. [128], Chen et al. [123], and Yuan et al. [202].

Table 5-3 Procedures for the SMD simulation of montmorillonite-rubber system

Step	Procedures	Configurations
1	Minimize	Conjugate gradient method
2	Equilibrium	a) Apply NVE ensemble to the system and run for 1 ns. b) Apply normal stress on the rigid montmorillonite layer. c) Maintain temperature in the thermal control layer of montmorillonite using the Langevin algorithm.
3	SMD	Based on the Equilibrium stage, perform a series of SMD simulations by pulling the rigid montmorillonite layer with constant velocities along the horizontal (*y*) direction.

5.5 Results and discussions

5.5.1 Influence of normal stress on friction behavior

The ground vibration during earthquakes induces a decrease in effective stress, leading to a decrease in the friction forces between soil particles. An effective approach to improve liquefaction resistance is soil densification, aiming to achieve a relative density greater than 70% as recommended by studies [207, 208]. To investigate the similarity of particle friction in the RSM system to that of natural soils, SMD simulations are utilized. These simulations enable the examination of friction behavior between montmorillonite and rubber under various normal stress conditions.

Figure 5-9 illustrates the variation of the friction force with the sliding distance in the *y*-direction under normal stresses of 1 GPa, 5 GPa, and 10 GPa. The friction force gradually increases with increasing sliding distance and reaches a stabilized state after 5 nm. In addition, the friction force tends to increase with the increase of normal stress level. A higher normal stress can result in a denser RSM. These findings indicate that the behavior of the RSM system is similar to that of natural soils, where denser soil systems typically exhibit higher friction forces. Consequently, in the design of RSM systems, enhancing the friction force can be achieved through the compaction of the rubber and clay components. This approach holds the potential to significantly improve the engineering applications of RSM.

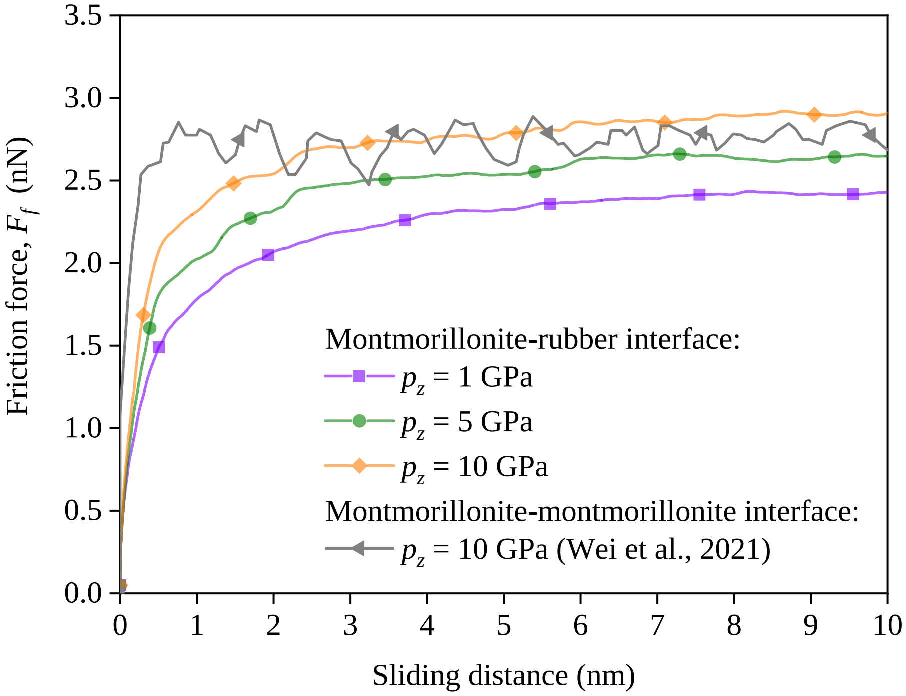

Figure 5-9 Friction force versus sliding distance curve under various normal stresses

Figure 5-9 also provides a force-displacement curve of the hydrated montmorillonite-montmorillonite interface, revealing the presence of a pronounced stick-slip effect during the sliding process. These results are obtained from an MD simulation performed by Wei et al. [115], where the interface was subjected to a normal stress of 10 GPa and a sliding velocity of 100 m/s. The occurrence of stick-slip friction holds considerable effect in stability and behavior of the soil during the earthquake [209]. During the slipping phase of stick-slip behavior, the rapid movement of soil particles may create a pumping effect that draws water into the voids between the soil particles. It has been reported by Finnegan et al. [210] that higher pore water pressures are accompanied by a more frequent occurrence of the stick-slip behavior. Therefore, when the soil exhibits stick-slip behavior, the increase in pore water pressure during the slip phase reduces the effective stress and shear strength of the soil, making it more susceptible to liquefaction.

It is worth noting that the presence of stick-slip motion at the montmorillonite-rubber interface is significantly reduced, as shown in Figure 5-9. This reduction can be attributed to the influence of the rubber component within the RSM system. Earlier experimental results indicate that the inclusion of smooth rubber blocks in the friction system contributes to a certain degree of reduction in stick-slip vibration intensity compared to the original friction system without rubber blocks [211]. The incorporation of rubber in soils provides damping effects and increases the energy dissipation during sliding [212]. This damping effect reduces the magnitude and frequency of the stick-slip cycles, thereby minimizing the occurrence of stick-slip behavior. Then, the reduction of stick-slip behavior within the RSM system reduces the fluctuation of pore water pressure within the soil. Then, the general response of the foundation resting on the RSM system may be reduced when subjected to seismic excitation.

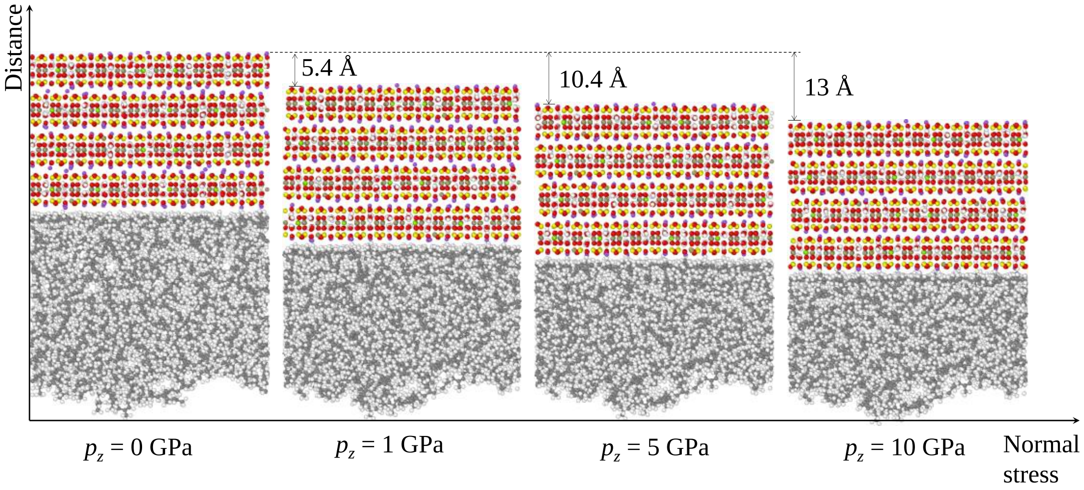

Figure 5-10 Snapshots of interfacial friction behavior at different normal stresses

The snapshots of the interface structure at different normal stresses (0, 1, 5 and 10 GPa) are shown in Figure 5-10. Observation of the snapshots shows that as the normal stress increases, the distance between the top of the montmorillonite and the bottom of the rubber gradually decreases, indicating progressive compression of the RSM system. The distances of 5.4, 10.4 and 13 Å represent the reduction distances of the montmorillonite/rubber system under normal stress of 1, 5, and 10 GPa in the *z*-direction, respectively. Sliding motion between two surfaces requires the expenditure of energy to overcome the adhesive forces that impede their relative motion [213]. The reduced distance between the two layers allows more atoms to interact. The increased normal stress results in a corresponding increase in van der Waals forces between the montmorillonite and rubber. The stronger van der Waals forces contribute to the intermolecular interactions between montmorillonite and rubber, increasing the surface friction force and influencing their adhesive properties and overall interface behavior.

To better understand the interaction between two surfaces, the Radial Distribution Function (RDF), also called $g(r)$, defined as the probability of finding an atom at a distance r from another atom chosen as a reference, is calculated. The RDF is used to reveal the atomic distribution and possible interactions between the rubber and the montmorillonite. The RDF curves of carbon (C_R) and hydrogen (H_R) atoms in rubber with atoms in montmorillonite are shown in Figure 5-11. Distinct peaks can be observed in the RDF curves of C_R and H_R with tetrahedral atoms (O_M, Si_M) and Na ions in montmorillonite, but not with octahedral atoms (Al_M, H_M). In particular, the position of the first peak of $g_{C_R\text{-}Na_M}(r)$ is found 2.8 Å and for $g_{H_R\text{-}Na_M}(r)$ is 2.8 Å, indicating that sodium ions can act as a bridge between the rubber and montmorillonite, attracting the nonpolar rubber to bind to the polar MMT surface. Furthermore, the positions of the first peaks of $g_{C_R\text{-}O_M}(r)$, $g_{H_R\text{-}O_M}(r)$, $g_{C_R\text{-}Si_M}(r)$ and $g_{H_R\text{-}Si_M}(r)$ are 3.6 Å, 2.7 Å, 4.0 Å and 3.5 Å, respectively. The interaction distance between the rubber and montmorillonite is 2.7 to 4.0 Å, suggesting that their interaction is mainly dominated by van der Waals forces through cation bridging.

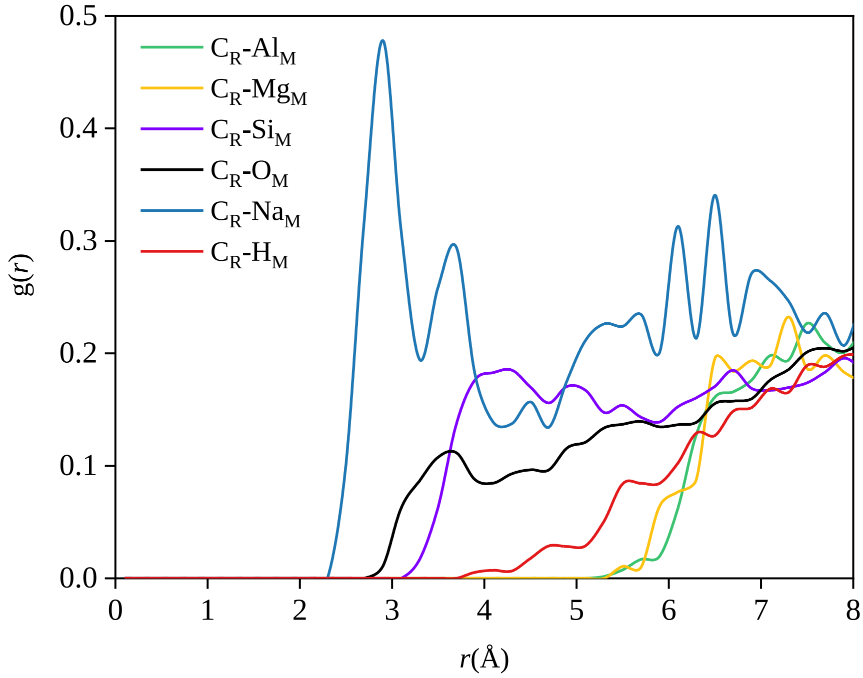

(a)

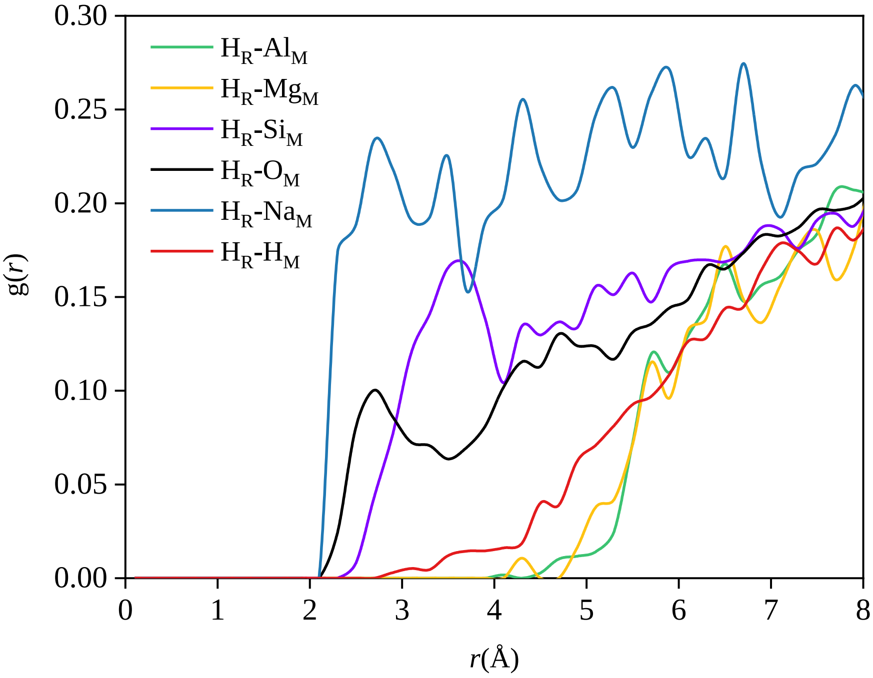

(b)

Figure 5-11 RDF curves of (a) carbon atom of rubber and various atoms of montmorillonite and (b) hydrogen atom of rubber and various atoms of montmorillonite (Note that the subscript M and R denote montmorillonite and rubber, respectively)

5.5.2 Influence of sliding velocity on friction behavior

The friction force between two surfaces at the nanoscale is influenced by several factors, and the sliding velocity is one of the critical parameters. At the nanoscale, the relationship between friction force and sliding velocity might exhibit unique characteristics due to the dominance of various nanoscale phenomena. In order to explore the effect of sliding velocity on friction behavior, the relationships between the pulling force and sliding displacement are studied at the sliding velocities ranging from 10 to 100 m/s. The normal stress applied to the rigid montmorillonite layer is 10 GPa.

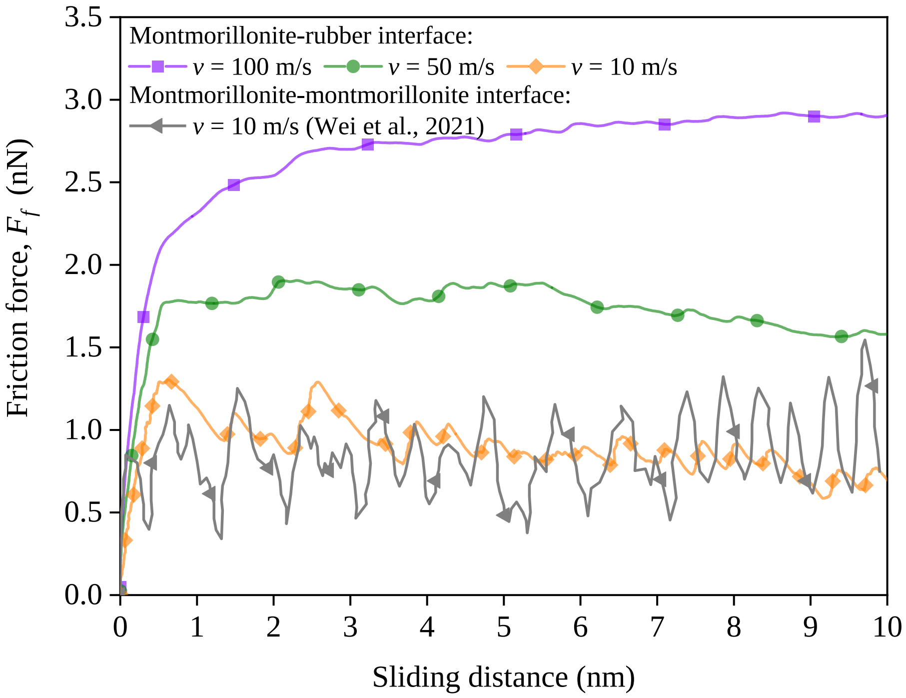

Figure 5-12 Friction force versus displacement curve under different sliding velocities

Figure 5-12 illustrates a clear correlation between sliding velocity and friction force, indicating that the friction force increases as the sliding velocity increases. At the nanoscale, the friction force between montmorillonite and rubber exhibits a velocity-dependent behavior, manifesting the velocity enhancement phenomenon resulting from intricate interactions between surface structures. As the sliding velocity increases, the contact time between the montmorillonite and rubber surfaces decreases, leaving less time for the interfaces to adjust and adapt to each other. Then, sliding at higher velocities will induce surface rearrangement or reconstruction processes. Due to the limited time available, the montmorillonite/rubber surface may not have the opportunity to rearrange into a more favorable configuration at faster sliding velocities, contributing to the observed increase in surface friction force.

As mentioned earlier, stick-slip behavior is commonly observed in nanoscale friction. Stick-slip motion is observed at a sliding velocity of 10 m/s, but not at faster sliding velocities (50 and 100 m/s). In order to study the stick-slip behavior at a sliding velocity of 10 m/s, the results of MD simulations for the montmorillonite-montmorillonite interface subjected to a normal stress of 10 GPa and a sliding velocity of 10 m/s are introduced for comparison [115].

The results reveal a significant increase in the occurrence of stick-slip motion compared to the calculated results for the montmorillonite/rubber interface at lower sliding velocities. This finding is consistent with the weakened stick-slip phenomenon observed in Figure 5-9, reconfirming the role of rubber in mitigating stick-slip motion in the friction behavior of the RSM system. Therefore, the differences in material properties between the rubber/montmorillonite and montmorillonite/montmorillonite interfaces result in increased adhesion forces and sliding resistance for the montmorillonite/montmorillonite interface, leading to more pronounced stick phases during sliding.

The interfacial friction coefficient plays a key role in the analysis of the interfacial friction process, and its calculation is determined by the formula [214, 215]:

$$\mu = \frac{F_f}{F_n} \tag{5.3}$$

where F_f denotes the friction force, μ represents friction coefficient, F_n is the applied normal force. The peak interface friction coefficient is an important parameter to analyze the interface friction process, which is calculated by the formula [129]:

$$\mu_p = C_1 \ln\left(p_z\right) + C_2 \tag{5.4}$$

where C_1 and C_2 are the constants, and μ_p is the peak interface friction coefficient, which is obtained from the average value of the friction coefficient after sliding 3 nm. It can be seen in Figure 5-13 that an increase in the normal stress results in a concomitant decrease in the interface friction coefficient, a trend that is consistent with the findings from the interface shear test between polymer and soil [129]. In addition, the rubber/montmorillonite surface has a higher friction coefficient with higher sliding velocity, which effectively limits the buildup of shear stress responsible for initiating stick-slip behavior. This increasing sliding velocity between the rubber and clay surfaces promotes smoother sliding motion, thereby reducing the likelihood of abrupt movements commonly associated with stick-slip behavior.

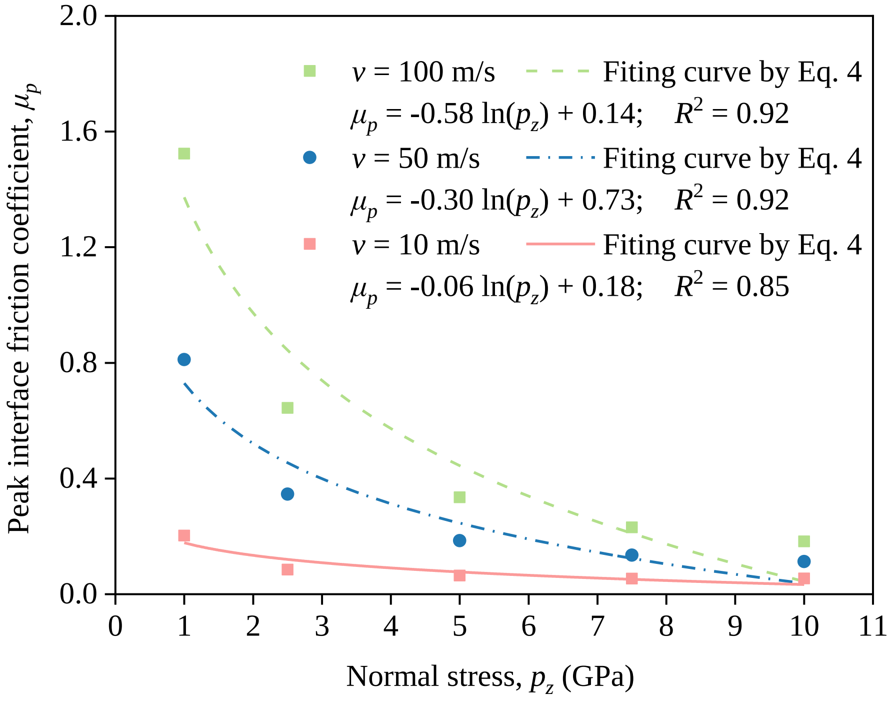

Figure 5-13 Variation of peak interface friction coefficient with normal stress

Table 5-4 presents the results of the current calculations along with relevant experimental data on the friction coefficient. The friction coefficients calculated in our study show a consistent agreement with the results of previous research. Slight differences are observed between the results of this study and those of previous investigations due to factors such as scale effects, moisture content, sliding velocity, and other relevant variables.

Table 5-4 The calculated friction coefficient with previous experimental results

Friction coefficient	Methods	Notes
0.05 to 0.2; 0.11 to 0.81; 0.18 to 1.52	MD simulation	Montmorillonite and rubber with sliding velocity of 10, 50, and 100 m/s in this study
0.50	Sliding wear test [216]	Butadiene rubber and unmodified montmorillonite
0.28 to 0.43	Laboratory experiment [217]	Rubber and sandy clay (33.3% clay ratio)

0.30 to 2.34	Atomic force microscope experiment [218]	BIMS rubber and nanoclay (8 to 16 parts per hundred grams of rubber)
0.03 to 0.33	Biaxial frictional testing [219]	Na-montmorillonite and Na-montmorillonite with different relative humidity. Values are obtained at shear displacement of 10 mm and normal stress of 10 MPa

5.6 Conclusions

Understanding the friction behavior of rubber/soil interfaces of RSM has potential implications for mitigating structure response and enhancing the stability of geotechnical structures in seismic regions. In this study, extensive investigations of the friction behavior and mechanism within the RSM system are carried out using MD simulations between the montmorillonite/rubber interface. The main findings can be summarized as follows:

(1) The friction force between montmorillonite and rubber increases with sliding distance and is influenced by the applied normal stress. Compacting the rubber and clay components in the RSM system can increase friction force, resulting in the improved mechanical properties of RSM in engineering applications.

(2) The inclusion of rubber in the RSM system significantly reduces the stick-slip motion at the montmorillonite/rubber interface in comparison to the original friction system without rubber. This leads to a potential reduction in the general response of foundations based on RSM systems when subjected to seismic excitation.

(3) The observed correlation between sliding velocity and friction force indicates that as the sliding velocity increases, the friction force between montmorillonite and rubber also increases. This velocity dependent behavior of the friction force is attributed to the nanoscale velocity enhancement phenomenon. Sliding at higher velocities limits the time for interfacial adaptation and rearrangement, contributing to the observed increase in friction force between montmorillonite and rubber.

(4) Stick-slip motion is observed at a sliding velocity of 10 m/s, but not at higher sliding velocities (50 and 100 m/s) at the montmorillonite-rubber interface. The higher sliding velocity at the rubber/montmorillonite interface limits the buildup of shear stress responsible for initiating stick-slip behavior, promoting smoother sliding motion and reducing the likelihood of abrupt movements associated with stick-slip behavior.

(5) The optimal interfacial distance and work of adhesion between the montmorillonite and rubber are calculated to be 4.4 Å and 75.2 mJ/m^2, respectively. Comparison of the mechanical properties, work of adhesion, and friction coefficients with relevant experimental data shows consistent agreement, confirming the validity of the constructed interface model.

Chapter 6. Formulation and numerical applications of efficient pile-soil integrated element considering structural inelasticity

Abstract

The prediction of pile behavior under extreme loading is an essential consideration in the design. The pile behavior at a large displacement level is governed by the pile-soil interaction and the material inelasticity. The conventional numerical model using a large number of elements is inefficient for modelling the nonlinear pile-soil interaction and structural inelasticity in finite element analysis. To accurately and effectively evaluate the behavior of piles under extreme loading, this work develops a pile-soil integrated element considering structural inelasticity. The pile-soil interaction force can be efficiently evaluated according to the soil resistance at the Gauss integration points. The different types of *p-y* and *t-z* curves can be applied in this element to represent soil properties at any soil depth. Zero-length plastic hinges at the ends and middle of an element are used to capture the inelastic behaviour of a pile. The plastic hinges and the soil springs are integrated into the proposed element formulations, and thus one element type is sufficient to conveniently simulate the nonlinear pile-soil interactions. Comparisons between the results of the elastic pile element and the data from published literature and field tests are provided to validate the accuracy and efficiency of the proposed method.

Keywords: Finite-element method; inelastic analysis; pile-soil interaction; nonlinear analysis; plastic hinges

6.1 Introduction

The prediction of settlement and lateral deflection of the pile foundation plays an essential role in engineering practice. The behaviors of the pile and its surrounding soil are usually considered linear and elastic in design [220-222]. However, the linear elastic analysis fails to predict pile behaviours accurately in the large deformation range [223-226]. The inelastic response of the pile's material affects the behavior of the pile-soil system under heavy loading conditions. On the other hand, the pile-soil interaction is highly nonlinear due to the complicated geological conditions, especially when the pile is embedded in multi-layered soils [227-230]. For a proper design of piles under heavy loading in complicated geological conditions, the soil and material nonlinearity should be explicitly considered in the analysis.

Several studies have been conducted on simulations of the inelastic behavior of piles, which can be classified into two main categories: distributed plasticity and plastic hinge models. Some researchers [221, 231-233] developed the distributed plasticity model to simulate the material nonlinearity of the pile at any cross-section, which subdivided the cross-section of elements into fibers. The distributed plasticity model is sophisticated but computationally expensive, and its computational time is over ten times longer than that of the plastic hinge model [234]. Such an inefficiency is more profound for a large-scale three-dimensional (3D) soil-structure integration analysis with thousands of piles.

In the plastic hinge model, the pile is assumed to remain elastic except at the critical location where the plastic hinge is allowed to form [235]. Chai [236] developed a simplified model to simulate the lateral response of the pile-soil system by an equivalent fixed-base cantilever with a single plastic hinge (SPH). However, the nonlinearity of the soil and the influence of the inelastic behavior of partially embedded piles are not considered [237]. Budek et al. [238] conducted the finite element (FE) analysis of the pile-soil system subjected to lateral loading. The total plastic bending deformation within the plastic zone is represented by the zero-length SPH. The SPH model has also been adopted by Song et al. [239] to determine the ductility of piles in several selected limit states. Chiou et al. [240, 241] and Zhang et al. [242] extended the SPH to the plastic zone with numerous plastic hinges through the software SAP2000. This model tracks the development of the plastic zone by using numerous plastic hinges within the possible plastic zone of the pile. The location and size of the plastic zone are necessary to estimate in advance to determine the plastic deformation of the pile shaft.

In addition to the modelling of the structural inelasticity, the nonlinear pile-soil interaction is commonly considered by the discrete spring elements model [15, 238, 240-249]. The pile-soil system is simplified to the pile being represented by structural beam elements and the soil resistance being represented by nonlinear discrete spring elements. The actual soil resistance distribution along the pile is approximated as a series of equivalent point loads acting on the element nodes via discrete springs. The length of the structural beam element cannot be too large in order to adequately capture the nonlinearity of pile-soil interaction; otherwise, it will lead to serious inaccuracies. Therefore, this model inevitably requires extensive structural beam elements and spring elements, especially when the *p-y* or *t-z* curves are highly nonlinear. Recently, Li et al. [250] developed the elastic pile element (EPE) model to robustly simulate the behaviors of the pile under loadings in 3D analysis. The soil springs are directly incorporated into the element formulation by the Gauss-Legendre integration method to consider the variations of soil resistance within the element. The soil spring elements are unnecessary, and much fewer elements are required, which significantly increases the efficiency of the FE analysis of the pile-soil system. However, the EPE model assumes the pile material is elastic, which would lead to errors in the prediction of pile behaviour under heavy loading conditions. To the authors' knowledge, although piles are one of the important components of a structure, there is no specific element type that can integrally simulate the pile-soil system in FE models considering both soil nonlinearity and structural inelasticity. The implementation of the specific element analysis for the pile-soil system has the potential to promote the coupling analysis between the pile-soil system and the superstructure.

Therefore, based on the previous studies on 3D EPE model, this work aims to develop a pile-soil integrated element that can conveniently simulate the soil and material nonlinearity. The material-yielding and nonlinear soil-pile interactions are considered through zero-length plastic hinges and soil springs, respectively. The plastic hinges are assigned at the ends and middle of the element. The hinges and the soil spring are directly integrated into this element formulation avoiding the tedious modelling process in the conventional analysis method. In this work, the definitions and formulations of the proposed method are given. The numerical solution procedure for calculating the pile response in the geometrically nonlinear analysis is introduced. The proposed method is compared with the existing numerical solutions and validated against field tests of axially and laterally loaded piles.

6.2 Numerical model

As shown in Figure 6-1, a pile subjected to axial and lateral loads embedded in different soil layers, L_1 to L_j, is simulated by the proposed model. To address the limitation of the EPE model, this work extends its element formulations by reformulating the element stiffness matrices and nodal forces to allow inelastic analysis of pile behavior. The co-rotational formulation [251, 252] is employed in this study to decompose the motion of elements into rigid body and pure deformation components by utilizing a local coordinate system of continuous rotations and translations. The element formulations are derived from the local coordinate system, where the deformations of the element are captured. The origin of the coordinate system is located at the middle of the element. Due to the existence of the internal plastic hinge in the middle of an element, the proposed element has six internal degrees of freedom in the 3D space compared to the conventional beam-column element. The plastic hinges are also added to the element ends so that each element allows the development of three plastic hinges, which can reflect inelastic behavior and allow for large deformation along the pile length. There is no need to estimate the location of plastic hinge regions in advance. The internal degrees of freedom are further incorporated into the element stiffness matrix using the static condensation algorithm [253]. Therefore, there is no additional degree of freedom generated in the global stiffness equation, which provides simplicity and convenience to calculation programs. The plastic hinges at the two ends and middle of an element have also been used to solve various types of structural inelastic analysis problems [254-257].

The soils surrounding the pile are modeled as a series of zero-length soil springs and integrated into the element formulations. The properties of the soil springs in horizontal and vertical directions are described by using *p-y* curves and *t-z* curves, respectively. The *Q-z* curve is also assigned to describe the relationship between the end bearing capacity and the axial displacement of the pile toe. The pile-soil interaction force can be efficiently evaluated according to the soil resistance at the Gauss integration points, and the different types of *p-y* and *t-z* curves can be applied in this element to represent soil properties at any soil depth with the plastic development of surrounding soil during loading.

This proposed element is developed based on the following assumptions: (a) The portion of elements except for the plastic hinges which have been formed is assumed to remain elastic; (b) The Euler-Bernoulli assumption is adopted; (c) warping deformation is not considered; and,

(d) pile material is homogeneous and isotropic.

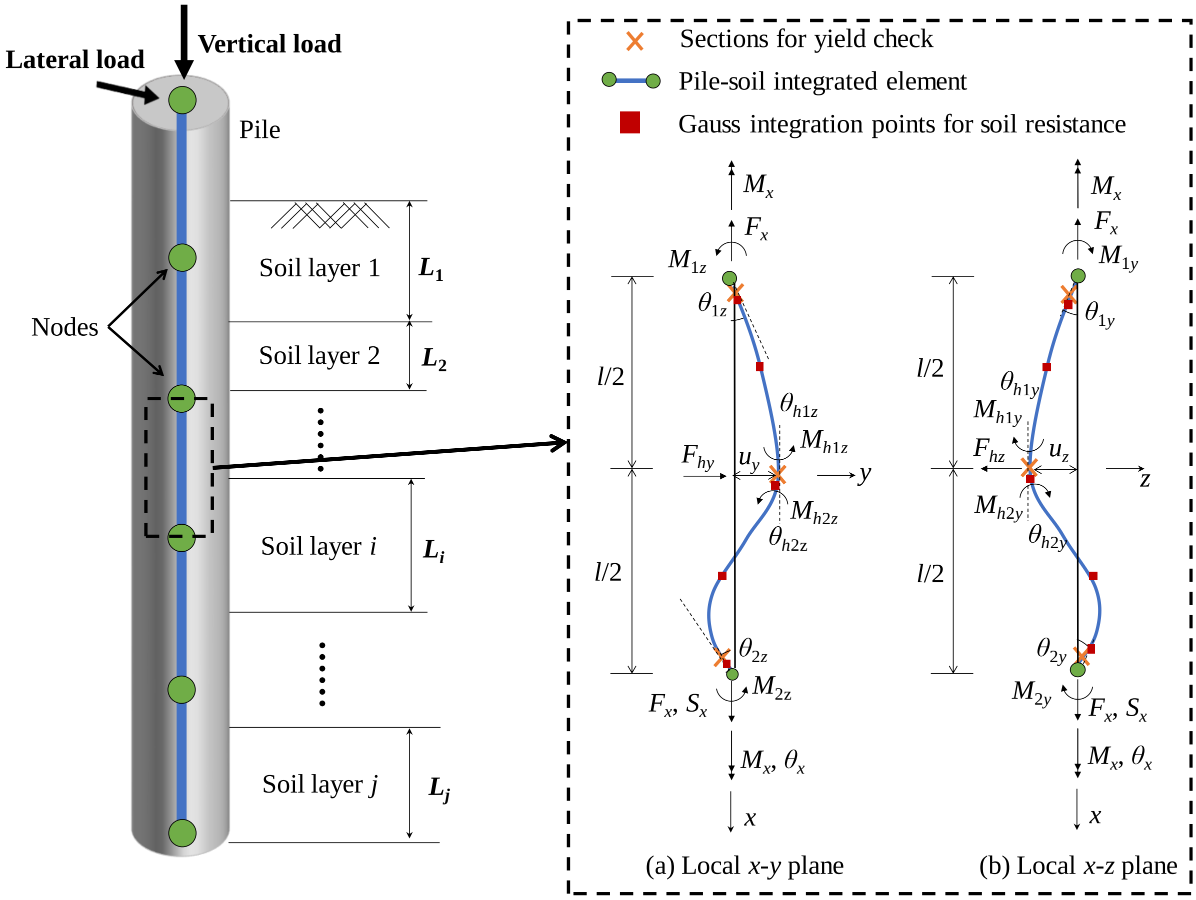

Figure 6-1 Proposed 3D pile-soil integrated element considering structural inelasticity

6.3 Proposed element formulations

6.3.1 Total potential energy

The total potential energy of the element for the pile-soil system is given by:

$$\Pi = U_E + U_S + V \tag{6.1}$$

where U_E is the element strain energy for the pile; U_S is the element strain energy for the soil springs; and, V is the external work done.

The strain energy function can be calculated by:

$$
\begin{aligned}
U_E &= \frac{1}{2}\int_{-\frac{l}{2}}^{\frac{l}{2}} E_p A \dot{s}_x^2(x)dx + \frac{1}{2}\int_{-\frac{l}{2}}^{\frac{l}{2}} E_p I_y \ddot{s}_y^2(x)dx + \frac{1}{2}\int_{-\frac{l}{2}}^{\frac{l}{2}} E_p I_z \ddot{s}_z^2(x)dx + \frac{1}{2}\int_{-\frac{l}{2}}^{\frac{l}{2}} GJ\dot{t}_x^2(x)dx \\
&+ \frac{1}{2}\int_{-\frac{l}{2}}^{\frac{l}{2}} F_{xE}\dot{s}_y^2(x)dx + \frac{1}{2}\int_{-\frac{l}{2}}^{\frac{l}{2}} F_{xE}\dot{s}_z^2(x)dx + \int_{\theta_{h2y}}^{\theta_{h1y}} E_p I_y R_y d\theta + \int_{\theta_{h2z}}^{\theta_{h1z}} E_p I_z R_z d\theta
\end{aligned}
\tag{6.2}
$$

in which l is the element length; E_p is Young's modulus of the pile; A is the cross-sectional area of the pile; $I_y(x)$ and $I_z(x)$ are the second moments of area in the y- and z-axis, respectively; G is the shear modulus of the pile; R_y and R_z are the parameters of material plasticity in the y- and z-axis, respectively; and J is the torsional constant of the pile; and, $s_x(x)$, $t_x(x)$, $s_y(x)$, and $s_z(x)$ are the vertical displacement along the x-axis, torsional rotation along the element length, lateral displacements along y- and z-axes, respectively, as shown in Figure 6-2, which are defined by interpolation functions given by:

$$
s_x(x) = \frac{l+2x}{2l} S_x \tag{6.3}
$$

$$
t_x(x) = \frac{l+2x}{2l} \theta_x \tag{6.4}
$$

$$
s_y(x) = \begin{cases} \dfrac{(l-4x)(l+2x)^2}{l^3} u_y + \dfrac{x(l+2x)^2}{l^2} \theta_{h1y} + \dfrac{2x^2(l+2x)}{l^2} \theta_{1y}, & -\dfrac{l}{2} \le x \le 0 \\ \dfrac{(l+4x)(l-2x)^2}{l^3} u_y + \dfrac{x(l-2x)^2}{l^2} \theta_{h2y} - \dfrac{2x^2(l-2x)}{l^2} \theta_{2y}, & 0 \le x \le \dfrac{l}{2} \end{cases} \tag{6.5}
$$

$$
s_z(x) = \begin{cases} \dfrac{(l-4x)(l+2x)^2}{l^3} u_z + \dfrac{x(l+2x)^2}{l^2} \theta_{h1z} + \dfrac{2x^2(l+2x)}{l^2} \theta_{1z}, & -\dfrac{l}{2} \le x \le 0 \\ \dfrac{(l+4x)(l-2x)^2}{l^3} u_z + \dfrac{x(l-2x)^2}{l^2} \theta_{h2z} - \dfrac{2x^2(l-2x)}{l^2} \theta_{2z}, & 0 \le x \le \dfrac{l}{2} \end{cases} \tag{6.6}
$$

where S_x is the axial deformation along the element; θ_x, θ_y, and θ_z are the rotations along the corresponding coordinate axes, respectively; u_y and u_z are the lateral deflections at the plastic hinge along y- and z-directions, respectively; and, θ_h is the rotation at the plastic hinge position. Throughout this work, the subscripts x, y, and z denote the corresponding axial directions, and subscripts 1 and 2 denote the two ends of an element, respectively. The above nodal deformations for the 3D element are illustrated in Figure 6-1.

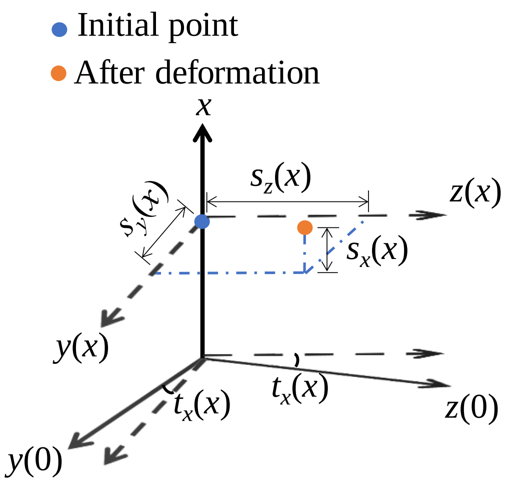

Figure 6-2 The deformation of a point in local coordinate

A series of zero-length soil springs are included within the element to consider both lateral and vertical soil resistance, which can be obtained from *p-y* and *t-z* curves. The *p-y* and *t-z* curves can be highly nonlinear and may require modification for specific issues such as the layering effect. It is difficult to describe all types of *p-y* and *t-z* curves by a specific analytical solution. Therefore, generalized semi-analytical solutions based on the Gauss-Legendre method have been developed to handle any form of *p-y* and *t-z* curves. Based on the Gauss-Legendre integration method, the strain energy of soil springs is given by:

$$U_S = \int_{-\frac{l}{2}}^{\frac{l}{2}}\int_0^{\rho} p_\rho d\rho dx + \int_{-\frac{l}{2}}^{\frac{l}{2}}\int_0^{x} p_x dx dx \approx \frac{l}{2}\sum_{m=1}^{n} W_m \kappa_{\rho,m}\rho_m^2 + \frac{l}{2}\sum_{m=1}^{n} W_m \kappa_{x,m} x_m^2 \tag{6.7}$$

in which p_ρ is the lateral soil resistance on pile; p_x is the pile side friction; ρ is the resultant lateral displacement; $\kappa_{\rho,m}$ and $\kappa_{x,m}$ are tangent values at the point of *p-y* and *t-z* curves when moving the lateral deflection ρ_m and vertical displacement x_m at the Gaussian integration point m, respectively; W_m is the weight coefficients; and, n is the number of Gauss integration points. In general, 5 integration points are enough for the analysis.

The external work done is given by:

$$V = -\sum_{i=1}^{12} F_i S_i \tag{6.8}$$

where F_i and S_i are the applied loads on the pile and the corresponding displacements along the load, respectively.

6.3.2 Tangent stiffness matrix

The minimum total potential energy principle is adopted to obtain the element tangent stiffness by second variations of the total potential energy equation. The tangent stiffness of structural element is given by:

$$[k_E]=[k_L]+[k_G]+[k_H] \tag{6.9}$$

where $[k_L]$ and $[k_G]$ are the linear and geometric stiffness matrices, respectively, which are given in Appendix I; and, $[k_H]$ is the plastic hinge matrix:

$$[k_H]=\left[\begin{array}{cccccccccccc}
0 & 0 & 0 & 0 & 0 & 0 & 0 & 0 & 0 & 0 & 0 & 0 \\
 & 0 & 0 & 0 & 0 & 0 & 0 & 0 & 0 & 0 & 0 & 0 \\
 & & 0 & 0 & 0 & 0 & 0 & 0 & 0 & 0 & 0 & 0 \\
 & & & 0 & 0 & 0 & 0 & 0 & 0 & 0 & 0 & 0 \\
 & & & & E_pI_yR_y & 0 & 0 & 0 & -E_pI_yR_y & 0 & 0 & 0 \\
 & & & & & E_pI_zR_z & 0 & 0 & 0 & -E_pI_zR_z & 0 & 0 \\
 & & & & & & 0 & 0 & 0 & 0 & 0 & 0 \\
 & & & & & & & 0 & 0 & 0 & 0 & 0 \\
 & & & & & & & & E_pI_yR_y & 0 & 0 & 0 \\
 & & & & & & & & & E_pI_zR_z & 0 & 0 \\
 & & & & & & & & & & 0 & 0 \\
SYM. & & & & & & & & & & & 0
\end{array}\right] \tag{6.10}$$

The maximum bending moment of a pile can be tracked at some distance below the ground. The pile begins to yield when the moment of pile section (M_h) exceeds its first-yield moment (M_y). The inelastic region will gradually spread with the increasing applied load until the pile section reaches its ultimate moment (M_u). In order to consider the gradual yielding behavior, the parameters of material plasticity R_y and R_z proposed by Chan and Chui [258] are used in this work and determined by:

$$R=\frac{6|M_u-M_h|}{|M_h-M_y|}, \quad M_y<M_h<M_u \tag{6.11}$$

where M_h is the moment at the plastic hinge; and, M_y and M_u are the first-yield moment and ultimate moment, respectively. The value of R is set to infinity (10^{10}) before yielding in this study. The dimension of $[k_H]$ is higher and incompatible with conventional analysis program. Therefore, a static condensation algorithm [253] is adopted to condense the plastic hinges' influencing matrix at the ends and mid-span into the conventional dimension. The element stiffness matrix [k_E] only consider the plastic hinges at and middle of an element, which are further incorporated into condensed matrix [k_U] by introducing parameters of material plasticity at element ends (R_y^b , R_z^b , R_y^t , and R_z^t). The detailed process and the condensed matrix [k_U] are provided in Appendix II.

The total tangent stiffness of an element is given by:

$$\left[k_T\right]=\left[\eta\right]\left[k_U\right]\left[\eta\right]^T+\left[\chi\right]+\left[k_S\right] \tag{6.12}$$

where [k_S] is the soil stiffness matrix with the consideration of lateral soil resistance and pile side friction; and, [η] and [χ] are transformed matrices. The matrices [k_S], [η], and [χ] are given in Appendix III. The element global stiffness matrix can be assembled by:

$$\left[K_T\right]=\sum_{i=1}^{NELE}\left(\left[\Psi\right]_i\left[k_T\right]\left[\Psi\right]_i^T\right) \tag{6.13}$$

in which *NELE* is the total number of elements; and, [Ψ]$_i$ is the local to global transformation matrix [250].

6.3.3 Nodal forces

The nodal forces can be obtained by the first variation of the potential energy equation. The nodal forces of an element are given by:

$$\begin{aligned}\{f\}&=\left[\eta\right]^T\{f_E\}+\{f_S\}\\&=\left\{F_{1x}\quad F_{1y}\quad F_{1z}\quad M_{1x}\quad M_{1y}\quad M_{1z}\quad F_{2x}\quad F_{2y}\quad F_{2z}\quad M_{2x}\quad M_{2y}\quad M_{2z}\right\}^T\end{aligned} \tag{6.14}$$

where {f_E} and {f_S} are the force vectors for structural element forces and the soil resistance force, respectively, which are given in Appendix IV; and, *F* and *M* are the force and moment along the corresponding coordinate axes, respectively. The vector of incremental element forces at the *s*th position is transformed to the global coordinate by:

$$\{\Delta R\}_s=\sum_{i=1}^{NELE}\left[\left[\Psi\right]_i^T\{f\}_i\right] \tag{6.15}$$

where *NELE* is the number of elements. The final element force vector is accumulated by the previous force vector at the (*s*-1)th position:

$$\{R\}_s = \{\Delta R\}_s + \{R\}_{s-1} \tag{6.16}$$

6.4 Numerical analysis procedure

A Python program has been developed, and the detailed procedure is summarized in Figure 6-3. The Updated Lagrangian description is employed for the large deformation FE analysis of the pile, whereby the tangent stiffness matrix is updated to incorporate the variations in geometrical properties. The Newton-Raphson iterative method [259] and the displacement control method [260] are employed to solve various nonlinear problems. The convergence criterion based on unbalanced forces $\{\Delta F\}$ and residual displacement $\{\Delta U\}$ is adopted in the iterative solution procedure. The iterative process is terminated once the acceptable tolerance (A_t) has been achieved, which is typically set to 0.001 in practice.

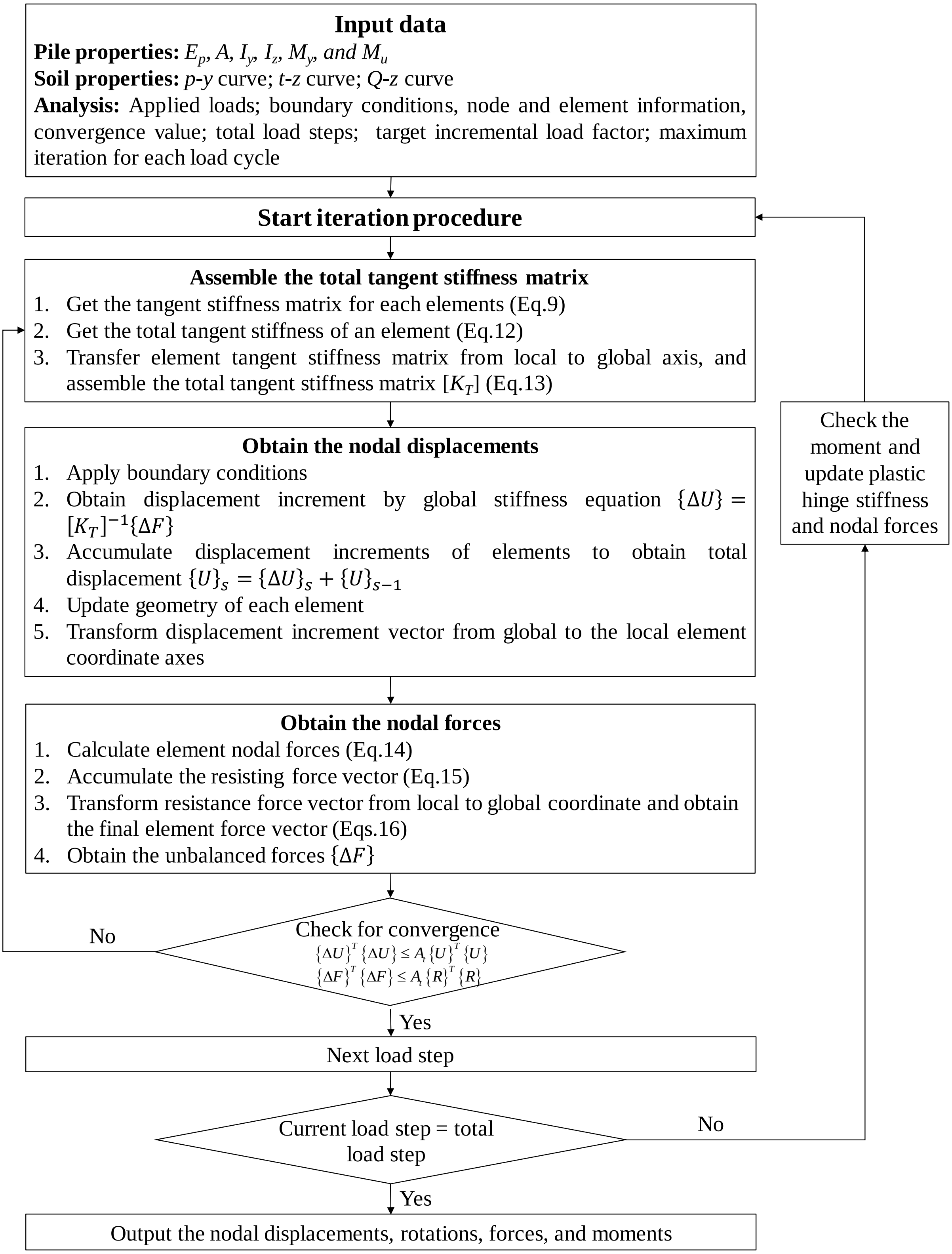

Figure 6-3 A flowchart of the numerical analysis procedure for the proposed method

6.5 Model validation

6.5.1 Compare with 3D FE method

This example performs a buckling analysis of initially bent columns to validate the accuracy of the element formulations, which was originally studied by Nadeem et al. [261] using 3D solid elements in the FE analysis. As shown in Figure 6-4, an initial imperfection described by a half-sine profile defines the initial node coordinates of the column. The material properties of pile are the following: column length (L_p) = 20 m; column diameter (D) = 1 m; E_p = 160 GPa; material yield strength (σ_y) = 200 MPa; M_y = 19635 kN·m; and, M_u = 33334 kN·m; and initial imperfection amplitudes (a_m) = 0.3 m and 0.1 m. Both column ends are pinned. The displacement control method is employed to trace the post-buckling configurations. The load-deflection behavior of the initially bent column is investigated by the proposed method with 10 elements and the FE method with 320 solid elements calculated by Nadeem et al. [261], which have been presented in Figure 6-5. The normalized value (P/P_E) versus mid-height deflection (X_m) curves show that the proposed method can produce accurate results using only 10 elements in the inelastic analysis. It indicates that the internal plastic hinges within the element can accurately predict the member's inelastic behavior. Due to the condensation of internal degrees of freedom of the proposed element, the size of the global stiffness matrix can be significantly reduced, which improves the numerical efficiency. On the other hand, it can be seen that the elastic analysis predicts higher critical buckling loads than the inelastic analysis, which may lead to an unsafe design due to the elastic assumption of pile material.

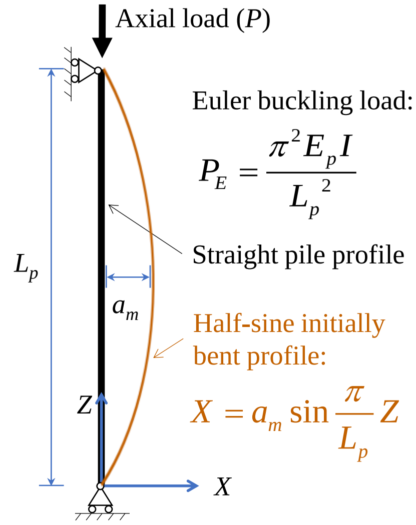

Figure 6-4 The initially bent column under axial load

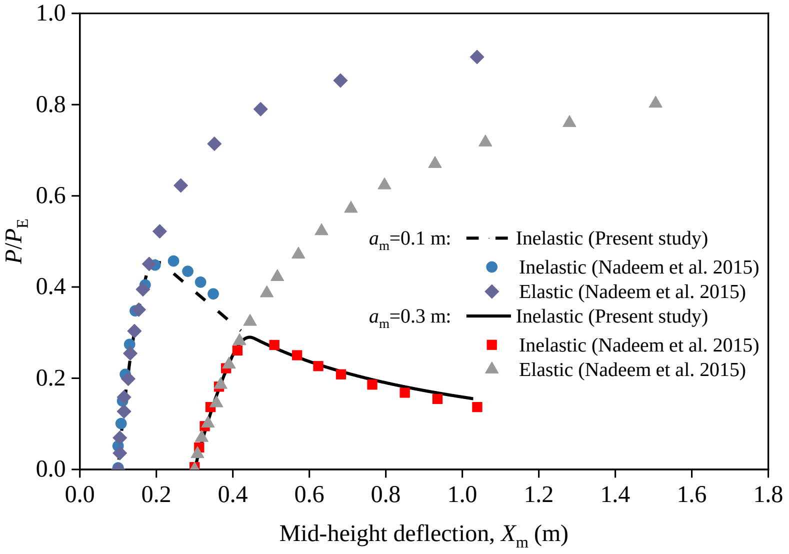

Figure 6-5 Load versus mid-height deflection curves of initially bent columns

6.5.2 Compare with field load test and EPE model on prestressed concrete pile

Pando [262] performed field tests on a laterally loaded prestressed concrete pile in two-layered sandy soils (Figure 6-6). The properties of the pile are: L_p = 18 m; width of square pile (D_w) = 0.61 m; axial stiffness (E_pA) = 8.2×10^6 kN; M_y = 352 kN·m; and, M_u = 595 kN·m. The pile head is free, and vertical direction of pile toe is fixed. The locations of the original ground surface, applied load, and bottom of pit are 1.24 m, 1.34 m, and 2.03 m below the pile head, respectively. The soils surrounding the pile are loose and medium dense sands, with corresponding thicknesses of 10 and 6.78 m. Almost all of the soil is submerged. The same soil parameters suggested by Pando [262], as presented in Figure 6-6, are employed in the present analysis, such as the soil depth (H_s), unit weight of soil (γ'), friction angle (φ), and initial *p-y* modulus (E_{py}). The *p-y* curves (Figure 6-7) for sandy soil are adopted from Reese et al. [263]. The pile head is free, and the pile toe is fixed. The EPE model is also employed as a comparison with the proposed method, both with 12 elements to simulate the pile-soil system. As shown in Figure 6-8&Figure 6-9, the predicted values of lateral deflection and pile head rotation at the ground surface show reasonably good agreement with the field measurements, verifying the accuracy of the proposed element in capturing the inelastic behavior of the pile. In addition, it can be seen that the proposed method is consistent with the results of the EPE model in the elastic state, but there is a large difference in the elastic-plastic state, mainly due to the elastic assumption of the EPE model. It has been demonstrated in reference [250] that the saving in the overall computational time and data input manipulation is considerable in the EPE model. The proposed method considers the the material-yielding through zero-length plastic hinges on the basis of the EPE model. The additional time required for the procedure to deal with the zero-length plastic hinges is minimal when compared with the total computational time [258]. Therefore, the proposed model has the similar efficiency as the EPE model in each iterative procedure and is capable of modelling the inelastic behavior of the pile with higher accuracy.

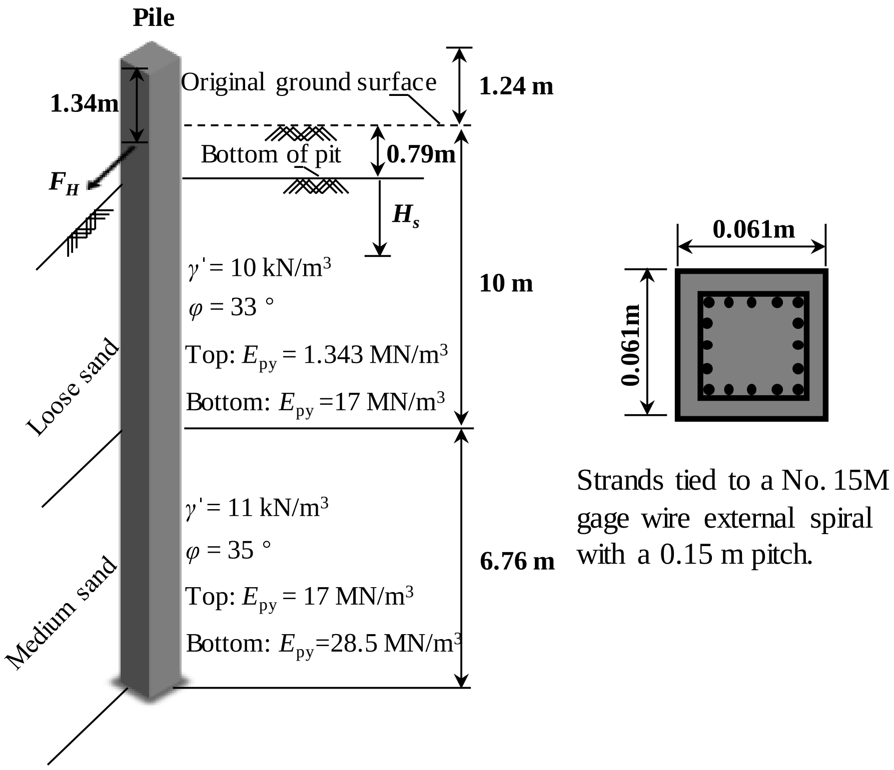

Figure 6-6 A schematic diagram of the prestressed concrete pile under lateral loads in multilayer soils in sandy soils

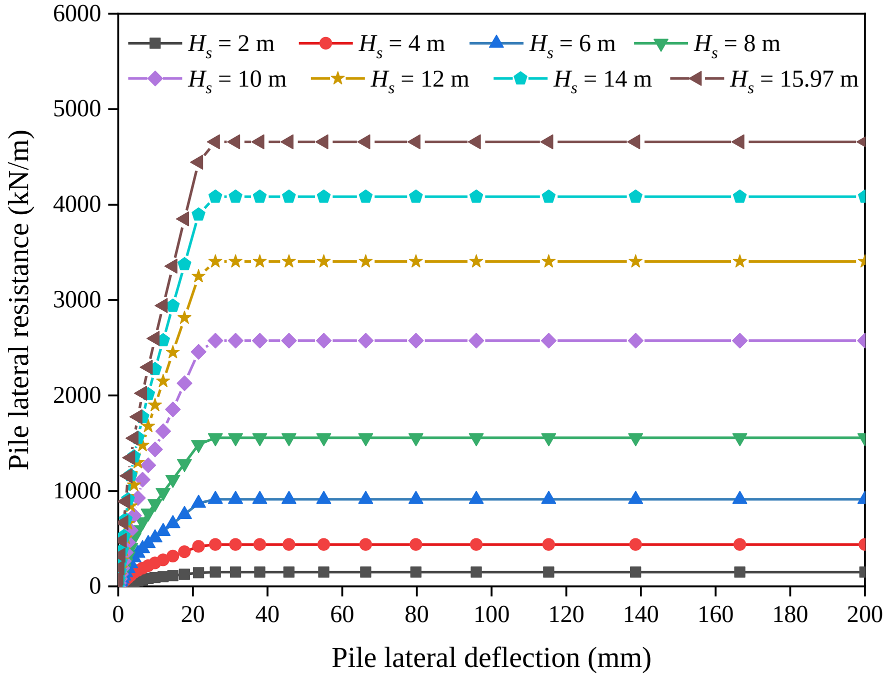

Figure 6-7 *p-y* curves for the sandy soils

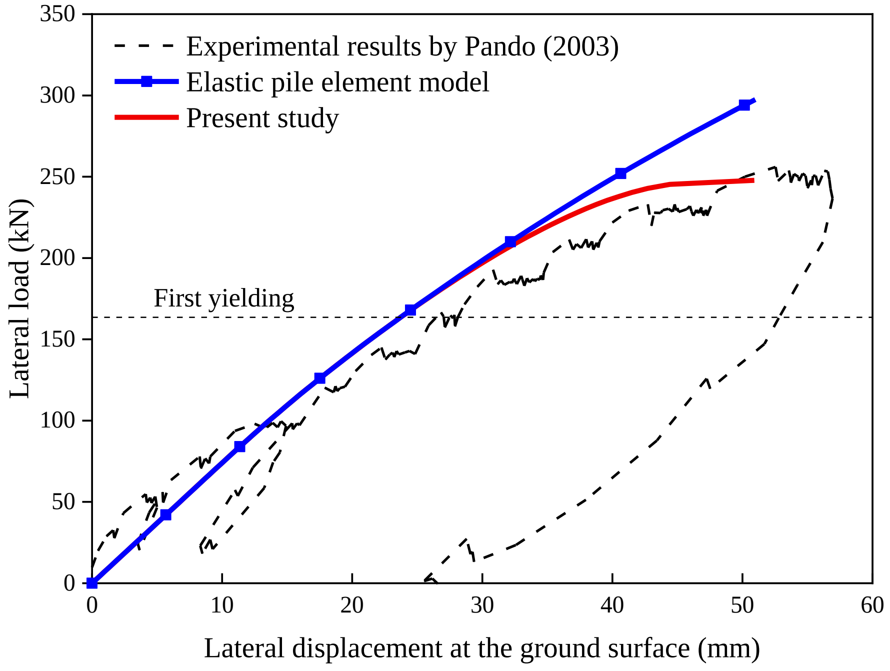

Figure 6-8 The load-deflection curve for the prestressed concrete pile

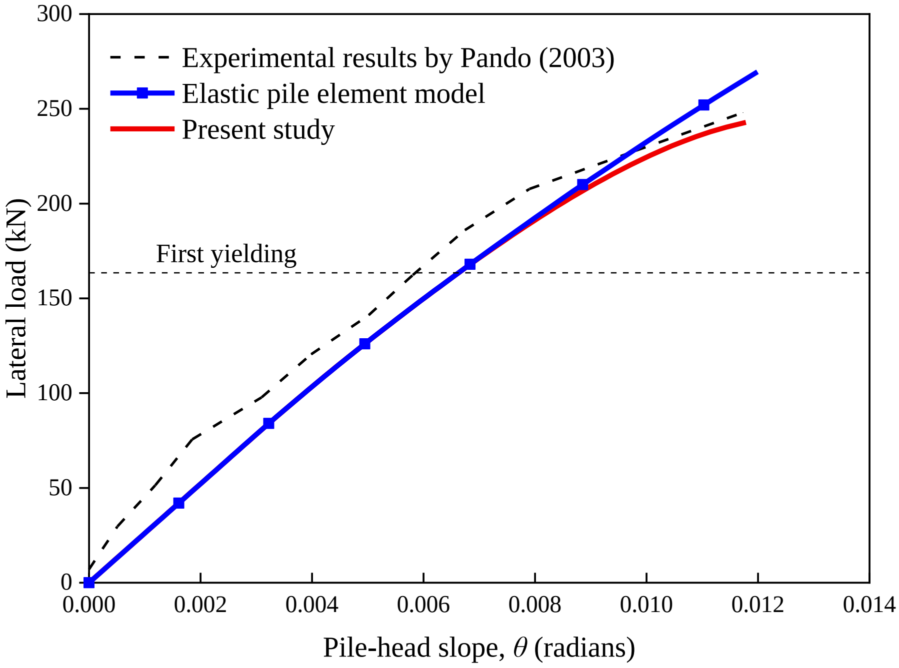

Figure 6-9 The load-slope curve for the prestressed concrete pile

6.5.3 Compare with field load test on steel pipe pile in multi-layer soil

A series of lateral load tests on steel pipe piles were performed by Snyder [264]. The pile has an embedment depth of 11.6 m, with 2.1 m protruding above ground. The pile parameters reported by Snyder [264] and El Naggar [221] are as following: L_p = 13.7 m; outer diameter (D_0) = 0.324 m; wall thickness (t_w) = 9.5 mm; Young's modulus (E_p) = 200 GPa; M_y = 358 kN·m; and, M_u = 424 kN·m. The lateral load was applied at 495 mm above the ground line. The soil profile consisted of layers of soft to medium clay underlain by interbedded layers of sand and fine-grained soils. The soil properties were determined from field and laboratory tests. The same model parameters suggested by Snyder [264], as presented in Figure 6-10, are employed in the present analysis. The unmodified *p-y* curves (Figure 6-11) in sand and clay are respectively adopted from Reese et al. [263, 265] by using the input soil parameters such as soil depth (H_s), unit weight of soil (γ'), friction angle (φ), undrained shear strength (S_u), soil strain at the 50% stress level (ε_{50}), and initial *p-y* modulus (E_{py}). The pile head is free, and the pile toe is fixed. As shown in Figure 6-12 to Figure 6-14, the load-displacement response and the relationship between bending moment and depth are well predicted by the proposed method in comparison with the experiment and LPILE calculation [264]. Since the experimental data and LPILE calculation are recorded only until the pile begins to yield, the load-displacement response after the pile yielding will be compared with the conventional model based on discrete spring elements reported by El Nagger [221]. It can be seen that the load-displacement curve predicted by the proposed method coincides well with the simulation results of the discrete spring elements model, indicating the accuracy of the proposed model. In addition, in terms of modelling of the nonlinear pile-soil interaction, the proposed method based on the EPE model increases the efficiency of the numerical analysis of the pile-soil system compared with the conventional model. This allows the proposed method to be better applied to pile-soil systems for the analysis of large structures that consist of hundreds of piles. As shown in Figure 6-14, the proposed method predicts the first-yielding of the pile occurs at H_s = 3.1 m with the pile head deflection of 143 mm, which is close to El Nagger's prediction of H_s = 3.24 m with the pile head deflection of 154 mm [221].

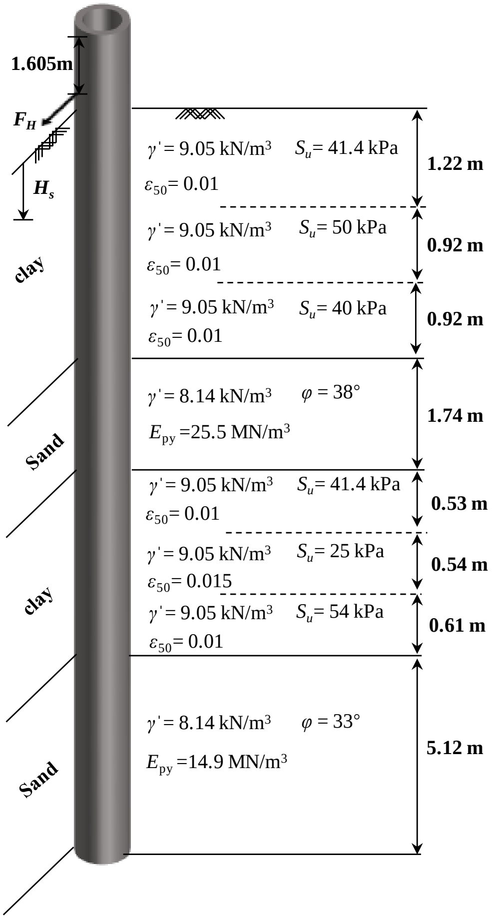

Figure 6-10 A schematic diagram of the steel pipe pile under lateral loads in multi-layer soil

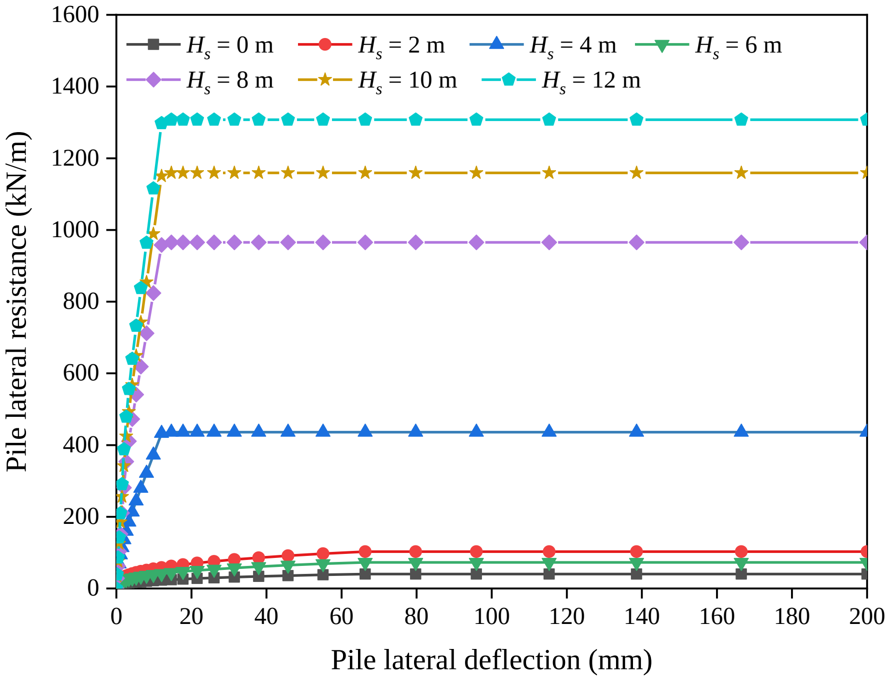

Figure 6-11 *p-y* curves for multi-layer soil

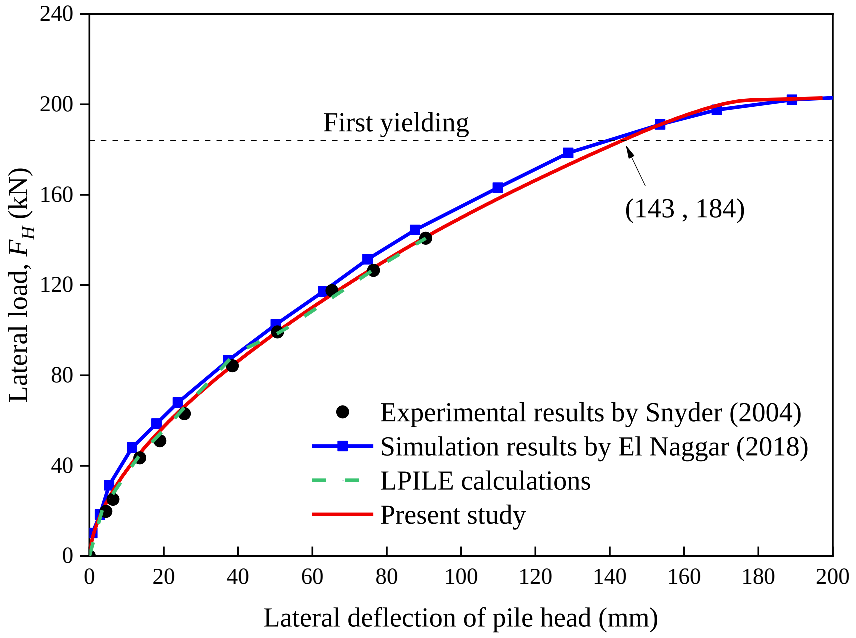

Figure 6-12 Comparison of measured lateral load versus displacement curves

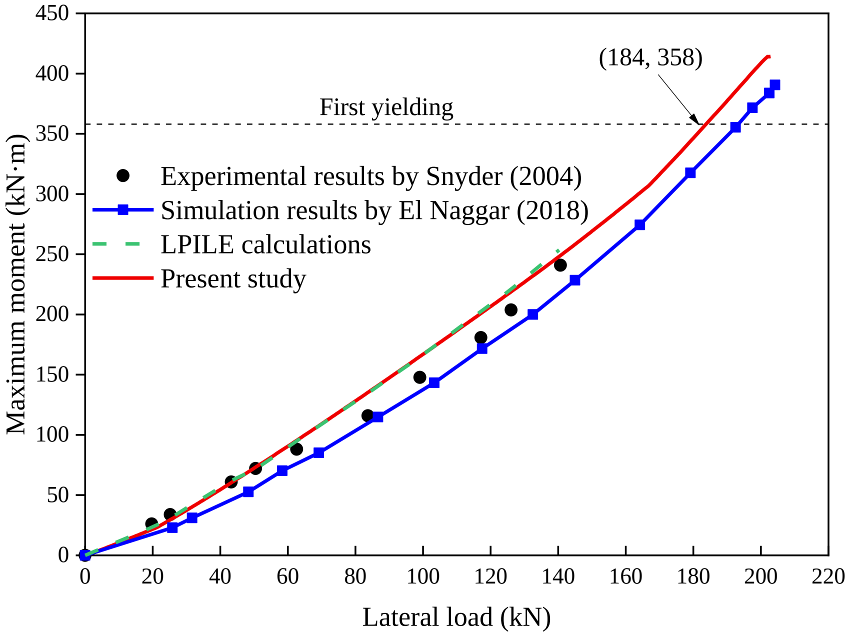

Figure 6-13 Comparison of measured maximum moment versus load curves

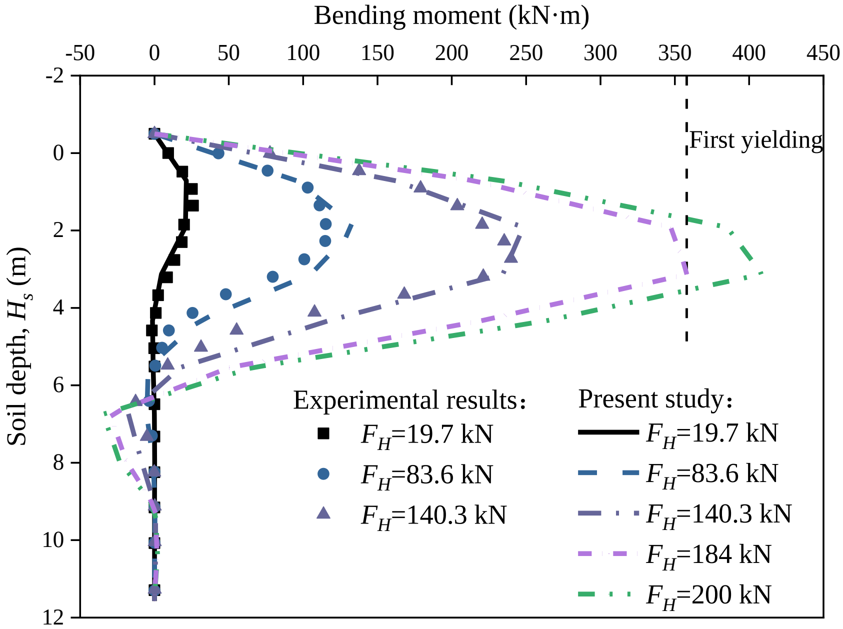

Figure 6-14 Bending moment versus depth for the different lateral loads

6.5.4 Compare with field load test on vertically loaded pile

In this example, a practical case is conducted to validate the performance of the pile-soil integrated element for simulating the friction pile that is free at the pile toe. Zhang et al. [266] reported a field test on a single bored pile embedded in multi-layered soil to study the load-settlement response. The pile-soil interactions of both the pile shaft and the pile toe (*t-z* and *Q-z* curves) are considered to calculate the total settlement. The pile parameters are as following: L_p = 47.7 m; D = 1.1 m; and, E_p = 30 GPa. The vertical load is applied on the pile head. The soil condition is shown in Figure 6-15, and the load-displacement relationships developed at the pile shaft and pile toe are given. The values of the parameters τ_u, a, b and S_u are determined by Zhang et al. [266] and presented in Table 1. As shown in Figure 6-16, the predictions by the proposed method are generally in good agreement with the field load test.

Table 6-1 Soil parameters [266]

Layer	Soil depth	τ_u (kPa)	$a \times 10^{-5}$ (m^3/kN)	$b \times 10^{-3}$ (m^2/kN)	S_u (mm)
1	1.3	6.06	5.5	110	1.0
2	1.9	11.8	4.8	37	1.0
	10.3	19.6	4.5	19	1.4
3	21.0	18.5	4.0	14	1.0
	25	53.7	2.0	5.3	1.5
4	34.6	61.0	1.2	4.4	1.0
5	38.7	29.9	2.9	4.4	1.0
6	40.5	34.6	2.5	6.2	1.
7	42.5	50.2	1.1	7.7	0.9
8	44.5	61.0	1.2	4.4	1.0
9	50.5	83.6	1.1	4.1	1.4
			$k_1 = 1.4\times10^6$ (kPa/m)	$k_2 = 3.3\times10^5$ (kPa/m)	$S_b = 1.4$ (mm)

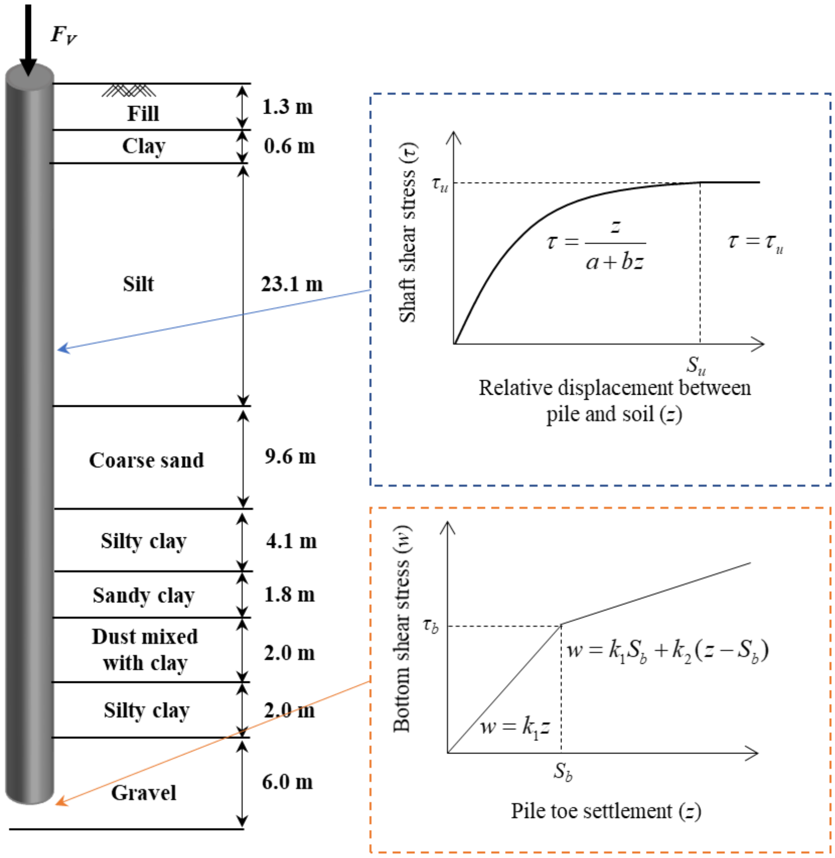

Figure 6-15 A schematic diagram of the steel pipe pile under lateral loads in multi-layer soil

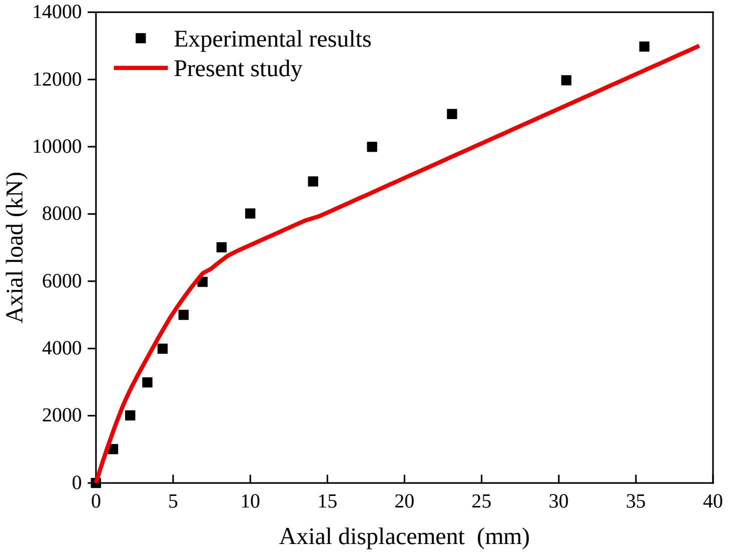

Figure 6-16 Comparison between the predicted and measured load-settlement behavior for a single pile in multilayered soils.

6.6 Conclusions

This work proposes a pile-soil integrated element to effectively and accurately simulate pile behaviour considering material and soil nonlinearity. The newly developed element stiffness matrices and nodal forces are employed for the numerical implementation of the pile-soil integrated element based on EPE. To account for material inelasticity, the internal plastic hinges located at the two ends and middle of the element have been incorporated into the element stiffness matrix using the static condensation algorithm. The nonlinear pile-soil interactions are efficiently evaluated according to Gauss-Legendre method for the summation processes of total potential energy equations and soil resistance at the Gauss integration points. The following conclusions can be drawn:

(1) The plastic hinges at the ends and middle of an element are directly integrated into the element formulations to capture the inelastic behaviour of a pile. The buckling behaviour predicted by the proposed method with 10 elements is in good agreement with the sophisticated FE method with 320 solid elements, indicating the accuracy of the element formulations and the contribution of three plastic hinges.

(2) The proposed method is compared with the EPE model using the same number of elements conducted on partially embedded piles in sandy soil. It demonstrates a better accuracy of the proposed method compared to the EPE model at a larger displacement level. It implies that the proposed method has the similar efficiency as the EPE model in each iterative procedure. The proposed method successfully accounts for the effects of pile inelasticity and soil nonlinearity in the analysis and allows for the development of plastic hinges along the pile, addressing the shortcomings of the EPE model.

(3) The proposed method is validated by comparing it with the field load tests. The predictions calculated by the proposed method are close to the actual measured results for the laterally and axially loaded piles in multi-layer soil. Unlike the conventional discrete spring elements model using beam elements and spring elements, the proposed method uses one element type that integrated both pile and soil to eliminate tedious modelling process. By providing convenience and efficiency in computing and modelling the pile-soil system under heavy loading conditions, the proposed method can be effectively utilized for the analysis and design of large structures with hundreds of piles.

Appendix I – Linear and geometric stiffness matrices

The linear stiffness matrix is given by:

$$[k_L]=\begin{bmatrix} k_{1,1}^L & 0 & 0 & 0 & 0 & 0 & 0 & 0 & 0 & 0 & 0 & 0 \\ & k_{2,2}^L & 0 & 0 & k_{2,5}^L & 0 & k_{2,7}^L & 0 & 0 & 0 & 0 & 0 \\ & & k_{3,3}^L & 0 & 0 & k_{3,6}^L & 0 & k_{3,8}^L & 0 & 0 & 0 & 0 \\ & & & k_{4,4}^L & 0 & 0 & 0 & 0 & 0 & 0 & 0 & 0 \\ & & & & k_{5,5}^L & 0 & k_{5,7}^L & 0 & 0 & 0 & 0 & 0 \\ & & & & & k_{6,6}^L & 0 & k_{6,8}^L & 0 & 0 & 0 & 0 \\ & & & & & & k_{7,7}^L & 0 & k_{7,9}^L & 0 & k_{7,11}^L & 0 \\ & & & & & & & k_{8,8}^L & 0 & k_{8,10}^L & 0 & k_{8,12}^L \\ & & & & & & & & k_{9,9}^L & 0 & k_{9,11}^L & 0 \\ & & & & & & & & & k_{10,10}^L & 0 & k_{10,12}^L \\ & & & & & & & & & & k_{11,11}^L & 0 \\ SYM. & & & & & & & & & & & k_{12,12}^L \end{bmatrix} \tag{6.17}$$

where

$$\begin{gathered} k_{1,1}^L=\frac{E_pA}{L}\ ,\quad k_{2,2}^L=k_{5,5}^L=k_{9,9}^L=k_{11,11}^L=\frac{8E_pI_y}{L},\quad k_{3,3}^L=k_{6,6}^L=k_{10,10}^L=k_{12,12}^L=\frac{8E_pI_z}{L} \\ k_{2,5}^L=k_{9,11}^L=\frac{4E_pI_y}{L}\ ,\ k_{2,7}^L=k_{5,7}^L=-k_{7,9}^L=-k_{7,11}^L=-\frac{24E_pI_y}{L^2}\ ,\ k_{3,6}^L=k_{10,12}^L=\frac{4E_pI_z}{L} \\ k_{3,8}^L=k_{6,8}^L=-k_{8,10}^L=-k_{8,12}^L=-\frac{24E_pI_z}{L^2},\ k_{4,4}^L=\frac{GJ}{L}\ ,\ k_{7,7}^L=\frac{192E_pI_y}{L^3}\ ,\ k_{8,8}^L=\frac{192E_pI_z}{L^3} \end{gathered} \tag{6.18}$$

The corresponding nodal deformations of an element is given by:

$$\{u\}=\{s_x,\quad \theta_{1y},\quad \theta_{1z},\quad \theta_x,\quad \theta_{h1y},\quad \theta_{h1z},\quad u_z,\quad u_y,\quad \theta_{h2y},\quad \theta_{h2z},\quad \theta_{2y},\quad \theta_{2z}\}^T \tag{6.19}$$

The geometric stiffness matrix is given by:

$$
[k_G]=\begin{bmatrix}
0 & k_{1,2}^G & k_{1,3}^G & 0 & k_{1,5}^G & k_{1,6}^G & k_{1,7}^G & k_{1,8}^G & k_{1,9}^G & k_{1,10}^G & k_{1,11}^G & k_{1,12}^G \\
 & k_{2,2}^G & k_{2,3}^G & 0 & k_{2,5}^G & k_{2,6}^G & k_{2,7}^G & k_{2,8}^G & k_{2,9}^G & k_{2,10}^G & k_{2,11}^G & k_{2,12}^G \\
 & & k_{3,3}^G & 0 & k_{3,5}^G & k_{3,6}^G & k_{3,7}^G & k_{3,8}^G & k_{3,9}^G & k_{3,10}^G & k_{3,11}^G & k_{3,12}^G \\
 & & & 0 & 0 & 0 & 0 & 0 & 0 & 0 & 0 & 0 \\
 & & & & k_{5,5}^G & k_{5,6}^G & k_{5,7}^G & k_{5,8}^G & k_{5,9}^G & k_{5,10}^G & k_{5,11}^G & k_{5,12}^G \\
 & & & & & k_{6,6}^G & k_{6,7}^G & k_{6,8}^G & k_{6,9}^G & k_{6,10}^G & k_{6,11}^G & k_{6,12}^G \\
 & & & & & & k_{7,7}^G & k_{7,8}^G & k_{7,9}^G & k_{7,10}^G & k_{7,11}^G & k_{7,12}^G \\
 & & & & & & & k_{8,8}^G & k_{8,9}^G & k_{8,10}^G & k_{8,11}^G & k_{8,12}^G \\
 & & & & & & & & k_{9,9}^G & k_{9,10}^G & k_{9,11}^G & k_{9,12}^G \\
 & & & & & & & & & k_{10,10}^G & k_{10,11}^G & k_{10,12}^G \\
 & & & & & & & & & & k_{11,11}^G & k_{11,12}^G \\
SYM. & & & & & & & & & & & k_{12,12}^G
\end{bmatrix} \tag{6.20}
$$

where

$$
\begin{aligned}
&k_{1,2}^G=-\frac{E_pAu_z}{10l}+\frac{E_pA\theta_{1y}}{15}-\frac{E_pA\theta_{h1y}}{60},\quad k_{1,3}^G=-\frac{E_pAu_y}{10l}+\frac{E_pA\theta_{1z}}{15}-\frac{E_pA\theta_{h1z}}{60}\\
&k_{1,5}^G=-\frac{E_pAu_z}{10l}-\frac{E_pA\theta_{1y}}{60}+\frac{E_pA\theta_{h1y}}{15},\quad k_{1,6}^G=-\frac{E_pAu_y}{10l}-\frac{E_pA\theta_{1z}}{60}+\frac{E_pA\theta_{h1z}}{15}\\
&k_{1,7}^G=\frac{24E_pAu_z}{5l^2}-\frac{E_pA\theta_{1y}}{10l}+\frac{E_pA\theta_{2y}}{10l}-\frac{E_pA\theta_{h1y}}{10l}+\frac{E_pA\theta_{h2y}}{10l}\\
&k_{1,8}^G=\frac{24E_pAu_y}{5l^2}-\frac{E_pA\theta_{1z}}{10l}+\frac{E_pA\theta_{2z}}{10l}-\frac{E_pA\theta_{h1z}}{10l}+\frac{E_pA\theta_{h2z}}{10l}\\
&k_{1,9}^G=\frac{E_pAu_z}{10l}-\frac{E_pA\theta_{2y}}{60}+\frac{E_pA\theta_{h2y}}{15},\quad k_{1,10}^G=\frac{E_pAu_y}{10l}-\frac{E_pA\theta_{2z}}{60}+\frac{E_pA\theta_{h2z}}{15}\\
&k_{1,11}^G=\frac{E_pAu_z}{10l}+\frac{E_pA\theta_{2y}}{15}-\frac{E_pA\theta_{h2y}}{60},\quad k_{1,12}^G=\frac{E_pAu_y}{10l}+\frac{E_pA\theta_{2z}}{15}-\frac{E_pA\theta_{h2z}}{60}\\
&k_{2,2}^G=\frac{F_{ex}l}{15}+\frac{E_pA\left(6u_z+l\left(-4\theta_{1y}+\theta_{h1y}\right)\right)^2}{3600l}\\
&k_{2,3}^G=\frac{E_pA\left(6u_z+l\left(-4\theta_{1y}+\theta_{h1y}\right)\right)\left(6u_y+l\left(-4\theta_{1z}+\theta_{h1z}\right)\right)}{3600l}\\
&k_{2,5}^G=-\frac{F_{ex}l}{60}+\frac{E_pA\left(6u_z+l\left(\theta_{1y}-4\theta_{h1y}\right)\right)\left(6u_z+l\left(-4\theta_{1y}+\theta_{h1y}\right)\right)}{3600l}
\end{aligned} \tag{6.21}
$$

$$k_{2,6}^{G}=\frac{E_pA\left(6u_z+l\left(-4\theta_{1y}+\theta_{h1y}\right)\right)\left(6u_y+l\left(\theta_{1z}-4\theta_{h1z}\right)\right)}{3600l}$$

$$k_{2,7}^{G}=-\frac{F_{ex}}{10}-\frac{E_pA\left(6u_z+l\left(-4\theta_{1y}+\theta_{h1y}\right)\right)\left(48u_z+l\left(-\theta_{1y}+\theta_{2y}-\theta_{h1y}+\theta_{h2y}\right)\right)}{600l^2}$$

$$k_{2,8}^{G}=\frac{E_pA\left(6u_z+l\left(-4\theta_{1y}+\theta_{h1y}\right)\right)\left(-48u_y+l\left(\theta_{1z}-\theta_{2z}+\theta_{h1z}-\theta_{h2z}\right)\right)}{600l^2}$$

$$k_{2,9}^{G}=-\frac{E_pA\left(6u_z+L\left(-4\theta_{1y}+\theta h_{1y}\right)\right)\left(6u_z-L\theta_{2y}+4L\theta_{h2y}\right)}{3600l}$$

$$k_{2,10}^{G}=\frac{E_pA\left(6u_z+l\left(-4\theta_{1y}+\theta_{h1y}\right)\right)\left(-6u_y+l\left(\theta_{2z}-4\theta_{h2z}\right)\right)}{3600l}$$

$$k_{2,11}^{G}=-\frac{E_pA\left(6u_z+l\left(-4\theta_{1y}+\theta_{h1y}\right)\right)\left(6u_z+4l\theta_{2y}-l\theta_{h2y}\right)}{3600l}$$

$$k_{2,12}^{G}=-\frac{E_pA\left(6u_z+l\left(-4\theta_{1y}+\theta_{h1y}\right)\right)\left(6u_y+4l\theta_{2z}-l\theta_{h2z}\right)}{3600l}$$

$$k_{3,3}^{G}=\frac{F_{ex}l}{15}+\frac{E_pA\left(6u_y+l\left(-4\theta_{1z}+\theta_{h1z}\right)\right)^2}{3600l}$$

$$k_{3,5}^{G}=-\frac{E_pA\left(6u_z+l\left(\theta_{1y}-4\theta_{h1y}\right)\right)\left(-6u_y+4l\theta_{1z}-l\theta_{h1z}\right)}{3600l}$$

$$k_{3,6}^{G}=-\frac{F_{ex}l}{60}+\frac{E_pA\left(6u_y+l\left(\theta_{1z}-4\theta_{h1z}\right)\right)\left(6u_y+l\left(-4\theta_{1z}+\theta h_{1z}\right)\right)}{3600l}$$

$$k_{3,7}^{G}=\frac{E_pA\left(6u_y+l\left(-4\theta_{1z}+\theta_{h1z}\right)\right)\left(-48u_z+l\left(\theta_{1y}-\theta_{2y}+\theta_{h1y}-\theta_{h2y}\right)\right)}{600L^2}$$

$$k_{3,8}^{G}=-\frac{F_{ex}}{10}-\frac{E_pA\left(6u_y+l\left(-4\theta_{1z}+\theta_{h1z}\right)\right)\left(48u_y+l\left(-\theta_{1z}+\theta_{2z}-\theta_{h1z}+\theta_{h2z}\right)\right)}{600l^2}$$

$$k_{3,9}^{G}=\frac{E_pA\left(6u_y+l\left(-4\theta_{1z}+\theta_{h1z}\right)\right)\left(-6u_z+l\left(\theta_{2y}-4\theta_{h2y}\right)\right)}{3600l}$$

$$k_{3,10}^{G}=-\frac{E_pA\left(6u_y+l\left(-4\theta_{1z}+\theta_{h1z}\right)\right)\left(6u_y-l\theta_{2z}+4l\theta_{h2z}\right)}{3600l}$$

$$k_{3,11}^{G}=-\frac{E_pA\left(6u_y+l\left(-4\theta_{1z}+\theta_{h1z}\right)\right)\left(6u_z+4l\theta_{2y}-l\theta_{h2y}\right)}{3600l}$$

$$k_{3,12}^{G}=-\frac{E_pA\left(6u_y+l\left(-4\theta_{1z}+\theta_{h1z}\right)\right)\left(6u_y+4l\theta_{2z}-l\theta_{h2z}\right)}{3600l}$$

$$k_{5,5}^{G}=\frac{F_{ex}l}{15}+\frac{E_pA\left(6u_z+l\left(\theta_{1y}-4\theta_{h1y}\right)\right)^2}{3600l},\quad k_{6,6}^{G}=\frac{F_{ex}l}{15}+\frac{E_pA\left(6u_y+l\left(\theta_{1z}-4\theta_{h1z}\right)\right)^2}{3600l}$$

$$k_{5,6}^{G}=\frac{E_pA\left(6u_z+l\left(\theta_{1y}-4\theta_{h1y}\right)\right)\left(6u_y+l\left(\theta_{1z}-4\theta_{h1z}\right)\right)}{3600l}$$

$$k_{5,7}^{G}=-\frac{F_{ex}}{10}+\frac{E_pA\left(6u_z+l\left(\theta_{1y}-4\theta_{h1y}\right)\right)\left(-48u_z+l\left(\theta_{1y}-\theta_{2y}+\theta_{h1y}-\theta_{h2y}\right)\right)}{600l^2}$$

$$k_{5,8}^{G}=\frac{E_pA\left(6u_z+l\left(\theta_{1y}-4\theta_{h1y}\right)\right)\left(-48u_y+l\left(\theta_{1z}-\theta_{2z}+\theta_{h1z}-\theta_{h2z}\right)\right)}{600l^2}$$

$$k_{5,9}^{G}=\frac{E_pA\left(6u_z+l\left(\theta_{1y}-4\theta_{h1y}\right)\right)\left(-6u_z+l\left(\theta_{2y}-4\theta_{h2y}\right)\right)}{3600l}$$

$$k_{5,10}^{G}=\frac{E_pA\left(6u_z+l\left(\theta_{1y}-4\theta h_{1y}\right)\right)\left(-6u_y+l\left(\theta_{2z}-4\theta_{h2z}\right)\right)}{3600l}$$

$$k_{5,11}^{G}=-\frac{E_pA\left(6u_z+l\left(\theta_{1y}-4\theta h_{1y}\right)\right)\left(6u_z+4l\theta_{2y}-l\theta_{h2y}\right)}{3600l}$$

$$k_{5,12}^{G}=-\frac{E_pA\left(6u_z+l\left(\theta_{1y}-4\theta_{h1y}\right)\right)\left(6u_y+4l\theta_{2z}-l\theta_{h2z}\right)}{3600l}$$

$$k_{6,7}^{G}=\frac{E_pA\left(6u_y+l\left(\theta_{1z}-4\theta_{h1z}\right)\right)\left(-48u_z+l\left(\theta_{1y}-\theta_{2y}+\theta_{h1y}-\theta_{h2y}\right)\right)}{600l^2}$$

$$k_{6,8}^{G}=-\frac{F_{ex}}{10}+\frac{E_pA\left(6u_y+l\left(\theta_{1z}-4\theta_{h1z}\right)\right)\left(-48u_y+l\left(\theta_{1z}-\theta_{2z}+\theta_{h1z}-\theta_{h2z}\right)\right)}{600l^2}$$

$$k_{6,9}^{G}=\frac{E_pA\left(6u_y+l\left(\theta_{1z}-4\theta_{h1z}\right)\right)\left(-6u_z+l\left(\theta_{2y}-4\theta_{h2y}\right)\right)}{3600l}$$

$$k_{6,10}^{G}=\frac{E_pA\left(6u_y+l\left(\theta_{1z}-4\theta_{h1z}\right)\right)\left(-6u_y+l\left(\theta_{2z}-4\theta_{h2z}\right)\right)}{3600l}$$

$$k_{6,11}^{G}=-\frac{E_pA\left(6u_y+l\left(\theta_{1z}-4\theta_{h1z}\right)\right)\left(6u_z+4l\theta_{2y}-l\theta_{h2y}\right)}{3600l}$$

$$k_{6,12}^{G}=-\frac{E_pA\left(6u_y+l\left(\theta_{1z}-4\theta_{h1z}\right)\right)\left(6u_y+4l_{\theta 2z}-l\theta_{h2z}\right)}{3600l}$$

$$k_{7,7}^{G}=\frac{24F_{ex}}{5L}+\frac{E_pA\left(48u_z+l\left(-\theta_{1y}+\theta_{2y}-\theta_{h1y}+\theta_{h2y}\right)\right)^2}{100l^3}$$

$$k_{7,8}^{G}=\frac{E_pA\left(-48u_z+l\left(\theta_{1y}-\theta_{2y}+\theta_{h1y}-\theta_{h2y}\right)\right)\left(-48u_y+l\left(\theta_{1z}-\theta_{2z}+\theta_{h1z}-\theta_{h2z}\right)\right)}{100l^3}$$

$$k_{7,9}^{G}=\frac{F_{ex}}{10}+\frac{E_pA\left(6u_z-l\theta_{2y}+4l\theta_{h2y}\right)\left(48u_z+l\left(-\theta_{1y}+\theta_{2y}-\theta_{h1y}+\theta_{h2y}\right)\right)}{600l^2}$$

$$k_{7,10}^{G}=\frac{E_pA\left(-48u_z+l\left(\theta_{1y}-\theta_{2y}+\theta_{h1y}-\theta_{h2y}\right)\right)\left(-6u_y+l\left(\theta_{2z}-4\theta_{h2z}\right)\right)}{600l^2}$$

$$k_{7,11}^{G}=\frac{F_{ex}}{10}+\frac{E_pA\left(6u_z+4l\theta_{2y}-L\theta_{h2y}\right)\left(48u_z+l\left(-\theta_{1y}+\theta_{2y}-\theta_{h1y}+\theta_{h2y}\right)\right)}{600l^2}$$

$$k_{7,12}^{G}=\frac{E_pA\left(48u_z+l\left(-\theta_{1y}+\theta_{2y}-\theta_{h1y}+\theta_{h2y}\right)\right)\left(6u_y+4l\theta_{2z}-l\theta_{h2z}\right)}{600l^2}$$

$$k_{8,8}^{G}=\frac{24F_{ex}}{5l}+\frac{E_pA\left(48u_y+l\left(-\theta_{1z}+\theta_{2z}-\theta_{h1z}+\theta_{h2z}\right)\right)^2}{100l^3}$$

$$k_{8,9}^{G}=\frac{E_pA\left(-6u_z+l\left(\theta_{2y}-4\theta_{h2y}\right)\right)\left(-48u_y+l\left(\theta_{1z}-\theta_{2z}+\theta_{h1z}-\theta_{h2z}\right)\right)}{600l^2}$$

$$k_{8,10}^{G}=\frac{F_{ex}}{10}+\frac{E_pA\left(6u_y-l\theta_{2z}+4L\theta_{h2z}\right)\left(48u_y+l\left(-\theta_{1z}+\theta_{2z}-\theta_{h1z}+\theta_{h2z}\right)\right)}{600l^2}$$

$$k_{8,11}^{G}=-\frac{E_pA\left(6u_z+4l\theta_{2y}-l\theta_{h2y}\right)\left(-48u_y+l\left(\theta_{1z}-\theta_{2z}+\theta_{h1z}-\theta_{h2z}\right)\right)}{600l^2}$$

$$k_{8,12}^{G}=\frac{F_{ex}}{10}+\frac{E_pA\left(6u_y+4l\theta_{2z}-l\theta_{h2z}\right)\left(48u_y+l\left(-\theta_{1z}+\theta_{2z}-\theta_{h1z}+\theta_{h2z}\right)\right)}{600l^2}$$

$$k_{9,9}^{G}=\frac{F_{ex}l}{15}+\frac{E_pA\left(6u_z-l\theta_{2y}+4l\theta_{h2y}\right)^2}{3600l},\quad k_{10,10}^{G}=\frac{F_{ex}l}{15}+\frac{E_pA\left(6u_y+4l\theta_{hz2}-l\theta_{z2}\right)^2}{3600l}$$

$$k_{9,10}^{G} = \frac{E_p A\left(-6u_z + l\left(\theta_{2y} - 4\theta_{h2y}\right)\right)\left(-6u_y + l\left(\theta_{2z} - 4\theta_{h2z}\right)\right)}{3600l}$$

$$k_{9,11}^{G} = -\frac{F_{ex}l}{60} + \frac{E_p A\left(6u_z + 4l\theta_{2y} - l\theta_{h2y}\right)\left(6u_z - l\theta_{2y} + 4l\theta_{h2y}\right)}{3600l}$$

$$k_{9,12}^{G} = \frac{E_p A\left(6u_z - l\theta_{2y} + 4l\theta_{h2y}\right)\left(6u_y + 4l\theta_{2z} - l\theta_{h2z}\right)}{3600l}$$

$$k_{10,11}^{G} = \frac{E_p A\left(-6u_z + l\left(\theta_{2y} - 4\theta_{h2y}\right)\right)\left(-6u_y + l\left(\theta_{2z} - 4\theta_{h2z}\right)\right)}{3600l}$$

$$k_{10,12}^{G} = -\frac{F_{ex}l}{60} + \frac{E_p A\left(6u_y + 4l\theta_{hz2} - l\theta_{z2}\right)\left(6u_y - l\theta_{hz2} + 4l\theta_{z2}\right)}{3600l}$$

$$k_{11,11}^{G} = \frac{F_{ex}l}{15} + \frac{E_p A\left(6u_z - l\theta_{hy2} + 4l\theta_{y2}\right)^2}{3600l}, \quad k_{12,12}^{G} = \frac{F_{ex}l}{15} + \frac{E_p A\left(6u_y - l\theta_{hz2} + 4l\theta_{z2}\right)^2}{3600l}$$

$$k_{11,12}^{G} = -\frac{E_p A\left(6u_z + 4l\theta_{2y} - l\theta_{h2y}\right)\left(-6u_y + l\left(\theta_{2z} - 4\theta_{h2z}\right)\right)}{3600l}$$

Appendix II – The condensed matrix considering the plastic hinges

The degrees of freedom of element $\{u\}$ are divided into two parts:

$$\{u_e\} = \{s_x \quad \theta_{1y} \quad \theta_{1z} \quad \theta_x \quad \theta_{2y} \quad \theta_{2z}\}^T \tag{6.22}$$

$$\{u_h\} = \{\theta_{h1y} \quad \theta_{h1z} \quad u_z \quad u_y \quad \theta_{h2y} \quad \theta_{h2z}\}^T \tag{6.23}$$

The stiffness matrix $[k_E]$ is reorganized according to the corresponding degrees of freedom of $\{u_e\}$ and $\{u_h\}$, and the following stiffness equation is obtained by:

$$\begin{bmatrix} k_{hh} & k_{he} \\ k_{he}^T & k_{ee} \end{bmatrix} \begin{bmatrix} u_h \\ u_e \end{bmatrix} = \begin{bmatrix} f_h \\ f_e \end{bmatrix} \tag{6.24}$$

The condensed stiffness $[k_c]$ and the corresponding force $\{f_c\}$ can be expressed as:

$$[k_c]\{u_e\} = \{f_c\} \tag{6.25}$$

and,

$$\left[k_c\right]=\left[k_{ee}\right]-\left[k_{he}\right]^T\left[k_{hh}\right]^{-1}\left[k_{he}\right]$$

$$=\begin{bmatrix} k_{11}^c & k_{12}^c & k_{13}^c & k_{14}^c & k_{15}^c & k_{16}^c \\ & k_{22}^c & k_{23}^c & k_{24}^c & k_{25}^c & k_{26}^c \\ & & k_{33}^c & k_{34}^c & k_{35}^c & k_{36}^c \\ & & & k_{44}^c & k_{45}^c & k_{46}^c \\ & & & & k_{55}^c & k_{56}^c \\ SYM. & & & & & k_{66}^c \end{bmatrix} \tag{6.26}$$

The generalized force $\{f_c\}$ is given by:

$$\left\{f_c\right\}=\left\{f_e\right\}-\left[k_{he}\right]^T\left[k_{hh}\right]^{-1}\left\{f_h\right\}$$

The condensed stiffness matrix is updated by incorporating plastic hinges at element ends along y- and z-directions:

$$\left[k_U\right]=\begin{bmatrix} k_{11}^c & k_{12}^c & k_{13}^c & k_{14}^c & k_{15}^c & k_{16}^c \\ & k_{22}^u & k_{23}^c & k_{24}^c & k_{25}^u & k_{26}^c \\ & & k_{33}^u & k_{34}^c & k_{35}^c & k_{36}^u \\ & & & k_{44}^c & k_{45}^c & k_{46}^c \\ & & & & k_{55}^u & k_{56}^c \\ SYM. & & & & & k_{66}^u \end{bmatrix} \tag{6.27}$$

where

$$k_{22}^u=\frac{E_pI_yR_y^t}{l}-\frac{\left(E_pI_yR_y^t\right)^2\left(k_{55}^c+E_pI_yR_y^b/l\right)}{\left(k_{22}^cl+E_pI_yR_y^t\right)\left(k_{55}^cl+E_pI_yR_y^b\right)-k_{25}^ck_{52}^cl^2} \tag{6.28}$$

$$k_{25}^u=\frac{\left(E_pI_y\right)^2R_y^tR_y^bk_{25}^c}{\left(k_{22}^cl+E_pI_yR_y^t\right)\left(k_{55}^cl+E_pI_yR_y^b\right)-k_{25}^ck_{52}^cl^2} \tag{6.29}$$

$$k_{55}^u=\frac{E_pI_yR_y^b}{l}-\frac{\left(E_pI_yR_y^b\right)^2\left(k_{22}^c+E_pI_yR_y^t/l\right)}{\left(k_{22}^cl+E_pI_yR_y^t\right)\left(k_{55}^cl+E_pI_yR_y^b\right)-k_{25}^ck_{52}^cl^2} \tag{6.30}$$

$$k_{33}^u=\frac{E_pI_yR_z^t}{l}-\frac{\left(E_pI_zR_z^t\right)^2\left(k_{66}^c+E_pI_zR_z^b/l\right)}{\left(k_{33}^cl+E_pI_zR_z^t\right)\left(k_{66}^cl+E_pI_zR_z^b\right)-k_{36}^ck_{63}^cl^2} \tag{6.31}$$

$$k_{36}^u=\frac{\left(E_pI_z\right)^2R_z^tR_z^bk_{36}^c}{\left(k_{33}^cl+E_pI_zR_z^t\right)\left(k_{66}^cl+E_pI_zR_z^b\right)-k_{36}^ck_{63}^cl^2} \tag{6.32}$$

$$k_{66}^{u}=\frac{E_pI_yR_z^b}{l}-\frac{\left(E_pI_zR_z^b\right)^2\left(k_{33}^c+E_pI_zR_z^t/l\right)}{\left(k_{33}^cl+E_pI_zR_z^t\right)\left(k_{66}^cl+E_pI_zR_z^b\right)-k_{36}^ck_{63}^cl^2} \tag{6.33}$$

where superscripts *b* and *t* denote the bottom and top plastic hinges at the two ends of an element, respectively.

Appendix III – Soil stiffness matrices

The soil stiffness matrix is given by:

$$[k_S]=\begin{bmatrix}
\zeta_1 l & 0 & 0 & 0 & 0 & 0 & \zeta_2 l & 0 & 0 & 0 & 0 & 0\\
 & \chi_1 l & 0 & 0 & 0 & \chi_2 l^2 & 0 & \chi_3 l & 0 & 0 & 0 & \chi_4 l^2\\
 & & \chi_5 l & 0 & \chi_6 l^2 & 0 & 0 & 0 & \chi_7 l & 0 & \chi_8 l^2 & 0\\
 & & & 0 & 0 & 0 & 0 & 0 & 0 & 0 & 0 & 0\\
 & & & & \chi_9 l^3 & 0 & 0 & 0 & \chi_{10} l^2 & 0 & \chi_{11} l^3 & 0\\
 & & & & & \chi_{12} l^3 & 0 & \chi_{13} l^2 & 0 & 0 & 0 & \chi_{14} l^3\\
 & & & & & & \zeta_3 l & 0 & 0 & 0 & 0 & 0\\
 & & S. & & & & & \chi_{15} l & 0 & 0 & 0 & \chi_{16} l^2\\
 & & & Y. & & & & & \chi_{17} l & 0 & \chi_{18} l^2 & 0\\
 & & & & M. & & & & & 0 & 0 & 0\\
 & & & & & & & & & & \chi_{19} l^3 & 0\\
 & & & & & & & & & & & \chi_{20} l^3
\end{bmatrix} \tag{6.34}$$

where the values of χ_1 to χ_{20} and γ_{1j} to γ_{3j} can be respectively obtained by:

$$\chi_q=\sum_{j=1}^{n}\delta_{q,j}\kappa_{\rho,j}\qquad (q=1\sim 20) \tag{6.35}$$

$$\zeta_m=\sum_{j=1}^{n}\gamma_{m,j}\kappa_{x,j}\qquad (m=1\sim 3) \tag{6.36}$$

where $\delta_{1,j}$ to $\delta_{20,j}$ and $\gamma_{1,j}$ to $\gamma_{3,j}$ are the integration parameters which are obtained by Gauss-Legendre integration method.

The transformation matrices $[\eta]$ and $[\chi]$ are respectively written as:

$$[\eta]=\begin{bmatrix} -1 & 0 & 0 & 0 & 0 & 0 \\ 0 & 0 & 1/l & 0 & 0 & 1/l \\ 0 & -1/l & 0 & 0 & -1/l & 0 \\ 0 & 0 & 0 & -1 & 0 & 0 \\ 0 & 1 & 0 & 0 & 0 & 0 \\ 0 & 0 & 1 & 0 & 0 & 0 \\ 1 & 0 & 0 & 0 & 0 & 0 \\ 0 & 0 & -1/l & 0 & 0 & -1/l \\ 0 & 1/l & 0 & 0 & 1/l & 0 \\ 0 & 0 & 0 & 1 & 0 & 0 \\ 0 & 0 & 0 & 0 & 1 & 0 \\ 0 & 0 & 0 & 0 & 0 & 1 \end{bmatrix} \tag{6.37}$$

$$[\chi]=\begin{bmatrix} 0 & T_z & -T_y & 0 & 0 & 0 & 0 & -T_z & T_y & 0 & 0 & 0 \\ & T_x & 0 & 0 & 0 & 0 & -T_z & -T_x & 0 & 0 & 0 & 0 \\ & & T_x & 0 & 0 & 0 & T_y & 0 & -T_x & 0 & 0 & 0 \\ & & & 0 & 0 & 0 & 0 & 0 & 0 & 0 & 0 & 0 \\ & & & & 0 & 0 & 0 & 0 & 0 & 0 & 0 & 0 \\ & & & & & 0 & 0 & 0 & 0 & 0 & 0 & 0 \\ & & & & & & 0 & T_z & -T_y & 0 & 0 & 0 \\ & & & & & & & T_x & 0 & 0 & 0 & 0 \\ & & & & & & & & T_x & 0 & 0 & 0 \\ & & & & & & & & & 0 & 0 & 0 \\ & & & & & & & & & & 0 & 0 \\ SYM. & & & & & & & & & & & 0 \end{bmatrix} \tag{6.38}$$

where

$$T_z=\frac{M_{e1z}+M_{e2z}}{l^2} \tag{6.39}$$

$$T_y=\frac{M_{e1y}+M_{e2y}}{l^2} \tag{6.40}$$

$$T_x=\frac{F_{ex}}{l} \tag{6.41}$$

Appendix IV – Element nodal forces

The nodal forces of an element can be obtained by the first variation of the potential energy function according to the minimum potential energy principle. The condensed nodal force vector in the local coordinate $\{f_E\}$ is given by:

$$\{f_E\} = \{F_{ex} \quad M_{e1y} \quad M_{e1z} \quad M_x \quad M_{e2y} \quad M_{e2z}\}^T \tag{6.42}$$

where

$$\begin{aligned} F_{ex} = {} & \frac{E_p A s_x}{l} + \frac{E_p A}{60l^2}(144u_y{}^2 + 144u_z{}^2 - 6lu_z(\theta_{1y} - \theta_{2y} + \theta_{h1y} - \theta_{h2y}) \\ & -6lu_y\left(\theta_{1z} - \theta_{2z} + \theta_{h1z} - \theta_{h2z}\right) + l^2(2\theta_{1y}{}^2 + 2\theta_{1z}{}^2 + 2\theta_{2y}{}^2 + 2\theta_{2z}{}^2 - \\ & \theta_{1y}\theta_{h1y} + 2\theta_{h1y}{}^2 - \theta_{1z}\theta_{h1z} + 2\theta_{h1z}{}^2 - \theta_{2y}\theta_{h2y} + 2\theta_{h2y}{}^2 - \theta_{2z}\theta_{h2z} + 2\theta_{h2z}{}^2)) \end{aligned} \tag{6.43}$$

$$M_{e1y} = -\frac{F_{ex}u_z}{10} - \frac{24E_pI_yu_z}{l^2} + \frac{8E_pI_y\theta_{1y}}{l} + \frac{F_xL\theta_{1y}}{15} + \frac{4E_pI_y\theta_{h1y}}{l} - \frac{F_xl\theta_{h1y}}{60} \tag{6.44}$$

$$M_{e1z} = -\frac{F_{ex}u_y}{10} - \frac{24E_pI_zu_y}{l^2} + \frac{8E_pI_z\theta_{1z}}{l} + \frac{F_{ex}L\theta_{1z}}{15} + \frac{4E_pI_z\theta_{h1z}}{l} - \frac{F_{ex}l\theta_{h1z}}{60} \tag{6.45}$$

$$M_x = \frac{GJ\theta_x}{l} \tag{6.46}$$

$$M_{e2y} = \frac{F_{ex}u_z}{10} + \frac{24E_pI_yu_z}{l^2} + \frac{8E_pI_y\theta_{2y}}{l} + \frac{F_{ex}l\theta_{2y}}{15} + \frac{4E_pI_y\theta_{h2y}}{l} - \frac{F_{ex}l\theta_{h2y}}{60} \tag{6.47}$$

$$M_{e2z} = \frac{F_{ex}u_y}{10} + \frac{24E_pI_zu_y}{l^2} + \frac{8E_pI_z\theta_{2z}}{l} + \frac{F_{ex}l\theta_{2z}}{15} + \frac{4E_pI_z\theta_{h2z}}{l} - \frac{F_{ex}l\theta_{h2z}}{60} \tag{6.48}$$

The nodal force vector for plastic hinge $\{f_h\}$ are given by

$$\{f_h\} = \{M_{h1y} \quad M_{h1z} \quad F_{hz} \quad F_{hy} \quad M_{h2y} \quad M_{h2z}\}^T \tag{6.49}$$

where

$$M_{h1y} = -\frac{F_{ex}u_z}{10} - \frac{24E_pI_yu_z}{l^2} + \frac{4E_pI_y\theta_{1y}}{l} - \frac{F_{ex}l\theta_{1y}}{60} + \frac{8E_pI_y\theta_{h1y}}{l} + \frac{F_{ex}l\theta_{h1y}}{15} \tag{6.50}$$

$$M_{h1z} = -\frac{F_{ex}u_y}{10} - \frac{24E_pI_zu_y}{l^2} + \frac{4E_pI_z\theta_{1z}}{l} - \frac{F_{ex}l\theta_{1z}}{60} + \frac{8E_pI_z\theta_{h1z}}{l} + \frac{F_{ex}l\theta_{h1z}}{15} \tag{6.51}$$

$$\begin{aligned} F_{hz} = {} & \frac{192E_pI_yu_z}{l^3} + \frac{24F_{ex}u_z}{5l} - \frac{F_{ex}\theta_{1y}}{10} - \frac{24E_pI_y\theta_{1y}}{l^2} + \frac{F_{ex}\theta_{2y}}{10} + \frac{24E_pI_y\theta_{2y}}{l^2} \\ & -\frac{F_{ex}\theta_{h1y}}{10} - \frac{24E_pI_y\theta_{h1y}}{l^2} + \frac{F_{ex}\theta_{h2y}}{10} + \frac{24E_pI_y\theta_{h2y}}{l^2} \end{aligned} \tag{6.52}$$

$$\begin{aligned} F_{hy} &= \frac{192E_pI_zu_y}{l^3}+\frac{24F_{ex}u_y}{5l}-\frac{F_{ex}\theta_{1z}}{10}-\frac{24E_pI_z\theta_{1z}}{l^2}+\frac{F_{ex}\theta_{2z}}{10}+\frac{24E_pI_z\theta_{2z}}{l^2} \\ &-\frac{F_{ex}\theta_{h1z}}{10}-\frac{24E_pI_z\theta_{h1z}}{l^2}+\frac{F_{ex}\theta_{h2z}}{10}+\frac{24E_pI_z\theta_{h2z}}{l^2} \end{aligned} \tag{6.53}$$

$$M_{h2y} = \frac{F_{ex}u_z}{10}+\frac{24E_pI_yu_z}{l^2}+\frac{4E_pI_y\theta_{2y}}{l}-\frac{F_{ex}l\theta_{2y}}{60}+\frac{8E_pI_y\theta_{h2y}}{l}+\frac{F_{ex}l\theta_{h2y}}{15} \tag{6.54}$$

$$M_{h2z} = \frac{F_{ex}u_y}{10}+\frac{24E_pI_zu_y}{l^2}+\frac{4E_pI_z\theta_{2z}}{l}-\frac{F_{ex}l\theta_{2z}}{60}+\frac{8E_pI_z\theta_{h2z}}{l}+\frac{F_{ex}l\theta_{h2z}}{15} \tag{6.55}$$

The resistance force vector from soil springs $\{f_S\}$ consists of skin friction and lateral soil resistance, which is given in the form of Gauss-Legendre integration:

$$\{f_S\}=\{F_{s1x}\quad F_{s1y}\quad F_{s1z}\quad M_{s1x}\quad M_{s1y}\quad M_{s1z}\quad F_{s2x}\quad F_{s2y}\quad F_{s2z}\quad M_{s2x}\quad M_{s2y}\quad M_{s2z}\}^T \tag{6.56}$$

where

$$F_{s1x}=\int_l\left(1-\frac{x}{l}\right)p_x(x)\,dx\approx l\sum_{m=1}^{n}\lambda_{1,m}p_x(x_m) \tag{6.57}$$

$$F_{s2x}=\int_l\frac{x}{l}p_x(x)\,dx\approx l\sum_{m=1}^{n}\lambda_{2,m}p_x(x_m) \tag{6.58}$$

$$F_{s1y}=\int_l\left(\frac{3x}{l}+\frac{l-x}{l}\right)\left(1-\frac{x}{l}\right)^2p_\rho(\rho)\cos\varphi\,d\rho\approx l\sum_{m=1}^{n}\lambda_{3,m}p_\rho(\rho_m)\cos\varphi \tag{6.59}$$

$$F_{s2y}=-\int_l\left[\frac{x}{l}+\frac{3(l-x)}{l}\right]\left(\frac{x}{l}\right)^2p_\rho(\rho)\cos\varphi\,d\rho\approx -l\sum_{m=1}^{n}\lambda_{4,m}p_\rho(\rho_m)\cos\varphi \tag{6.60}$$

$$F_{s1z}=\int_l\left(\frac{3x}{l}+\frac{l-x}{l}\right)\left(1-\frac{x}{l}\right)^2p_\rho(\rho)\sin\varphi\,d\rho\approx l\sum_{m=1}^{n}\lambda_{3,m}p_\rho(\rho_m)\sin\varphi \tag{6.61}$$

$$F_{s2z}=-\int_l\left[\frac{x}{l}+\frac{3(l-x)}{l}\right]\left(\frac{x}{l}\right)^2p_\rho(\rho)\sin\varphi\,d\rho\approx -l\sum_{m=1}^{n}\lambda_{4,m}p_\rho(\rho_m)\sin\varphi \tag{6.62}$$

$$M_{s1y}=\int_l x\left(1-\frac{x}{l}\right)^2p_\rho(\rho)\sin\varphi\,d\rho=l^2\sum_{m=1}^{n}\lambda_{5,m}p_\rho(\rho_m)\sin\varphi \tag{6.63}$$

$$M_{s2y}=-\int_l \frac{x^2}{l^2}\left(l-x\right)p_\rho\left(\rho\right)\sin\varphi d\rho\approx -l^2\sum_{m=1}^{n}\lambda_{6,m}p_\rho\left(\rho_m\right)\sin\varphi \tag{6.64}$$

$$M_{s1z}=\int_l x\left(1-\frac{x}{l}\right)^2 p_\rho\left(\rho\right)\cos\varphi d\rho = l^2\sum_{m=1}^{n}\lambda_{5,m}p_\rho(\rho_m)\cos\varphi \tag{6.65}$$

$$M_{s2z}=-\int_l \frac{x^2}{l^2}\left(l-x\right)p_\rho\left(\rho\right)\cos\varphi d\rho\approx -l^2\sum_{m=1}^{n}\lambda_{6,m}p_\rho\left(\rho_m\right)\cos\varphi \tag{6.66}$$

where the coefficients $\lambda_{1,m}$ to $\lambda_{6,m}$ are the integration parameters; φ is the angle of lateral load; and, n is the total integration points.

General conclusions

This thesis undertakes an investigation of the mechanical behavior within the realm of pile-soil systems, specifically focusing on the incorporation of fiber-reinforced polymer (FRP) piles and rubber-soil mixtures (RSM). The investigation uses molecular dynamics (MD) simulations to address three aspects: 1) Elucidate the friction properties at the interface between FRP piles and clay using a kaolinite-epoxy surface model. 2) Investigate the mechanics governing the interactions at the silica-epoxy interfaces through nanoscale simulations in dry, pure water, and saltwater systems. 3) Analyze the intricacies of the rubber-clay interface within the RSM system to explore potential ways to mitigate the effects of dynamic loading. In addition, this thesis presents a novel approach using the finite element (FE) method, leading to the development of an efficient integrated pile-soil element. This innovative element aims to simulate pile behavior on an engineering scale.

(1) The study investigates the friction behavior between FRP piles and clay from an atomic scale using MD simulation. The siloxane surface of kaolinite chosen for contact with epoxy resin due to its lower surface energy results in well-fitting kaolinite surfaces. The work of adhesion between epoxy and kaolinite is calculated to be 159 mJ/m^2. The peak interfacial shear coefficient decreases nonlinearly with increasing normal stress, which affects the friction in a manner consistent with FRP-soil interface tests. The nanofriction between them is velocity dependent, with distinct slow and fast velocity regions, and the energy barriers increase with normal stress, explaining the higher pulling forces required for sliding at higher stress.

(2) The MD simulation examines interfacial friction at the interface of an FRP pile and sand, considering various environmental conditions, normal stress levels, and sliding velocities. The friction force-displacement profiles show distinct nonlinear and steady-state phases. The tangential stiffness profiles, especially at lower normal stress levels, show a more rapid reduction to zero. The initial tangential stiffness is higher in dry systems than in those immersed in pure water or salt water environments. The presence of water molecules has a pronounced effect on the friction behavior, acting as a lubricant with a complex effect on the friction characteristics. The introduction of NaCl ions tends to undermine the lubricating effect, resulting in changes in the friction response. Specifically, the coefficient of friction is highest in the dry system under identical applied normal stress conditions. This is followed by the saltwater system, while the pure water system exhibits the lowest coefficient of friction.

Furthermore, the water-based lubrication proves to be more effective at lower sliding velocities, highlighting its role in the interfacial friction response.

(3) Friction behavior of rubber/soil interfaces in RSM is studied using MD simulations. The friction force shows a consistent increase with both sliding distance and applied normal stress, similar to the behavior observed in natural soils. This behavior suggests that compacting the rubber and clay components within the RSM could enhance the friction forces, resulting in improved mechanical properties for engineering applications. In addition, the introduction of rubber reduces stick-slip motion at the montmorillonite/rubber interface, resulting in reduced pore water pressure. This reduction has implications for optimizing design parameters when considering different soil pressures and sliding velocities. Stick-slip motion is observed at certain velocities but is eliminated at higher velocities due to the limited interfacial adaptation time. The work establishes interface parameters, work of adhesion, and friction coefficients and their agreement with experimental data, furthering the understanding of RSM behavior and its application in foundation soil.

(4) Based on the FE method, the efficient pile-soil integrated element is proposed to simulate the pile behavior, taking into account the nonlinearity of both soil and pile materials. Plastic hinges at the ends and center of the element capture the inelastic pile behavior. The proposed method compares favorably with 3D solid element model and the EPE model in terms of effectiveness. It accurately predicts buckling behavior and inelasticity effects. Validation with field load tests demonstrates its accuracy for both lateral and axial pile loading. The proposed method provides convenience and efficiency for the analysis of pile-soil systems in large structures.

Perspectives

In practical engineering, pile foundations are essential for transferring loads from the superstructure to ensure that the structure meets the deformation requirements of the design. Nonlinear soil springs are commonly used in numerical simulations to represent the load transfer relationship between the vertical pile-soil interaction. The stress-strain relationship of springs represents the relationship between frictional resistance and displacement, known as *t-z* curves. Different *t-z* curve models exist for different soil and pile types. The mechanical properties of the interface under different sliding velocities and normal stresses have the potential to provide theoretical parameters for *t-z* curve models, thereby improving predictive capabilities for FRP pile-soil interactions in engineering-scale problems. However, this MD work may not provide a complete representation of the complex behavior of the actual FRP-soil interface due to the limitations of computational resources and capabilities. Therefore, future research could focus on applying the coarse-grained model [267], on the base of this work, to efficiently model the complicated and large system comprising the surface between FRP piles and soil, with the aim of computing frictional properties for experimental validation.

References

[1] J.J. Crispin, Static and dynamic analysis of piles in inhomogeneous soil, in, University of Bristol, 2022.

[2] H. Khabbaz, R. Gibson, B. Fatahi, Effect of constructing twin tunnels under a building supported by pile foundations in the Sydney central business district, Underground Space, 4 (2019) 261-276.

[3] H.G. Poulos, E.H. Davis, Pile foundation analysis and design, Wiley New York, 1980.

[4] R. Di Laora, L. de Sanctis, Piles-induced filtering effect on the foundation input motion, Soil Dynamics and Earthquake Engineering, 46 (2013) 52-63.

[5] K.-H.E. Kim, B. Andrawes, Compression behavior of FRP strengthened bridge timber piles subjected to accelerated aging, Construction and Building Materials, 124 (2016) 177-185.

[6] K. Zyka, A. Mohajerani, Composite piles: A review, Construction and Building Materials, 107 (2016) 394-410.

[7] N. Gathimba, Y. Kitane, T. Yoshida, Y. Itoh, Surface roughness characteristics of corroded steel pipe piles exposed to marine environment, Construction and Building Materials, 203 (2019) 267-281.

[8] Y. Shin, M. Kim, J. Ko, S. Jeong, Proposed design chart of mechanical joints on steel-PHC composite piles, Materials and structures, 47 (2014) 1221-1238.

[9] A. Mohammadi, J.H. Gull, R. Taghinezhad, A. Azizinamini, Assessment and evaluation of timber piles used in Nebraska for retrofit and rating, (2014).

[10] S.S. Khedmatgozar Dolati, A. Mehrabi, Review of available systems and materials for splicing prestressed-precast concrete piles, Structures, 30 (2021) 850-865.

[11] P. Doherty, D. Igoe, G. Murphy, K. Gavin, J. Preston, C. McAvoy, B.W. Byrne, R. McAdam, H.J. Burd, G.T. Houlsby, C.M. Martin, L. Zdravković, D.M.G. Taborda, D.M. Potts, R.J. Jardine, M. Sideri, F.C. Schroeder, A. Muir Wood, D. Kallehave, J. Skov Gretlund, Field validation of fibre Bragg grating sensors for measuring strain on driven steel piles, Géotechnique Letters, 5 (2015) 74-79.

[12] Z.K. Awad, T. Aravinthan, Y. Zhuge, F. Gonzalez, A review of optimization techniques used in the design of fibre composite structures for civil engineering applications, Materials & Design, 33 (2012) 534-544.

[13] E. Guades, T. Aravinthan, M. Islam, A. Manalo, A review on the driving performance of FRP composite piles, Composite Structures, 94 (2012) 1932-1942.

[14] M.G. Iskander, M. Hassan, State of the practice review in FRP composite piling, Journal of Composites for Construction, 2 (1998) 116-120.

[15] M.X. Zhu, Y.B. Zhang, W.M. Gong, L. Wang, G.L. Dai, Generalized Solutions for Axially and Laterally Loaded Piles in Multilayered Soil Deposits with Transfer Matrix Method, Int J Geomech, 17 (2017).

[16] API, Recommended Practice for Planning, Designing and Constructing Fixed Offshore Platforms—Working Stress Design, in: American Petroleum Institute, 2002.

[17] A.H. Bateman, J.J. Crispin, P.J. Vardanega, G.E. Mylonakis, Theoretical t-z Curves for Axially Loaded Piles, Journal of Geotechnical and Geoenvironmental Engineering, 148 (2022) 04022052.

[18] E. Van Buren, M. Muskulus, Improving pile foundation models for use in bottom-fixed offshore wind turbine applications, Energy Procedia, 24 (2012) 363-370.

[19] T. Tikanta, T. Matsumoto, A. Vu, S. Kobayashi, S. Shimono, C. Bamrungwong, Fundamental experiments on a reinforcement method using sheet pile wall for bridge pile foundations subjected to pile embedment reduction and numerical validation, J. of the SEAGS & AGSEA, 48 (2017) 25-39.

[20] M.J. Abyaneh, H. El Naggar, P. Sadeghian, Numerical Modeling of the Lateral Behavior of Concrete-Filled FRP Tube Piles in Sand, International Journal of Geomechanics, 20 (2020) 04020108.
[21] J. Giraldo Valez, M.T. Rayhani, Axial and lateral load transfer of fibre-reinforced polymer (FRP) piles in soft clay, International Journal of Geotechnical Engineering, (2016) 1-7.
[22] M. Sakr, M.H.E. Naggar, M. Nehdi, Load transfer of fibre-reinforced polymer (FRP) composite tapered piles in dense sand, Canadian geotechnical journal, 41 (2004) 70-88.
[23] J.S. Park, S.S. Lee, J.H. Nam, I.K. Kang, D.J. An, S.J. Yoon, Load Carrying Capacity of Hybrid FRP-Concrete Composite Pile, in: Advanced Materials Research, Trans Tech Publ, 2011, pp. 1165-1172.
[24] B. Indraratna, Recent Advances in Soft Soil Consolidation, in: Ground Improvement Case Histories, 2015, pp. 3-32.
[25] V.R. Raju, W. Sondermann, Ground Improvement Using Deep Vibro Techniques, in: Ground Improvement Case Histories, 2015, pp. 175-213.
[26] P. Simonini, Analysis of Behavior of Sand Surrounding Pile Tips, Journal of Geotechnical Engineering, 122 (1996) 897-905.
[27] D. Loukidis, R. Salgado, Analysis of the shaft resistance of non-displacement piles in sand, Géotechnique, 58 (2008) 283-296.
[28] P. Basu, D. Loukidis, M. Prezzi, R. Salgado, Analysis of shaft resistance of jacked piles in sands, International Journal for Numerical and Analytical Methods in Geomechanics, 35 (2011) 1605-1635.
[29] V.D. Gennaro, R. Frank, Elasto-plastic analysis of the interface behaviour between granular media and structure, Computers and Geotechnics, 29 (2002) 547-572.
[30] A. Lashkari, M. Kadivar, A constitutive model for unsaturated soil-structure interfaces, International Journal for Numerical and Analytical Methods in Geomechanics, 40 (2016) 207-234.
[31] Y. Chow, Analysis of vertically loaded pile groups, International journal for numerical and analytical methods in geomechanics, 10 (1986) 59-72.
[32] E. Alonso, A. Josa, A. Ledesma, Negative skin friction on piles: a simplified analysis and prediction procedure, Geotechnique, 34 (1984) 341-357.
[33] J. Liu, H.B. Xiao, J. Tang, Q.S. Li, Analysis of load-transfer of single pile in layered soil, Computers and Geotechnics, 31 (2004) 127-135.
[34] W. Yao, Y. Liu, J. Chen, Characteristics of Negative Skin Friction for Superlong Piles under Surcharge Loading, International Journal of Geomechanics, 12 (2012) 90-97.
[35] H.M. Coyle, L.C. Reese, Load Transfer for Axially Loaded Piles in Clay, Journal of the Soil Mechanics and Foundations Division, 92 (1966) 1-26.
[36] A.S. Alawneh, Modelling load–displacement response of driven piles in cohesionless soils under tensile loading, Computers and Geotechnics, 32 (2005) 578-586.
[37] S. Lee, J.H. Long, Skin friction features of drilled CIP piles in sand from pile segment analysis, International Journal for Numerical and Analytical Methods in Geomechanics, 32 (2008) 745-770.
[38] H. Zhu, M.-F. Chang, Load Transfer Curves along Bored Piles Considering Modulus Degradation, Journal of Geotechnical and Geoenvironmental Engineering, 128 (2002) 764-774.
[39] S.W. Liu, J.H. Wan, C.Y. Zhou, Z. Liu, X. Yang, Efficient Beam-Column Finite-Element Method for Stability Design of Slender Single Pile in Soft Ground Mediums, International Journal of Geomechanics, 20 (2020) 04019148.
[40] W. Cao, H. Guo, Y. Zhang, R. Ma, Y. Li, Q. Dong, Y. Li, R. Zhao, Controls of paleochannels on groundwater arsenic distribution in shallow aquifers of alluvial plain in the Hetao Basin, China, Science of the Total Environment, 613 (2018) 958-968.

[41] G. Wu, L. He, D. Chen, Sorption and distribution of asphaltene, resin, aromatic and saturate fractions of heavy crude oil on quartz surface: molecular dynamic simulation, Chemosphere, 92 (2013) 1465-1471.
[42] N. Fagel, Chapter four clay minerals, deep circulation and climate, Developments in marine geology, 1 (2007) 139-184.
[43] M.O. Schrenk, D.S. Kelley, J.R. Delaney, J.A. Baross, Incidence and diversity of microorganisms within the walls of an active deep-sea sulfide chimney, Applied and Environmental Microbiology, 69 (2003) 3580-3592.
[44] G. Li, H. Wang, X. Shi, C. Yang, R. Wang, B. He, J. Jin, Y. Gong, A. Tang, H. Yang, A montmorillonite-modification strategy enabling long cycling stability of dual-ion batteries, Chemical Communications, 58 (2022) 11276-11279.
[45] H.H. Tsang, Seismic isolation by rubber–soil mixtures for developing countries, Earthquake engineering & structural dynamics, 37 (2008) 283-303.
[46] Y. Mishin, M. Asta, J. Li, Atomistic modeling of interfaces and their impact on microstructure and properties, Acta Materialia, 58 (2010) 1117-1151.
[47] D. Lau, W. Jian, Z. Yu, D. Hui, Nano-engineering of construction materials using molecular dynamics simulations: Prospects and challenges, Composites Part B: Engineering, 143 (2018) 282-291.
[48] P.M. Amarasinghe, A. Anandarajah, P. Ghosh, Molecular dynamic study of capillary forces on clay particles, Applied Clay Science, 88-89 (2014) 170-177.
[49] R. Shahsavari, L. Chen, L. Tao, Edge dislocations in dicalcium silicates: Experimental observations and atomistic analysis, Cement and Concrete Research, 90 (2016) 80-88.
[50] W. Sekkal, A. Zaoui, Nanoscale analysis of the morphology and surface stability of calcium carbonate polymorphs, Sci Rep, 3 (2013) 1587.
[51] D. Tunega, A. Zaoui, Mechanical and Bonding Behaviors Behind the Bending Mechanism of Kaolinite Clay Layers, J Phys Chem C Nanomater Interfaces, 124 (2020) 7432-7440.
[52] Y. Zheng, A. Zaoui, Temperature effects on the diffusion of water and monovalent counterions in the hydrated montmorillonite, Physica A: Statistical Mechanics and its Applications, 392 (2013) 5994-6001.
[53] J.R. Maple, U. Dinur, A.T. Hagler, Derivation of force fields for molecular mechanics and dynamics from ab initio energy surfaces, Proceedings of the National Academy of Sciences, 85 (1988) 5350-5354.
[54] R.T. Cygan, J.-J. Liang, A.G. Kalinichev, Molecular models of hydroxide, oxyhydroxide, and clay phases and the development of a general force field, The Journal of Physical Chemistry B, 108 (2004) 1255-1266.
[55] M.P. Allen, D.J. Tildesley, Computer simulation of liquids, Oxford university press, 2017.
[56] S. Park, K. Schulten, Calculating potentials of mean force from steered molecular dynamics simulations, The Journal of chemical physics, 120 (2004) 5946-5961.
[57] A.K. Gand, T.-M. Chan, J.T. Mottram, Civil and structural engineering applications, recent trends, research and developments on pultruded fiber reinforced polymer closed sections: a review, Frontiers of Structural and Civil Engineering, 7 (2013) 227-244.
[58] A.A. Mohammed, A.C. Manalo, W. Ferdous, Y. Zhuge, P. Vijay, A.Q. Alkinani, A. Fam, State-of-the-art of prefabricated FRP composite jackets for structural repair, Engineering Science and Technology, an International Journal, 23 (2020) 1244-1258.
[59] A. Vedernikov, A. Safonov, F. Tucci, P. Carlone, I. Akhatov, Pultruded materials and structures: A review, Journal of Composite Materials, 54 (2020) 4081-4117.
[60] M.M. Prabhakar, N. Rajini, N. Ayrilmis, K. Mayandi, S. Siengchin, K. Senthilkumar, S. Karthikeyan, S.O. Ismail, An overview of burst, buckling, durability and corrosion analysis of lightweight FRP composite pipes and their applicability, Composite Structures, 230 (2019) 111419.

[61] J. Giraldo, M. Rayhani, Influence of fiber-reinforced polymers on pile–soil interface strength in clays, Advances in civil engineering materials, 2 (2013) 1-17.

[62] P. Morampudi, K.K. Namala, Y.K. Gajjela, M. Barath, G. Prudhvi, Review on glass fiber reinforced polymer composites, Materials Today: Proceedings, 43 (2021) 314-319.

[63] T. Zhang, S. Liu, G. Cai, Correlations between electrical resistivity and basic engineering property parameters for marine clays in Jiangsu, China, Journal of Applied Geophysics, 159 (2018) 640-648.

[64] J. Giraldo, M.T. Rayhani, Load transfer of hollow Fiber-Reinforced Polymer (FRP) piles in soft clay, Transportation Geotechnics, 1 (2014) 63-73.

[65] M. Hosseini, Evaluation of Seismic Behaviour of Hollow Fibre-Reinforced Polymer (FRP) Piles using Shake Table Testing, in, Carleton University, 2021.

[66] X. Gu, M. Huang, J. Qian, DEM investigation on the evolution of microstructure in granular soils under shearing, Granular Matter, 16 (2013) 91-106.

[67] M. Jiang, A. Zhang, C. Fu, 3-D DEM simulations of drained triaxial tests on inherently anisotropic granulates, European Journal of Environmental and Civil Engineering, 22 (2017) s37-s56.

[68] J.D. Frost, J. Han, Behavior of interfaces between fiber-reinforced polymers and sands, Journal of Geotechnical and Geoenvironmental Engineering, 125 (1999) 633-640.

[69] M.A. Pando, G.M. Filz, J.E. Dove, E.J. Hoppe, Interface Shear Tests on FRP Composite Piles, in: Deep Foundations 2002, 2002, pp. 1486-1500.

[70] H. He, W. Chen, Z.-Y. Yin, K. Senetakis, J.-H. Yin, A micromechanical-based study on the tribological and creep-relaxation behavior of sand-FRP composite interfaces, Composite Structures, 275 (2021).

[71] W.-G. Jiang, Y. Wu, Q.-H. Qin, D.-S. Li, X.-B. Liu, M.-F. Fu, A molecular dynamics based cohesive zone model for predicting interfacial properties between graphene coating and aluminum, Computational Materials Science, 151 (2018) 117-123.

[72] L. Pan, H. Guo, L. Zhong, M. Wang, P. Xue, X. Yuan, Influence of surface-modified glass fibers on interfacial properties of GF/PEEK composites using molecular dynamics, Computational Materials Science, 188 (2021) 110216.

[73] J. Liu, Y. Zhang, H. Zhang, J. Yang, Mechanical properties of graphene-reinforced aluminium composite with modified substrate surface: a molecular dynamics study, Nanotechnology, 32 (2020) 085712.

[74] H. Wang, K. Jin, C. Wang, X. Guo, Z. Chen, J. Tao, Effect of fiber surface functionalization on shear behavior at carbon fiber/epoxy interface through molecular dynamics analysis, Composites Part A: Applied Science and Manufacturing, 126 (2019) 105611.

[75] L.-h. Tam, J. Jiang, Z. Yu, J. Orr, C. Wu, Molecular dynamics investigation on the interfacial shear creep between carbon fiber and epoxy matrix, Applied Surface Science, 537 (2021) 148013.

[76] A. Rahman, P. Deshpande, M.S. Radue, G.M. Odegard, S. Gowtham, S. Ghosh, A.D. Spear, A machine learning framework for predicting the shear strength of carbon nanotube-polymer interfaces based on molecular dynamics simulation data, Composites Science and Technology, 207 (2021) 108627.

[77] O. Büyüköztürk, M.J. Buehler, D. Lau, C. Tuakta, Structural solution using molecular dynamics: Fundamentals and a case study of epoxy-silica interface, International Journal of Solids and Structures, 48 (2011) 2131-2140.

[78] W. Jian, L.-h. Tam, D. Lau, Atomistic study of interfacial creep behavior in epoxy-silica bilayer system, Composites Part B: Engineering, 132 (2018) 229-236.

[79] D. Hou, Q. Yang, P. Wang, Z. Jin, M. Wang, Y. Zhang, X. Wang, Unraveling disadhesion mechanism of epoxy/CSH interface under aggressive conditions, Cement and Concrete Research, 146 (2021).

[80] J. Fan, A. Anastassiou, C.W. Macosko, E.B. Tadmor, Molecular dynamics-based cohesive law for epoxy–graphene interfaces, Tribology Letters, 69 (2021) 1-17.

[81] D.-H. Kim, H.-S. Kim, Investigation of hygroscopic and mechanical properties of nanoclay/epoxy system: Molecular dynamics simulations and experiments, Composites Science and Technology, 101 (2014) 110-120.

[82] V.S. Vo, V.-H. Nguyen, S. Mahouche-Chergui, B. Carbonnier, D. Di Tommaso, S. Naili, From atomistic structure to thermodynamics and mechanical properties of epoxy/clay nanocomposites: Investigation by molecular dynamics simulations, Computational Materials Science, 139 (2017) 191-201.

[83] Y. Chen, J.Y.H. Chia, Z.C. Su, T.E. Tay, V.B.C. Tan, Mechanical characterization of interfaces in epoxy-clay nanocomposites by molecular simulations, Polymer, 54 (2013) 766-773.

[84] Z. Rahman, W. Yaacob, S. Rahim, T. Lihan, W. Idris, W. Sani, Geotechnical characterisation of marine clay as potential liner material, Sains Malaysiana, 42 (2013) 1081-1089.

[85] M. Thiry, Palaeoclimatic interpretation of clay minerals in marine deposits: an outlook from the continental origin, Earth-Science Reviews, 49 (2000) 201-221.

[86] Z. Liu, C. Colin, W. Huang, Z. Chen, A. Trentesaux, J. Chen, Clay minerals in surface sediments of the Pearl River drainage basin and their contribution to the South China Sea, Chinese Science Bulletin, 52 (2007) 1101-1111.

[87] S. Plimpton, Fast parallel algorithms for short-range molecular dynamics, Journal of computational physics, 117 (1995) 1-19.

[88] B. Yin, X. Hua, D. Qi, P. Wang, G. Qiao, F. Fan, X. Hua, X. Wang, D. Hou, Performance cement-based composite obtained by in-situ growth of organic–inorganic frameworks during the cement hydration, Construction and Building Materials, 336 (2022) 127533.

[89] P. Wang, G. Qiao, Y. Zhang, D. Hou, J. Zhang, M. Wang, X. Wang, X. Hu, Molecular dynamics simulation study on interfacial shear strength between calcium-silicate-hydrate and polymer fibers, Construction and Building Materials, 257 (2020) 119557.

[90] Z. Lu, J. Yu, J. Yao, D. Hou, Experimental and molecular modeling of polyethylene fiber/cement interface strengthened by graphene oxide, Cement and Concrete Composites, 112 (2020) 103676.

[91] R.W. Hockney, J.W. Eastwood, Particle-particle-particle-mesh (P3M) algorithms, Computer simulation using particles, (1988) 267-304.

[92] S. Nosé, A molecular dynamics method for simulations in the canonical ensemble, Molecular Physics, 52 (1984) 255-268.

[93] D. Bish, R. Von Dreele, Rietveld refinement of non-hydrogen atomic positions in kaolinite, Clays and Clay Minerals, 37 (1989) 289-296.

[94] X.L. Hu, A. Michaelides, The kaolinite (0 0 1) polar basal plane, Surface science, 604 (2010) 111-117.

[95] V.V. Murashov, E. Demchuk, A comparative study of unrelaxed surfaces on quartz and kaolinite, using the periodic density functional theory, The Journal of Physical Chemistry B, 109 (2005) 10835-10841.

[96] J.R.M. d'Almeida, G.W.d. Menezes, S.N. Monteiro, Ageing of the DGEBA/TETA epoxy system with off-stoichiometric compositions, Materials Research, 6 (2003) 415-420.

[97] F. Benard, J.-Y. Buzaré, I. Campistron, A. Laguerre, F. Laval, Influence of silica fillers during the electron irradiation of DGEBA/TETA epoxy resins, part III: Solid-state NMR investigations, Polymer degradation and stability, 92 (2007) 785-794.

[98] S. Meure, D.-Y. Wu, S.A. Furman, FTIR study of bonding between a thermoplastic healing agent and a mendable epoxy resin, Vibrational Spectroscopy, 52 (2010) 10-15.

[99] S. Yousefi-Nasab, J. Safdari, J. Karimi-Sabet, M. hasan Mallah, Molecular dynamics simulations on the scattering of heavy gases on the composite surfaces, Vacuum, 183 (2021) 109864.

[100] S. Yousefi-Nasab, J. Safdari, J. Karimi-Sabet, M.h. Mallah, Molecular dynamics simulations on the scattering of heavy gases on the composite surfaces, Vacuum, 183 (2021).

[101] C. Wu, W. Xu, Atomistic molecular modelling of crosslinked epoxy resin, Polymer, 47 (2006) 6004-6009.

[102] X.Q. Wang, W. Jian, O. Buyukozturk, C.K.Y. Leung, D. Lau, Degradation of epoxy/glass interface in hygrothermal environment: An atomistic investigation, Composites Part B: Engineering, 206 (2021).

[103] V. Varshney, S.S. Patnaik, A.K. Roy, B.L. Farmer, A molecular dynamics study of epoxy-based networks: cross-linking procedure and prediction of molecular and material properties, Macromolecules, 41 (2008) 6837-6842.

[104] D. Xin, Q. Han, Investigation of moisture diffusion in cross-linked epoxy moulding compound by molecular dynamics simulation, Molecular Simulation, 39 (2013) 322-329.

[105] F. Jeyranpour, G. Alahyarizadeh, B. Arab, Comparative investigation of thermal and mechanical properties of cross-linked epoxy polymers with different curing agents by molecular dynamics simulation, J Mol Graph Model, 62 (2015) 157-164.

[106] B. Kim, J. Choi, S. Yang, S. Yu, M. Cho, Influence of crosslink density on the interfacial characteristics of epoxy nanocomposites, Polymer, 60 (2015) 186-197.

[107] S. Yang, S. Yu, M. Cho, Sequential thermoelastic multiscale analysis of nanoparticulate composites, Journal of Applied Physics, 108 (2010).

[108] H.B. Fan, M.M.F. Yuen, Material properties of the cross-linked epoxy resin compound predicted by molecular dynamics simulation, Polymer, 48 (2007) 2174-2178.

[109] O. Sindt, J. Perez, J.F. Gerard, Molecular architecture-mechanical behaviour relationships in epoxy networks, Polymer, 37 (1996) 2989-2997.

[110] L.-L. Zhang, Y.-Y. Zheng, P.-C. Wei, Q.-F. Diao, Z.-Y. Yin, Nanoscale mechanical behavior of kaolinite under uniaxial strain conditions, Applied Clay Science, 201 (2021).

[111] C. Hu, C. Yi, M. Bai, J. Lv, D. Tang, Molecular dynamics study of the frictional properties of multilayer MoS 2, RSC advances, 10 (2020) 17418-17426.

[112] C. Hu, M. Bai, J. Lv, Z. Kou, X. Li, Molecular dynamics simulation on the tribology properties of two hard nanoparticles (diamond and silicon dioxide) confined by two iron blocks, Tribology International, 90 (2015) 297-305.

[113] S. Gao, L.H. Yang, Y. Gan, Q. Chen, The Influence of Sliding Speed on the Friction Behavior of Silica Surface, ACS Omega, 6 (2021) 3384-3389.

[114] B. Persson, Theory of friction: Stress domains, relaxation, and creep, Physical Review B, 51 (1995) 13568.

[115] P.-C. Wei, L.-L. Zhang, Y.-Y. Zheng, Q.-F. Diao, D.-Y. Zhuang, Z.-Y. Yin, Nanoscale friction characteristics of hydrated montmorillonites using molecular dynamics, Applied Clay Science, 210 (2021).

[116] A. Zaoui, Energetic stabilities and the bonding mechanism of ZnO {0001}/Pd (111) interfaces, Physical Review B, 69 (2004) 115403.

[117] P. Liu, X. Han, D. Sun, Z. Chen, Q. Wang, Adhesion, stability and electronic properties of Ti 2 AlN(0001)/TiAl(111) coherent interface from first-principles calculation, Intermetallics, 96 (2018) 49-57.

[118] N. Murali, P. Gujar, P. Ghosh, Performance of clay–epoxy interface at different points on proctor curve, Applied Clay Science, 226 (2022) 106553.

[119] A. Kinloch, Interfacial fracture mechanical aspects of adhesive bonded joints—a review, The Journal of Adhesion, 10 (1979) 193-219.

[120] K. Zukiene, G. Monastyreckis, S. Kilikevicius, M. Procházka, M. Micusik, M. Omastová, A. Aniskevich, D. Zeleniakiene, Wettability of MXene and its interfacial adhesion with epoxy resin, Materials Chemistry and Physics, 257 (2021).

[121] M. Sakr, M.H. El Naggar, M. Nehdi, Lateral behaviour of composite tapered piles in dense sand, Proceedings of the Institution of Civil Engineers-Geotechnical Engineering, 158 (2005) 145-157.

[122] Z. Wang, S. Wu, K. Weng, W. Yao, S. Xu, Z. Ding, Vertical and Lateral Bearing Capacity of FRP Composite Sheet Piles in Soft Soil, Advances in Civil Engineering, 2020 (2020).

[123] H. Chen, G. Zhang, Z. Lu, L. Bai, Frictional behaviors of diamond-like carbon films under water lubrication: A molecular dynamics study, Tribology International, 153 (2021).

[124] J.G. Vilhena, C. Pimentel, P. Pedraz, F. Luo, P.A. Serena, C.M. Pina, E. Gnecco, R. Perez, Atomic-Scale Sliding Friction on Graphene in Water, ACS Nano, 10 (2016) 4288-4293.

[125] R. Sinko, S. Keten, Traction–separation laws and stick–slip shear phenomenon of interfaces between cellulose nanocrystals, Journal of the Mechanics and Physics of Solids, 78 (2015) 526-539.

[126] L. Xu, T.-B. Ma, Y.-Z. Hu, H. Wang, Vanishing stick–slip friction in few-layer graphenes: the thickness effect, Nanotechnology, 22 (2011) 285708.

[127] W.G. Conley, C.M. Krousgrill, A. Raman, Stick-slip motions in the friction force microscope: Effects of tip compliance, Tribology Letters, 29 (2008) 23-32.

[128] A. Chatterjee, D.K. Dubey, S.K. Sinha, Effect of Loading on the Adhesion and Frictional Characteristics of Top Layer Articular Cartilage Nanoscale Contact: A Molecular Dynamics Study, Langmuir, 37 (2021) 46-62.

[129] H.M. Abuel-Naga, H.A. Shaia, Interface friction evolution of FRP tube confined concrete piles during the driving installation process, Géotechnique Letters, 4 (2014) 52-56.

[130] R. Pokhrel, N. Bhattarai, P. Baral, B.S. Gerstman, J.H. Park, M. Handfield, P.P. Chapagain, Molecular mechanisms of pore formation and membrane disruption by the antimicrobial lantibiotic peptide Mutacin 1140, Physical Chemistry Chemical Physics, 21 (2019) 12530-12539.

[131] H. Hölscher, D. Ebeling, U.D. Schwarz, Friction at atomic-scale surface steps: experiment and theory, Physical review letters, 101 (2008) 246105.

[132] T. Ackbarow, X. Chen, S. Keten, M.J. Buehler, Hierarchies, multiple energy barriers, and robustness govern the fracture mechanics of α-helical and β-sheet protein domains, Proceedings of the National Academy of Sciences, 104 (2007) 16410-16415.

[133] Y.L. Yaphary, Z. Yu, R.H.W. Lam, D. Hui, D. Lau, Molecular dynamics simulations on adhesion of epoxy-silica interface in salt environment, Composites Part B: Engineering, 131 (2017) 165-172.

[134] A.M. Page, G. Grimstad, G.R. Eiksund, H.P. Jostad, A macro-element pile foundation model for integrated analyses of monopile-based offshore wind turbines, Ocean Engineering, 167 (2018) 23-35.

[135] B. Xu, K. Wei, S. Qin, J. Hong, Experimental study of wave loads on elevated pile cap of pile group foundation for sea-crossing bridges, Ocean Engineering, 197 (2020) 106896.

[136] C.M. Su, Q. Sha, Y.C. Mou, Z.B. Jiao, Pre-Warning Pattern for Safety Monitoring of Artificial Islands in Coastal Areas during Operating Period, Applied Mechanics and Materials, 482 (2014) 419-422.

[137] M.A. Masuelli, Introduction of fibre-reinforced polymers− polymers and composites: concepts, properties and processes, in: Fiber reinforced polymers-the technology applied for concrete repair, IntechOpen, 2013.

[138] V. Farhangi, M. Karakouzian, Effect of fiber reinforced polymer tubes filled with recycled materials and concrete on structural capacity of pile foundations, Applied Sciences, 10 (2020) 1554.

[139] M.d.C. Gutiérrez-Castorena, W.R. Effland, 21 - Pedogenic and Biogenic Siliceous Features, in: G. Stoops, V. Marcelino, F. Mees (Eds.) Interpretation of Micromorphological Features of Soils and Regoliths, Elsevier, Amsterdam, 2010, pp. 471-496.

[140] P. Cosoli, M. Fermeglia, M. Ferrone, Molecular Simulation of Atrazine Adhesion and Diffusion in a Saturated Sand Model, Soil and Sediment Contamination: An International Journal, 19 (2010) 72-87.

[141] Q. Meng, D. Chen, G. Wu, Microscopic Mechanisms for the Dynamic Wetting of a Heavy Oil Mixture on a Rough Silica Surface, The Journal of Physical Chemistry C, 122 (2018) 24977-24986.

[142] S.C. Chowdhury, B.Z. Haque, J.W. Gillespie, Molecular dynamics simulations of the structure and mechanical properties of silica glass using ReaxFF, Journal of Materials Science, 51 (2016) 10139-10159.

[143] J. Luo, Y. Xu, Y. Zhong, J. Teng, W. Yao, L. Hao, C. Kang, Molecular dynamics analysis of wetting behavior of nano water drops on quartz sand surface, Comptes Rendus. Mécanique, 349 (2021) 485-499.

[144] D. Lau, K. Broderick, M.J. Buehler, O. Buyukozturk, A robust nanoscale experimental quantification of fracture energy in a bilayer material system, Proc Natl Acad Sci U S A, 111 (2014) 11990-11995.

[145] A. Stukowski, Visualization and analysis of atomistic simulation data with OVITO–the Open Visualization Tool, Modelling and simulation in materials science and engineering, 18 (2009) 015012.

[146] L.-h. Tam, D. Lau, A molecular dynamics investigation on the cross-linking and physical properties of epoxy-based materials, RSC Adv., 4 (2014) 33074-33081.

[147] S. Masoumi, B. Arab, H. Valipour, A study of thermo-mechanical properties of the cross-linked epoxy: An atomistic simulation, Polymer, 70 (2015) 351-360.

[148] A.L. Rosa, A.A. El-Barbary, M.I. Heggie, P.R. Briddon, Structural and thermodynamic properties of water related defects in α-quartz, Physics and Chemistry of Minerals, 32 (2005) 323-331.

[149] R. Hill, The Elastic Behaviour of a Crystalline Aggregate, Proceedings of the Physical Society. Section A, 65 (1952) 349-354.

[150] S. Yu, S. Yang, M. Cho, Multi-scale modeling of cross-linked epoxy nanocomposites, Polymer, 50 (2009) 945-952.

[151] F.G. Garcia, B.G. Soares, V.J.R.R. Pita, R. Sánchez, J. Rieumont, Mechanical properties of epoxy networks based on DGEBA and aliphatic amines, Journal of Applied Polymer Science, 106 (2007) 2047-2055.

[152] Z. Lai, X. Zhao, R. Tang, J. Yang, G. Zhou, Electrical Conductivity-Based Estimation of Unfrozen Water Content in Saturated Saline Frozen Sand, Advances in Civil Engineering, 2021 (2021) 1-13.

[153] V. Thurmond, R. Potter II, M. Clynne, The densities of saturated solutions of NaCl and KCL from 10 degrees to 105 degrees C, in, US Geological Survey, 1984.

[154] E.-Q. Lin, L.-S. Niu, H.-J. Shi, Z. Duan, Molecular dynamics simulation of nano-scale interfacial friction characteristic for different tribopair systems, Applied Surface Science, 258 (2012) 2022-2028.

[155] S. Yuan, X. Guo, Q. Mao, J. Guo, A.C.T. van Duin, Z. Jin, R. Kang, D. Guo, Effects of pressure and velocity on the interface friction behavior of diamond utilizing ReaxFF simulations, International Journal of Mechanical Sciences, 191 (2021).

[156] Z.-J. Wang, T.-B. Ma, Y.-Z. Hu, L. Xu, H. Wang, Energy dissipation of atomic-scale friction based on one-dimensional Prandtl-Tomlinson model, Friction, 3 (2015) 170-182.

[157] S. Cohen, D. Tabor, The friction and lubrication of polymers, Proceedings of the Royal Society of London. Series A. Mathematical and Physical Sciences, 291 (1966) 186-207.

[158] V. Nardelli, M.R. Coop, The experimental contact behaviour of natural sands: normal and tangential loading, Géotechnique, 69 (2019) 672-686.

[159] B. Zhao, F. Wu, K. Sun, X. Mu, Y. Zhang, Q. Sun, Study on tangential stiffness nonlinear softening of bolted joint in friction-sliding process, Tribology International, 156 (2021).

[160] A. Lashkari, Prediction of the shaft resistance of nondisplacement piles in sand, International Journal for numerical and analytical methods in geomechanics, 37 (2013) 904-931.

[161] J. Archard, Elastic deformation and the laws of friction, Proceedings of the royal society of London. Series A. Mathematical and physical sciences, 243 (1957) 190-205.

[162] S. Brunet, J.C. de la Llera, E. Kausel, Non-linear modeling of seismic isolation systems made of recycled tire-rubber, Soil Dynamics and Earthquake Engineering, 85 (2016) 134-145.

[163] S.M. Tafreshi, A. Norouzi, Application of waste rubber to reduce the settlement of road embankment, Geomechanics & Engineering, 9 (2015) 219-241.

[164] A. Mohajerani, L. Burnett, J.V. Smith, S. Markovski, G. Rodwell, M.T. Rahman, H. Kurmus, M. Mirzababaei, A. Arulrajah, S. Horpibulsuk, F. Maghool, Recycling waste rubber tyres in construction materials and associated environmental considerations: A review, Resources, Conservation and Recycling, 155 (2020).

[165] N. Ecemis, H. Valizadeh, M. Karaman, Sand-granulated rubber mixture to prevent liquefaction-induced uplift of buried pipes: a shaking table study, Bulletin of Earthquake Engineering, 19 (2021) 2817-2838.

[166] D. ASTM, Standard practice for use of scrap tires in civil engineering applications, in: American Society for Testing and Materials West Conshohocken, PA, 2008.

[167] T. Zhang, G. Cai, W. Duan, Strength and microstructure characteristics of the recycled rubber tire-sand mixtures as lightweight backfill, Environ Sci Pollut Res Int, 25 (2018) 3872-3883.

[168] E. Mahdavisefat, H. Salehzadeh, A.A. Heshmati, Full-scale experimental study on screening effectiveness of SRM-filled trench barriers, Géotechnique, 68 (2018) 869-882.

[169] W. Xiong, Y. Li, Seismic isolation using granulated tire–soil mixtures for less-developed regions: experimental validation, Earthquake Engineering & Structural Dynamics, 42 (2013) 2187-2193.

[170] K. Pitilakis, S. Karapetrou, K. Tsagdi, Numerical investigation of the seismic response of RC buildings on soil replaced with rubber–sand mixtures, Soil Dynamics and Earthquake Engineering, 79 (2015) 237-252.

[171] A.K. Panah, A. Khoshay, A new seismic isolation system: sleeved-pile with soil-rubber mixture, International journal of civil engineering, 13 (2015) 124-132.

[172] H.-H. Tsang, K. Pitilakis, Mechanism of geotechnical seismic isolation system: Analytical modeling, Soil Dynamics and Earthquake Engineering, 122 (2019) 171-184.

[173] S. Dutta, R.P. Nanda, Finite element analysis of rubber–soil mixture (RSM) for the pile response reduction under liquefaction, Arabian Journal of Geosciences, 14 (2021).

[174] B. Abbasi, B. Muhunthan, I. Salehinia, H.M. Zbib, Nanoscale Stick-Slip Behavior of Na-Montmorillonite Clay, Journal of Engineering Mechanics, 146 (2020).

[175] P.-C. Wei, Y.-Y. Zheng, A. Zaoui, Z.-Y. Yin, Atomistic study on thermo-mechanical behavior and structural anisotropy of montmorillonite under triaxial tension and compression, Applied Clay Science, 233 (2023) 106817.

[176] S. Tembe, D.A. Lockner, T.-F. Wong, Effect of clay content and mineralogy on frictional sliding behavior of simulated gouges: Binary and ternary mixtures of quartz, illite, and montmorillonite, Journal of Geophysical Research: Solid Earth, 115 (2010).

[177] G.A. Pistolas, K. Pitilakis, A. Anastasiadis, A numerical investigation on the seismic isolation potential of rubber/soil mixtures, Earthquake Engineering and Engineering Vibration, 19 (2020) 683-704.

[178] K.B. Thapa, K.S. Katti, D.R. Katti, Influence of the fluid polarity on shear strength of sodium montmorillonite clay: A steered molecular dynamics study, Computers and Geotechnics, 158 (2023).

[179] J. Xu, X. Chen, B. Yu, Experimental and simulation study of rubber/cement paste interface modified by waste paint and silica in two stages, Construction and Building Materials, 382 (2023).

[180] J. Kang, Y. Liu, J. Yuan, C. Chen, L. Wang, Z. Yu, Effectiveness of surface treatment on rubber particles towards compressive strength of rubber concrete: A numerical study on rubber-cement interface, Construction and Building Materials, 350 (2022).

[181] J. Yu, D. Hou, J. Zhang, Molecular dynamics study on ultra-confined NaCl solution in the silane coupling agent modified rubber calcium silicate hydrate nano-pore, Construction and Building Materials, 270 (2021).

[182] Q. Han, Y. Yang, J. Zhang, J. Yu, D. Hou, B. Dong, H. Ma, Insights into the interfacial strengthening mechanism of waste rubber/cement paste using polyvinyl alcohol: Experimental and molecular dynamics study, Cement and Concrete Composites, 114 (2020).

[183] L.L. Zhang, A. Zaoui, W. Sekkal, Y.Y. Zheng, Interlayer adsorption of cationic dye on cationic surfactant-modified and unmodified montmorillonite, J Hazard Mater, 442 (2023) 130107.

[184] H. Zhao, H. Cui, S. Jiang, W. Awadalseed, J. Guo, W. Yang, X. Kang, Tensile and compressive behavior of Na-, K-, Ca-Montmorillonite and temperature effects, Chemical Physics, 569 (2023) 111855.

[185] A. Viani, A.F. Gualtieri, G. Artioli, The nature of disorder in montmorillonite by simulation of X-ray powder patterns, American Mineralogist, 87 (2002) 966-975.

[186] Y. Zheng, A. Zaoui, I. Shahrour, A theoretical study of swelling and shrinking of hydrated Wyoming montmorillonite, Applied Clay Science, 51 (2011) 177-181.

[187] Y. Ichikawa, K. Kawamura, N. Fujii, T. Nattavut, Molecular dynamics and multiscale homogenization analysis of seepage/diffusion problem in bentonite clay, International journal for numerical methods in engineering, 54 (2002) 1717-1749.

[188] K. Tong, J. Guo, S. Chen, F. Yu, S. Li, Z. Dai, A simulation study on the swelling and shrinking behaviors of nanosized montmorillonite based on monte carlo and molecular dynamics, Geofluids, 2021 (2021) 1-13.

[189] P. Sharma, S. Roy, H.A. Karimi-Varzaneh, Validation of Force Fields of Rubber through Glass-Transition Temperature Calculation by Microsecond Atomic-Scale Molecular Dynamics Simulation, J Phys Chem B, 120 (2016) 1367-1379.

[190] L.J. Fetters, D.J. Lohse, W.W. Graessley, Chain dimensions and entanglement spacings in dense macromolecular systems, Journal of Polymer Science Part B: Polymer Physics, 37 (1999) 1023-1033.

[191] X. Lu, B. Jiang, Glass transition temperature and molecular parameters of polymer, Polymer, 32 (1991) 471-478.

[192] P. Handbook, J. Brandrup, E. Immergut, International Science, in, Wiley, New York, 1989.

[193] A.V. Tobolsky, H.F. Mark, Polymer science and materials, R. E. Krieger Pub. Co., 1980.

[194] J. Brandrup, E.H. Immergut, E.A. Grulke, A. Abe, D.R. Bloch, Polymer handbook, Wiley New York, 1999.

[195] W.-S. Kim, I.-H. Yun, J.-J. Lee, H.-T. Jung, Evaluation of mechanical interlock effect on adhesion strength of polymer–metal interfaces using micro-patterned surface topography, International Journal of Adhesion and Adhesives, 30 (2010) 408-417.

[196] M. Maiti, A.K. Bhowmick, Structure and properties of some novel fluoroelastomer/clay nanocomposites with special reference to their interaction, Journal of Polymer Science Part B: Polymer Physics, 44 (2006) 162-176.

[197] J.C. Dai, J.T. Huang, Surface modification of clays and clay–rubber composite, Applied clay science, 15 (1999) 51-65.

[198] M. Bhattacharya, M. Maiti, A.K. Bhowmick, Tailoring properties of styrene butadiene rubber nanocomposite by various nanofillers and their dispersion, Polymer Engineering & Science, 49 (2009) 81-98.

[199] M.R. Kamal, J.U. Calderon, B.R. Lennox, Surface energy of modified nanoclays and its effect on polymer/clay nanocomposites, Journal of adhesion science and technology, 23 (2009) 663-688.

[200] L. Zhu, W. Shen, J. Shao, M. He, Insight of molecular simulation to better assess deformation and failure of clay-rich rocks in compression and extension, International Journal of Rock Mechanics and Mining Sciences, 138 (2021).

[201] K. Liu, H. Liu, Simulation of the earthquake-induced soil-rock mixed accumulation body sliding movement using discrete–continuous coupled approach, Natural Hazards, 114 (2022) 2087-2108.

[202] S. Yuan, X. Guo, J. Huang, Y. Gou, Z. Jin, R. Kang, D. Guo, Insight into the mechanism of low friction and wear during the chemical mechanical polishing process of diamond: A reactive molecular dynamics simulation, Tribology International, 148 (2020).

[203] Y. Dong, Q. Li, A. Martini, Molecular dynamics simulation of atomic friction: A review and guide, Journal of Vacuum Science & Technology A: Vacuum, Surfaces, and Films, 31 (2013) 030801.

[204] M.Y. Chen, Z.H. Hong, T.H. Fang, S.H. Kang, L.M. Kuo, Effect of Textured Surface on Sliding Friction Investigated Using Molecular Dynamic Simulation, Applied Mechanics and Materials, 284-287 (2013) 296-299.

[205] P. Stoyanov, P.A. Romero, R. Merz, M. Kopnarski, M. Stricker, P. Stemmer, M. Dienwiebel, M. Moseler, Nanoscale sliding friction phenomena at the interface of diamond-like carbon and tungsten, Acta Materialia, 67 (2014) 395-408.

[206] L. Dai, V. Sorkin, Z.D. Sha, Q.X. Pei, P.S. Branicio, Y.W. Zhang, Molecular dynamics simulations on the frictional behavior of a perfluoropolyether film sandwiched between diamond-like-carbon coatings, Langmuir, 30 (2014) 1573-1579.

[207] R.M. Varghese, G. Madhavi Latha, Shaking table tests to investigate the influence of various factors on the liquefaction resistance of sands, Natural hazards, 73 (2014) 1337-1351.

[208] H. Suprijanto, A.P. Hendrawan, A.W.B. Nugraha, Potential study of the liquefaction hazard at the reclamation development site of I Gusti Ngurah Rai airport, Nusa Dua region, province of Bali, in: IOP Conference Series: Earth and Environmental Science, IOP Publishing, 2020, pp. 012058.

[209] P. Mora, D. Place, Simulation of the frictional stick-slip instability, pure and applied geophysics, 143 (1994) 61-87.

[210] N.J. Finnegan, E.E. Brodsky, H.M. Savage, A.L. Nereson, C.R. Murphy, Seasonal Slow Landslide Displacement Is Accommodated by mm-Scale Stick-Slip Events, Geophysical Research Letters, 49 (2022) e2022GL099548.

[211] X.C. Wang, J.L. Mo, H. Ouyang, X.D. Lu, B. Huang, Z. Zhou, The effects of grooved rubber blocks on stick–slip and wear behaviours, Proceedings of the Institution of Mechanical Engineers, Part D: Journal of Automobile Engineering, 233 (2019) 2939-2954.

[212] H.-H. Tsang, S.H. Lo, X. Xu, M. Neaz Sheikh, Seismic isolation for low-to-medium-rise buildings using granulated rubber-soil mixtures: numerical study, Earthquake Engineering & Structural Dynamics, 41 (2012) 2009-2024.

[213] A.M. Homola, J.N. Israelachvili, P.M. McGuiggan, M.L. Gee, Fundamental experimental studies in tribology: The transition from “interfacial” friction of undamaged molecularly smooth surfaces to “normal” friction with wear, Wear, 136 (1990) 65-83.

[214] W. Dang, H. Konietzky, T. Frühwirt, M. Herbst, Cyclic frictional responses of planar joints under cyclic normal load conditions: laboratory tests and numerical simulations, Rock Mechanics and Rock Engineering, 53 (2020) 337-364.
[215] K. Tao, W. Dang, Y. Li, Frictional sliding of infilled planar granite fracture under oscillating normal stress, International Journal of Mining Science and Technology, 33 (2023) 687-701.
[216] K.G. Gatos, K. Kameo, J. Karger-Kocsis, On the friction and sliding wear of rubber/layered silicate nanocomposites, Express Polymer Letters, 1 (2007) 27-31.
[217] S. Manuwa, Evaluation of soil/material interface friction and adhesion of Akure sandy clay loam soils in southwestern Nigeria, Advances in Natural Science, 5 (2012) 41-46.
[218] K.D. Kumar, A.H. Tsou, A.K. Bhowmick, Unique Tackification Behavior of Needle-like Sepiolite Nanoclay in Brominated Isobutylene-co-p-methylstyrene (BIMS) Rubber, Macromolecules, 43 (2010) 4184-4193.
[219] H. Tetsuka, I. Katayama, H. Sakuma, K. Tamura, Effects of humidity and interlayer cations on the frictional strength of montmorillonite, Earth, Planets and Space, 70 (2018).
[220] L. Sakellariadis, A. Marin, I. Anastasopoulos, Widening of Existing Motorway Bridges: Pile Group Retrofit versus Nonlinear Pile–Soil Response, J Geotech Geoenviron, 145 (2019).
[221] M.H. El Naggar, Geo-structural nonlinear analysis of piles for infrastructure design, Innov Infrastruct So, 3 (2018).
[222] S.W. Liu, J.H. Wan, C.Y. Zhou, Z. Liu, X. Yang, Efficient beam–column finite-element method for stability design of slender single pile in soft ground mediums, Int J Geomech, 20 (2020) 04019148.
[223] R. Jardine, D. Potts, A. Fourie, J. Burland, Studies of the influence of non-linear stress–strain characteristics in soil–structure interaction, Geotechnique, 36 (1986) 377-396.
[224] F. Basile, Non-linear analysis of pile groups, Proceedings of the Institution of Civil Engineers-Geotechnical Engineering, 137 (1999) 105-115.
[225] F. Basile, Non-linear analysis of vertically loaded piled rafts, Comput Geotech, 63 (2015) 73-82.
[226] H.H. Bui, K. Sako, R. Fukagawa, J. Wells, SPH-based numerical simulations for large deformation of geomaterial considering soil-structure interaction, in: The 12th international conference of international association for computer methods and advances in geomechanics (IACMAG), Citeseer, 2008, pp. 570-578.
[227] J. Liu, C. Shi, C. Cao, M. Lei, Z. Wang, Improved analytical method for pile response due to foundation pit excavation, Comput Geotech, 123 (2020) 103609.
[228] P.A. Arvan, M. Arockiasamy, Energy-based approach: analysis of a laterally loaded pile in multi-layered non-Linear elastic soil strata, Geotechnics, 2 (2022) 570-598.
[229] X.Y. Li, J.H. Wan, S.W. Liu, L.M. Zhang, Numerical formulation and implementation of Euler‐Bernoulli pile elements considering soil‐structure‐interaction responses, Int J Numer Anal Met, 44 (2020) 1903-1925.
[230] J. Yang, P. Li, Z. Lu, Large‐scale shaking table test on pile‐soil‐structure interaction on soft soils, The Structural Design of Tall and Special Buildings, 28 (2019) e1679.
[231] A.E. Kampitsis, S. Giannakos, N. Gerolymos, E.J. Sapountzakis, Soil–pile interaction considering structural yielding: Numerical modeling and experimental validation, Eng Struct, 99 (2015) 319-333.
[232] R.K. Goel, Evaluation of in-ground plastic-hinge length and depth for piles in marine oil terminals, Earthq Spectra, 31 (2015) 2397-2417.
[233] M. Heidari, M. Hesham El Naggar, Analytical Approach for Seismic Performance of Extended Pile-Shafts, J Bridge Eng, 23 (2018).

[234] B.A. IZZUDDIN, A.S. ELNASHAI, Adaptive space frame analysis. part I: a plastic hinge approach, Proceedings of the Institution of Civil Engineers - Structures and Buildings, 99 (1993) 303-316.
[235] J.R. Liew, H. Chen, N. Shanmugam, W. Chen, Improved nonlinear plastic hinge analysis of space frame structures, Eng Struct, 22 (2000) 1324-1338.
[236] Y.H. Chai, Flexural Strength and Ductility of Extended Pile-Shafts. I: Analytical Model, J Struct Eng, 128 (2002) 586-594.
[237] A.Y. Abdelaziz, M.H. El Naggar, M. Ouda, Determination of depth-of-fixity point for laterally loaded vertical offshore piles: A new approach, Ocean Eng, 232 (2021).
[238] A.M. Budek, M.J.N. Priestley, G. Benzoni, Inelastic Seismic Response of Bridge Drilled-Shaft RC Pile/Columns, J Struct Eng, 126 (2000) 510-517.
[239] S. Song, Y. Chai, T. Hale, Analytical model for ductility assessment of fixed-head concrete piles, J Struct Eng, 131 (2005) 1051-1059.
[240] J.S. Chiou, C.L. Lin, C.H. Chen, Exploring influence of sectional flexural yielding on experimental pile response analysis and applicability of distributed plastic hinge model in inelastic numerical simulation for laterally loaded piles, Comput Geotech, 56 (2014) 40-49.
[241] J.S. Chiou, H.H. Yang, C.H. Chen, Use of Plastic Hinge Model in Nonlinear Pushover Analysis of a Pile, J Geotech Geoenviron, 135 (2009) 1341-1346.
[242] Y. Zhang, X. Chen, X. Zhang, M. Ding, Y. Wang, Z. Liu, Nonlinear response of the pile group foundation for lateral loads using pushover analysis, Earthq Struct, 19 (2020) 273-286.
[243] G. Pacheco, L.E. Suárez, M. Pando, Dynamic lateral response of single piles considering soil inertia contributions, in: World Conference on Earthquake Engineering. Beijing, China2008, 2008.
[244] V. Tandjiria, C.I. Teh, B.K. Low, Reliability analysis of laterally loaded piles using response surface methods, Struct Saf, 22 (2000) 335-355.
[245] S. Joshi, A. Prashant, A. Deb, S.K. Jain, Analysis of buried pipelines subjected to reverse fault motion, Soil Dyn Earthq Eng, 31 (2011) 930-940.
[246] G. Wu, W.L. Finn, Dynamic nonlinear analysis of pile foundations using finite element method in the time domain, Can Geotech J, 34 (1997) 44-52.
[247] L.J. Prendergast, K. Gavin, A comparison of initial stiffness formulations for small-strain soil–pile dynamic Winkler modelling, Soil Dyn Earthq Eng, 81 (2016) 27-41.
[248] S. Wang, B.L. Kutter, M.J. Chacko, D.W. Wilson, R.W. Boulanger, A. Abghari, Nonlinear seismic soil-pile structure interaction, Earthq Spectra, 14 (1998) 377-396.
[249] S. Adhikary, V.R. Deoda, Seismic response of a tall tower on deep soil–A case study, in: Structures, Elsevier, 2022, pp. 1183-1199.
[250] X.Y. Li, J.H. Wan, H.P. Zhao, S.W. Liu, Three-Dimensional Analysis of Nonlinear Pile-Soil Interaction Responses Using 3D Pile Element Model, Int J Geomech, 21 (2021) 04021129.
[251] K.M. Hsiao, R.T. Yang, A co-rotational formulation for nonlinear dynamic analysis of curved euler beam, Comput Struct, 54 (1995) 1091-1097.
[252] S. Chhang, C. Sansour, M. Hjiaj, J.-M. Battini, An energy-momentum co-rotational formulation for nonlinear dynamics of planar beams, Comput Struct, 187 (2017) 50-63.
[253] C.Y. Yau, S.L. Chan, Inelastic and Stability Analysis of Flexibly Connected Steel Frames by Springs-Series-Model, J Struct Eng, 120 (1994) 2803-2819.
[254] S.L. Chan, Z.H. Zhou, Elastoplastic and large deflection analysis of steel frames by one element per member. II: Three hinges along member, J Struct Eng, 130 (2004) 545-553.
[255] S.W. Liu, Y.P. Liu, S.L. Chan, Direct analysis by an arbitrarily-located-plastic-hinge element—Part 2: Spatial analysis, J Constr Steel Res, 103 (2014) 316-326.
[256] S.W. Liu, Y.P. Liu, S.L. Chan, Direct analysis by an arbitrarily-located-plastic-hinge element—Part 1: Planar analysis, J Constr Steel Res, 103 (2014) 303-315.

[257] R. Bai, S.W. Liu, Y.P. Liu, S.L. Chan, Direct analysis of tapered-I-section columns by one-element-per-member models with the appropriate geometric-imperfections, Eng Struct, 183 (2019) 907-921.
[258] S.L. Chan, P.T. Chui, Non-linear static and cyclic analysis of steel frames with semi-rigid connections, Elsevier, 2000.
[259] K.J. Bathe, Finite element procedures, Prentice-Hall, Boston, 2006.
[260] J.L. Batoz, G. Dhatt, Incremental displacement algorithms for nonlinear problems, International Journal for Numerical Methods in Engineering, 14 (1979) 1262-1267.
[261] M. Nadeem, T. Chakraborty, V. Matsagar, Nonlinear Buckling Analysis of Slender Piles with Geometric Imperfections, J Geotech Geoenviron, 141 (2015).
[262] M.A. Pando, A laboratory and field study of composite piles for bridge substructures, (2003).
[263] L.C. Reese, W.R. Cox, F.D. Koop, Analysis of Laterally Loaded Piles in Sand, in: Offshore Technology Conference, OnePetro, Houston, Texas, USA, 1974, pp. 95-105.
[264] J.L. Snyder, Full-Scale Lateral-Load Tests of a 3x5 Pile Group in Soft Clays and Silts, in, 2004.
[265] L.C. Reese, W.R. Cox, F.D. Koop, Field Testing and Analysis of Laterally Loaded Piles om Stiff Clay, in: Offshore Technology Conference, Onepetro, Houston, Texas, USA, 1975, pp. 671-690.
[266] Q.Q. Zhang, Z.M. Zhang, J.Y. He, A simplified approach for settlement analysis of single pile and pile groups considering interaction between identical piles in multilayered soils, Comput Geotech, 37 (2010) 969-976.
[267] S.Y. Joshi, S.A. Deshmukh, A review of advancements in coarse-grained molecular dynamics simulations, Molecular Simulation, 47 (2020) 786-803.